The infrared spectrum of massive protostars: circumstellar disks and high mass star formation

Barr, A.G.

4 | H_2O Absorption in Circumstellar Disks of Massive Protostars at High Spectral Resolution: Full spectral survey results of AFGL 2591 and AFGL 2136

Abstract

We have performed a high-resolution 4-13 μm spectral survey of the hot molecular gas associated with the massive protostars AFGL 2591 and AFGL 2136. Here we present the results of the analysis of the ν_2 band of H_2O, detected with the Echelon Cross Echelle Spectrograph (EXES) on board the Stratospheric Observatory for Infrared Astronomy (SOFIA) between wavelengths of 5-8 μm. All lines are seen in absorption. Rotation diagrams indicate that the gas is optically thick and lines are observed to saturate at 40% and 15% relative to the continuum for AFGL 2136 and AFGL 2591, respectively. We applied two curve of growth analyses to derive the physical conditions, one assuming a foreground origin and one a circumstellar disk origin. We find temperatures of 400-600 K. A foreground origin would require the presence of externally heated clumps that are smaller than the continuum source. The disk analysis is based on stellar atmosphere theory which takes into consideration the temperature gradient in the disk. We discuss the challenges with each model and conclude that the disk origin for the absorption lines best explains the data, where a direct prediction of the stellar atmosphere model is that absorption lines should saturate at non-zero flux. Furthermore, abundance ratios are consistent with a disk chemistry. This implies the presence of a viscously heated disk that has a temperature gradient which decreases with scale height, in order to explain the presence of absorption lines.

A. G. Barr, J. Li, A. Boogert, C. N. DeWitt, E. Montiel, M. J. Richter, N. Indriolo, Y. Pendleton, J. Chiar, A. G. G. M. Tielens

The Astrophysical Journal, In review

4.1 Introduction

Water is observed throughout the universe; from diffuse and translucent clouds to dense star forming regions, shocks, protoplanetary disks and comets, evolved stars and external galaxies (van Dishoeck et al. 2013). Its importance in the environment of star forming regions is exhibited by it being one of the most abundant molecules in both the ice and gas-phases. In warm regions, due to ice sublimation (T>100 K) and gas phase chemistry (T>250 K), all of the available oxygen that is not locked up in CO or dust grains is driven into H_2O resulting in a jump in abundance from as low as 10^{-9} with respect to H in the cold envelope, to up to 10^{-4} in the hot gas close to the protostar (Boonman et al. 2003a; Boonman & van Dishoeck 2003). It is one of the main carriers of oxygen and readily detected towards low to high mass protostars, therefore it is of fundamental importance to studies of star formation.

A massive protostar forms out of a gravitationally unstable core in a dark molecular cloud (Egan et al. 1998; Zinnecker & Yorke 2007). During this process, an accretion disk develops around the protostar through which material from the envelope can be channeled onto the forming star. Due to the high accretion rates, the disk is heated from the mid-plane by viscous processes (Dullemond et al. 2007; D'Alessio et al. 1998). The disk and protostar at this stage will still be deeply embedded in the parent molecular cloud, and will remain so until after the star reaches the main sequence (Beuther et al. 2007).

Water is very difficult to observe from the ground due to the large quantity of H_2O in the Earth's atmosphere. Ideally observations would be carried out with space based facilities, to study H_2O in depth. This is reflected in the particular success of the Infrared Space Observatory (ISO) (Cernicharo & Crovisier 2005) and the Herschel Space Observatory in observing H_2O in all of the astronomical objects previously mentioned (Melnick et al. 2010; Neufeld et al. 2011; Moreno et al. 2012; van der Tak et al. 2013; van Dishoeck et al. 2021). The Stratospheric Observatory for Infrared Astronomy (SOFIA) offers an alternative opportunity for studying H_2O, as it flies above most of the water in the Earth's atmosphere, vastly reducing interference, and allowing the opportunity to observe hundreds of ro-vibrational H_2O lines, including low energy lines, and even lines tracing the ground level (Indriolo et al. 2015a).

Gas-phase H_2O absorption towards massive protostars has been studied extensively with ISO's short wavelength spectrometer (SWS) (van Dishoeck & Helmich 1996; Cernicharo et al. 1997; van Dishoeck 1998; González-Alfonso et al. 1998; Wright et al. 2000; Boonman & van Dishoeck 2003; Boonman et al. 2003a). The cold envelope and warm protostellar environment were distinguished by a "jump" in the H_2O abundance as the temperature transitioned from low to high (Boonman & van Dishoeck 2003; Boonman et al. 2003a). The low resolution ($R \sim 1400$) of ISO/SWS, however, meant that the individual ro-vibrational H_2O transitions blended into each other, creating a single broad absorption feature. The result of this was that physical conditions had to be derived assuming a single absorbing slab model in local thermodynamic equilibrium (LTE) and adopting a simple line profile. Moreover, because of the low spectral resolution, no kinematic information could be obtained.

We have conducted the first full spectral survey of the mid-infrared (mid-IR) wavelength region at high spectral resolution of two massive protostars. Previous

papers have focused on the simple organics detected, including HCN, C_2H_2, NH_3, CS and ^{13}CO (chapters 2 and 3). All species are seen in absorption and are optically thin. Abundance/column density variations are observed in HCN and C_2H_2 with absorption bands tracing the same lower level exhibiting differences up to a factor of 10. The bands at 13 μm have a lower abundance compared to bands at 7 μm, for both AFGL 2136 and AFGL 2591. If this absorption was due to foreground gas, this would imply a smaller covering factor of the continuum source at 13 μm compared to 7 μm. Knez et al. (2009) find that absorbing gas is optically thick and lines are saturated towards NGC 7538 IRS1, however lines do not go to zero flux. They suggest that this could be due to partial covering of the continuum source, however this is highly uncertain with covering factors ranging from of a few % to 100% across two absorbing components. Barentine & Lacy (2012) found that toward NGC 7538 IRS1, the column of C_2H_2 is higher at 7 μm compared to 13 μm. They attributed this to varying opacity in the stellar photosphere with wavelength, locating the absorption lines to probe this region, however this could only account for a factor of 2 difference in the column density.

Here we discuss H_2O in the context of this spectral survey, where the fully resolved H_2O lines allow temperatures and abundances to be derived as well as the study of kinematics in these environments. The details of the survey and analysis techniques are outlined in sections 4.2 and 4.3, respectively. In section 4.4 we present the results for the H_2O lines in the contexts of both a foreground absorbing slab and a stellar atmosphere model assuming a disk origin, and in section 4.5 we discuss these results elaborating on, and comparing, the two approaches.

4.2 Observations and Data Reduction

AFGL 2591 and AFGL 2136 were observed with the Echelon Cross Echelle Spectrograph (EXES) spectrometer (Richter et al. 2018) onboard SOFIA flying observatory (Young et al. 2012) as part of SOFIA programs 05_0041 and 06_0117. In this full spectral survey of AFGL 2591 and AFGL 2136, EXES covered the range 5.3-8 μm and required 16 wavelength settings in its HIGH-LOW mode, where the high-resolution echelon grating is cross-dispersed at the lowest practical order/angle so that the instantaneous wavelength coverage was maximised. AFGL 2591 was observed to completion in March 2017, but AFGL 2136 was observed over three flight series which spanned March 2017-April 2019. The slit width was 3.2″ for all settings, providing R=55,000 resolution. The fixed slit lengths used were either 3.1″ or 2.2″, depending on the wavelength setting. In order to remove background night sky emission and telescope thermal emission, the telescope was nodded to an off-source position 15″ away from the target coordinates every 1-2 minutes. During the flight series, the precipitable water vapour (pwv) meter on SOFIA was not working, therefore the quantity of water in the atmosphere could not be measured.

Table 4.1: Summary of Observations. V_{dop} is the Earth's velocity relative to local standard rest (LSR) at the time of the observations in the direction of the YSOs. Integration time is the time spent on source.

Source	Date (UT)	Time (UT)	Wavelength Range (μm)	V_{dop} (km s^{-1})	Integration Time (s)	Longitude (deg)	Latitude (deg)	Altitude (feet)	Zenith Angle (deg)
AFGL 2591	2017-03-23	10:06:16	7.83 - 8.01	25.8	120	-101.7	44.7	42086	53.2
	2017-03-23	09:51:47	7.67 - 7.85	25.8	240	-102.6	45.8	42066	55.0
	2017-03-17	10:34:18	7.51 - 7.69	24.4	420	-104.3	44.0	44006	51.9
	2017-03-17	10:15:14	7.34 - 7.52	24.4	300	-106.5	46.9	43043	57.1
	2017-03-22	11:47:14	7.19 - 7.37	25.6	390	-124.1	34.1	43056	54.1
	2017-03-23	09:32:32	7.02 - 7.20	25.8	330	-104.2	47.6	42069	56.9
	2017-03-21	10:14:38	6.87 - 7.05	25.3	270	-100.8	43.0	43006	51.2
	2017-03-21	09:55:52	6.69 - 6.88	25.3	300	-102.5	45.3	41998	54.4
	2017-03-23	10:14:17	6.53 - 6.71	25.8	300	-100.2	42.8	42082	50.9
	2017-03-22	12:10:50	6.36 - 6.54	25.6	180	-122.8	32.4	43058	51.3
	2017-03-22	11:23:00	6.18 - 6.37	25.6	420	-126.3	36.6	43069	58.1
	2017-03-23	09:07:04	6.01 - 6.20	25.8	420	-106.7	50.1	42065	60.6
	2017-03-22	10:50:37	5.82 - 6.02	25.6	600	-128.7	39.4	43054	63.1
	2017-03-21	09:32:06	5.65 - 5.84	25.3	330	-105.0	48.4	42001	58.6
	2017-03-21	08:45:11	5.48 - 5.67	25.3	660	-109.1	52.1	42011	62.9
	2017-03-17	09:37:31	5.35 - 5.51	24.4	660	-108.9	49.7	42996	59.2
AFGL 2136	2019-04-24	10:00:12	7.83 - 8.01	40.5	256	-104.4	36.3	43014	51.8
	2017-03-23	11:55:34	7.67 - 7.85	43.8	1170	-117.6	34.5	43063	51.3
	2017-03-17	11:13:03	7.51 - 7.69	43.5	840	-110.5	38.8	44962	60.2
	2017-03-17	11:55:32	7.34 - 7.52	43.5	660	-114.7	36.0	45008	55.7
	2017-05-25	09:57:59	7.19 - 7.37	30.0	810	-121.9	38.7	43008	51.7
	2017-05-25	10:39:58	7.02 - 7.20	30.0	840	-128.8	39.4	45012	53.1
	2017-03-21	10:47:40	6.87 - 7.05	43.7	1200	-109.3	36.5	43008	56.8
	2017-03-21	11:54:08	6.69 - 6.88	43.7	1140	-117.0	32.7	43008	50.0
	2017-03-23	10:46:19	6.53 - 6.71	43.8	1440	-110.0	37.4	43083	56.3

2017-03-16	11:34:59	6.36 - 6.54	43.4	1230	-122.4	37.2	43995	60.9
2019-04-17	10:01:58	6.18 - 6.37	41.9	256	-95.1	35.4	42997	51.7
2019-04-17	08:35:48	6.01 - 6.20	41.9	256	-83.7	39.2	43006	56.5
2019-04-17	11:10:48	5.82 - 6.02	41.9	256	-105.2	34.5	43008	47.2
2019-04-23	10:19:34	5.65 - 5.84	40.7	256	-101.1	35.9	43011	49.7
2019-04-19	10:01:54	5.48 - 5.67	41.5	256	-114.8	41.9	43012	61.4
2019-04-23	11:29:01	5.35 - 5.51	40.7	256	-112.2	35.0	43015	48.2

The EXES data were reduced with the SOFIA Redux pipeline (Clarke et al. 2015), which has incorporated routines originally developed for the Texas Echelon Cross Echelle Spectrograph (TEXES) (Lacy et al. 2003). The science frames were de-spiked and sequential nod positions subtracted, to remove telluric emission lines and telescope/system thermal emission. An internal blackbody source was observed for flat fielding and flux calibration and then the data were rectified, aligning the spatial and spectral dimensions. The wavenumber solution was calibrated using sky emission spectra produced for each setting by omitting the nod-subtraction step. We used wavenumber values from HITRAN (Rothman et a. 2013) to set the wavelength scale. The resulting wavelength solutions are accurate to 0.3 km s^{-1}.

Standard star spectra were taken for several settings but were found to be of insufficient quality to be effective. In general these spectra were too noisy such that they needed to be smoothed so much that the required telluric lines were also smoothed out, making them ineffective at dividing out the atmosphere. In some cases the standard star exhibited emission features which resulted in spurious absorption features being divided into the final spectrum. One advantage of using a standard star spectrum is that, if taken straight after the science target spectrum, the baseline is largely the same as that of the science target. This allows for efficient removal of the erratic baseline and fringing that were present. We found however that the use instead of an atmospheric model, in this case from ATRAN, proved to be much more effective in removing the atmosphere. While the ATRAN model provided a more governable way of removing the atmosphere, allowing line widths to be controlled, fringing was not removed from our data. Due to the fact that the pwv metre was not working, ATRAN models were constructed at a fixed observatory altitude of 43,000 ft, and the depths of the telluric model lines were then adapted to the observed telluric lines by multiplying the model to a power, denoted Z:

$$F = \frac{F_0}{F_m^{(AZ)}} \tag{4.1}$$

where F, F_0 and F_m are the final, original and model spectra respectively, and A is the airmass, following recommendations by the instrument team and outlined in Figure 4.1. The use of telluric model in future studies would reduce the large amount of additional time required to observe a standard star spectrum.

4.2.1 Source Description

The mid-IR continuum of AFGL 2136 and AFGL 2591 is thought to originate from a disk around these massive protostars (Preibisch et al. 2003; Monnier et al. 2009; de Wit et al. 2011; Boley et al. 2013). In the case of AFGL 2136, the mid-IR continuum has been attributed to an inner dust rim with a radius of > 125 AU. The absence of small dust grains in the inner 125 AU has been attributed to excavation by photoevaporation (Monnier et al. 2009; de Wit et al. 2011; Frost et al. 2021). For AFGL 2591, a similar scenario is suggested with an absence of grains that contribute to the mid-IR continuum in the inner 65 AU (Preibisch et al. 2003; Monnier et al. 2009), although the exact radius is not well determined due to uncertainties in the adopted distance to this source. The inner 130 AU of AFGL 2136 is observed to

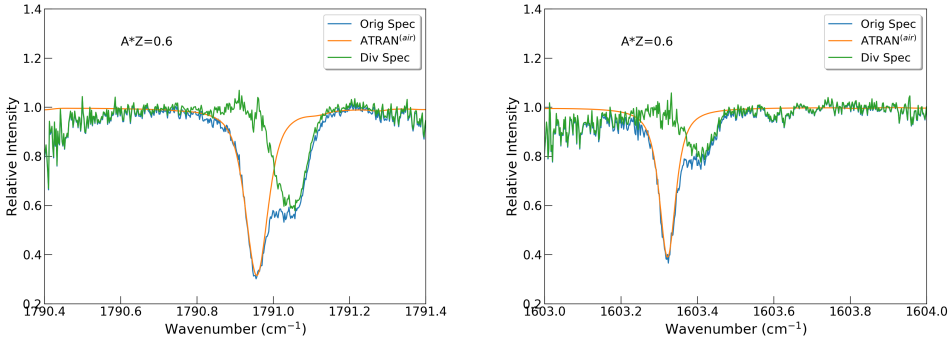

Figure 4.1: Two examples of absorption lines from AFGL 2136 from different wavelength settings illustrating the division of the telluric lines with the ATRAN model. The original spectrum is shown in blue, the ATRAN model is shown in orange, and the original spectrum divided by the ATRAN model is shown in green. The ATRAN model is scaled by multiplying the model to the power airmass to achieve a good match.

be gaseous, with a Keplerian disk observed in vibrationally excited H_2O emission detected with the Atacama Large Millimetre Array (ALMA) (Maud et al. 2019). As the emitting level is 3462 K above ground, this emission is associated with very hot gas. Coexisting with the H_2O disk are large grains (mm-size or larger) which create the sub-mm continuum and have not been photoevaporated. The sub-mm continuum is observed to cover the same extent as the gas, of around 120 AU in radius. This places the dust and gas observed at sub-mm wavelengths within the proposed dust rim responsible for the mid-IR continuum. There is evidence for a disk wind in AFGL 2136 from radial motion in the disk which could be driven by the star, supported by the detection of very compact H30α emission potentially driving an ionised disk wind (Maud et al. 2018). de Wit et al. (2011) and Frost et al. (2021) find that a hot zero-age main sequence star is too faint to provide enough N-band flux to explain the visibilities observed with the MIDI instrument on the Very Large Telescope Interferometer (VLTI). To reconcile this they propose the presence of a bloated star which contributes a few % to the total N-band flux to match the observations, in any case implying that the main source of continuum is the disk and not the central protostar. Both YSOs are associated with elongated thermal radio emission coinciding with the protostar and elongated parallel to the outflow axis (Trinidad et al. 2003; Menten & van der Tak 2004), indicative of photo-ionization of a jet-generated cone surface (Tan & McKee 2003; Tan 2008; Tanaka et al. 2016, 2017). Size estimates for these compact radio emission sources are 65 AU (Menten & van der Tak 2004) for AFGL 2136 and < 100 AU (van der Tak et al. 1999) for AFGL 2591, at the adopted distance of 3.3 kpc (Sanna et al. 2012).

4.3 Analysis

The data presented in this paper are part of a high resolution spectral survey of the 4-13 μm region of two massive young stellar objects (YSOs) AFGL 2591 VLA3 (hereafter AFGL 2591) and AFGL 2136 IRS1 (hereafter AFGL 2136). A limited set of water absorption lines in carefully selected, narrow, spectral windows has been analysed by (Indriolo et al. 2015a) and (Indriolo et al. 2020) for AFGL 2591 and AFGL 2136, respectively. In this work we build on these studies using the H_2O data from the full 5-8 μm spectral survey, containing 209 H_2O lines in AFGL 2136, and 240 lines in AFGL 2591, in the v_2=1-0 and v_2=2-1 ro-vibrational transitions of the ν_2 band. These are the numbers of lines used in this study, with many more lines having to be discarded due to the reasons outlined below.

Due to many challenges with the data reduction, the absorption lines were analysed on a line-by-line basis, instead of applying a global reduction to the spectrum as a whole. This involved normalising the science target spectrum, matching the continuum of the science spectrum and atmospheric model, and dividing the atmosphere out from each echelle order where the given absorption line was present (Fig 4.1). A first order polynomial representing the continuum was then fit over the absorption line which was then divided by this continuum to achieve a flat baseline. Naturally this introduced some systematic error in the continuum placement as not for every case was it clear where the continuum should go, and removing the baseline fluctuations was not possible since the orders could not be merged in this method. A further systematic uncertainty in the fit was poor removal of the telluric lines in places. The systematic uncertainties are estimated to be negligible to up to a factor of 0.75 of the error on the equivalent width (derived from the statistical noise) depending on the absorption line. Transitions that were blended with very deep telluric lines were discarded since it was not possible to recover the line profiles of these transitions. Likewise lines that were blended with other hot core lines were discarded.

Lines were fitted in velocity space, with either one or two gaussians depending on which was appropriate. The variables of the gaussian model were the peak velocity, v_{lsr}, velocity dispersion parameter, σ_v and the line depth. For AFGL 2136 the v_{lsr} was constrained between 24 and 28 km s^{-1} for the first component and 32 and 36 km s^{-1} for the second component. For both components, σ_v was constrained between 1 and 6 km s^{-1}. In the case of AFGL 2591, the first component was constrained to a v_{lsr} between -18 and -7 km s^{-1}. It was not possible to set the v_{lsr} of the second component as a free parameter, due to the heavy blending of the velocity components. Instead this was chosen such that it was, for all transitions, 14 km s^{-1} blue-shifted with respect to the v_{lsr} of the first component. The value of 14 km s^{-1}, however, has a certain error associated with it. This will be discussed further in section 4.4. Both components were fit with σ_v between 1 and 8 km s^{-1}. The line widths have been deconvolved with the instrument profile.

Rotation diagrams presented in section 4.4 are created using the Boltzmann equation. The column density in the lower ro-vibrational level is calculated using the optically thin relation:

$$N_i = \frac{g_l}{g_u} \frac{8\pi}{A_{ul}\lambda_{ul}^3} \int \frac{\tau_i(v)}{\phi_i(v)} dv \tag{4.2}$$

where $i = 1, 2$ for the two velocity components. N_i is the column density of the lower level, g_l and g_u are the statistical weights for the lower and upper level respectively, A_{ul} is the spontaneous emission coefficient for the transition, λ_{ul} is the wavelength of the line, $\tau(v)$ is the optical depth profile of the line in velocity space, and $1/\phi(v)$ is equal to 1 for an integrated line. If the lines are optically thin and LTE is a valid assumption, data points on the rotation diagram follow a straight line with slope -1/T_{rot}, with temperature T_{rot}.

4.3.1 Foreground Absorption

In order to attend to the effects of optical depth, we introduce a curve of growth analysis that is based on the assumption of a background light source seen through a dust-free absorbing slab of gas. The theoretical curve of growth can be approximated by:

$$\frac{W_\lambda}{b f_c \lambda} \sim \frac{\sqrt{\pi}}{c} \frac{\tau_p}{1 + \tau_p/2\sqrt{2}} \tag{4.3}$$

for $\tau_p < 1.254$ and:

$$\frac{W_\lambda}{b f_c \lambda} \sim \frac{2}{c} \sqrt{\ln[\tau_p/\ln 2] + \frac{\gamma\lambda}{4b\sqrt{\pi}}(\tau_p - 1.254)} \tag{4.4}$$

for $\tau_p > 1.254$, taken from Tielens (2021) with the additional factor $1/f_c$ to take into account a covering factor. Here W_λ is the equivalent width, λ is the wavelength, τ_p is the peak optical depth, b is the the Doppler width and γ is the damping factor. The Doppler parameter, b, is related to the velocity dispersion via $b = \sqrt{2}\sigma_v$. The expression for τ_p is given by:

$$\tau_p = \frac{\sqrt{\pi} e^2 N_l f_l \lambda}{m_e c b} \tag{4.5}$$

where N_l and f_l are the column density and oscillator strength in the lower level, respectively, e is the electron charge, m_e is the electron mass and τ_p is integrated over wavelength. In the empirical curve of growth, we introduce an additional parameter, f_c, the covering factor of the absorbing gas, which is divided into the equivalent width (e.g., the left hand side of equations 4.3 & 4.4 become $W_\lambda/b\lambda f_c$). This parameter describes the covering of the background illuminating source, where a smaller covering factor will result in a smaller observed equivalent width.

The level populations are related as follows,

$$N_l = \frac{g_l N}{Q(T)} e^{-E_l/T} \tag{4.6}$$

where Q(T) is the partition function, N is the total column density of the species, E_l is the energy of the lower level in kelvin and T is a free parameter that will be of order of T_{rot}.

4.3.2 Disk Atmosphere

Alternatively, we consider the stellar atmosphere model developed in chapter 3 and construct curves of growth in this regime also, following the stellar atmosphere theory of Mihalas (1978). Curves of growth in this approximation are constructed using the equation:

$$\frac{W}{2Y\Delta\nu} = \int_0^\infty \frac{\eta_0 H(a,v)}{1+\eta_0 H(a,v)} dv \tag{4.7}$$

where W is the equivalent width of the absorption lines in frequency space, $\Delta\nu$ is the Doppler width in units of Hz, and Y takes into account the temperature gradient in the atmosphere. For the derivation and definition of Y, see Appendix A of chapter 3. $H(a,v)$ is the Voigt profile as a function of the frequency shift, v (in velocity space and normalised to the Doppler parameter), and a the damping parameter (in Doppler units). The latter only plays a role on the square root portion of the curve of growth which is not relevant here. The right-hand side of this equation can be calculated as a function of η_0, resulting in a theoretical curve of growth. We have used the simple approximations to this provided by (Mihalas 1978). η_0 is the opacity at line centre set relative to the continuum opacity given by:

$$\eta_0 = \frac{\kappa_L(\nu=\nu_0)}{\kappa_c} = \alpha \frac{A_{ij}\lambda^3}{8\pi\sqrt{2\pi}\sigma_v} \frac{g_u}{g_l} \frac{X_l}{X_{CO}} \tag{4.8}$$

where X_l is the abundance in the lower level and α is set by the requirement that the CO abundance, X_{CO}, is 10^{-4}, which results in $\alpha = 1.3\times10^{19}$ and 2.3×10^{18} for AFGL 2136 and AFGL 2591, respectively.

As in the curve of growth for equations 4.3 to 4.5, the level populations are related by equation 4.6, with the difference that it is no longer the column density of the lower level but the abundance with respect to H nuclei; and thus N is replaced by the total abundance with respect to H, $X(H_2O)$. Adopting an abundance, temperature, and Doppler parameter for the absorbing gas, the left-hand side of equation 4.7 as well as η_0 can be calculated for each line, resulting in an empirical curve of growth.

Empirical curves of growth are created for a range of different values of T and $X(H_2O)$ and these are fit to the theoretical curve of growth. This fit is quantified by a least square process where the best combination of T and N or $X(H_2O)$ is chosen such that the reduced χ^2 is the lowest. The errors on these best fit parameters are taken from the 1σ contour in the corresponding error plot. These contour plots have been normalised to the minimum reduced χ^2 from the fitting procedure.

4.4 Results

4.4.1 AFGL 2136

For AFGL 2136 we only focus on the velocity component with peak velocity fit between 24 and 28 km s^{-1} since this is the main absorbing component seen also in HCN, C_2H_2, NH_3 and CS (chapter 3). For the v_2=1-0 band, all peak velocities are in agreement and there is no evidence for any velocity trends with opacity. We derive

an average value of 25.5±1.1 km s^{-1} for the v_{lsr}. There is however an overall increase of the line width with η_0, by a factor of 2, shown in Figure 4.2. Figure 4.3 illustrates that lines with high opacity are clearly broader.

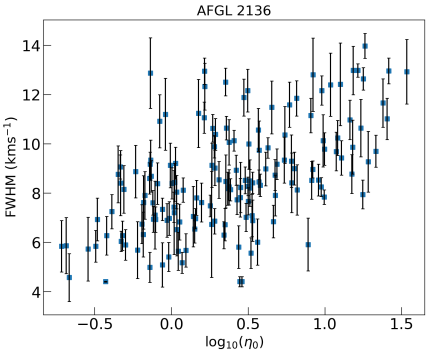

Figure 4.2: Trend between η_0 with the line width in AFGL 2136.

As was noted by Indriolo et al. (2020), the rotation diagram shows a large scatter that cannot be accounted for by the error bars (Figure 4.4). This is evident by the under-prediction of the column density of a number of lines, most prominent for those with high η_0 values i.e., high Einstein A coefficients and/or high column densities. As a result of this, the temperature and column density derived from the rotation diagram do not reflect the true physical conditions. This effect is illustrated more clearly in Figure 4.5 which shows the column density of a number of levels for which we have multiple transitions. The individual transitions should yield the same column density but as this figure illustrates, lines with high η_0 systematically yield lower column densities.

The line profiles can give further insight where, in Figure 4.6, we plot absorption lines from the $7_{2,5}$ level against an LTE model that assumes an absorbing slab of gas which is not mixed with the dust, and fully covers the background source. In this model, the equivalent width of the optically thick lines would continue to increase with column density until they saturate at zero flux. Five lines are shown with varying η_0. Observed absorption lines do not go to zero, as would be expected for very optically thick lines in the assumption of an absorbing slab, but instead saturate at 40% relative to the continuum. Therefore lines with larger opacity exhibit a greater discrepancy with the absorbing slab model as the opacity increases. The behaviour presented in Figure 4.5 is a result of this saturation. Therefore a full curve of growth analysis is required.

We present the results of the curve of growth from the absorbing slab model for AFGL 2136 in Figure 4.7. We constrain f_c by the condition that this parameter must be equal to the depth of deepest absorption line (on a continuum-normalised flux scale). From Figure 4.6 we fix f_c to 0.4 for AFGL 2136. We then carried out the chi-squared fitting routine to find the best fit combination of T and N, for a range of different Doppler widths. We find a temperature of 457^{+13}_{-14} K and a column

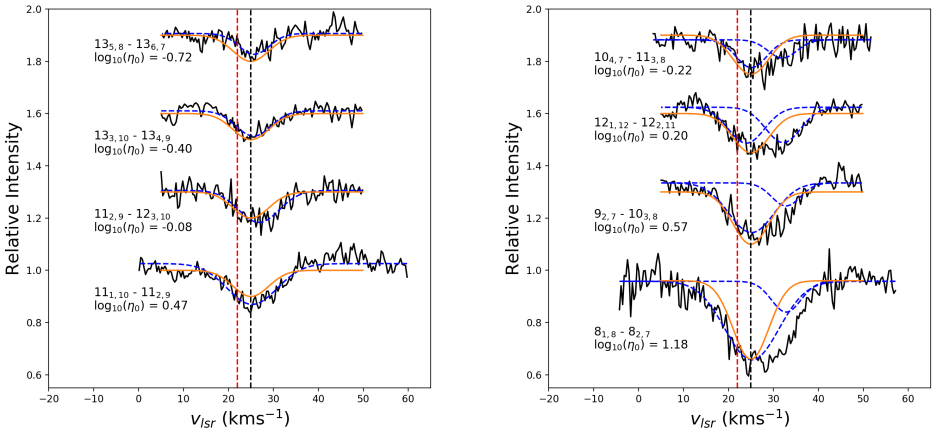

Figure 4.3: Line profiles of AFGL 2136 showing transitions of different opacity. Absorption lines are shown that exhibit one and two velocity components in the left and right panels, respectively. Shown in orange is a gaussian with a v_{lsr} of 25 km s^{-1} and a σ_v of 4 km s^{-1}. The blue dashed lines denoted the gaussian fits to each velocity component. The black dashed line at 25 km s^{-1} is added for a reference and the red dashed line at 22 km s^{-1} indicates the velocity of the gaseous envelope as observed at sub-mm wavelengths.

density $3.6^{+0.1}_{-0.1} \times 10^{18}$ cm^{-2}, for a Doppler width, b, of 3.75 km s^{-1}. This value of b corresponds to a value of 2.7 km s^{-1} for σ_v. While this is the best fit model, by eye the curve of growth does not fit well for the low opacity lines. A more linear behaviour for the low opacity lines is obtained for an excitation temperature of 600 K and a column density of $2.2{\times}10^{18}$ cm^{-2}, at the cost of an increased spread of the points around the theoretical curve of growth (and a higher chi-squared). This does not depend strongly on the adopted line width. The intrinsic σ_v may vary between 1 km s^{-1} - appropriate for thermal motion of this gas - and the observed line width of the narrowest lines (3.2 km s^{-1}), however line widths below 2.5 km s^{-1} do not fit the theoretical curve of growth. The chosen Doppler parameter introduces an uncertainty of 20% and 30% in the derived temperature and column density, respectively and does not noticeably improve the fit by eye in figure 4.7. The rotation diagram is corrected for optical depth effects by extrapolating the equivalent width for the calculated τ_p of each optically thick absorption line to a linear relation in the curve of growth. The rotation diagram is re-calculated, however the correction still shows considerable scatter (Fig 4.7).

We also pursue a curve of growth analysis based on the stellar atmosphere model presented in chapter 3. We calculate empirical curves of growth for a range of intrinsic line widths, with the constraint that σ_v must be greater than the thermal line width and less than the observed width of the optically thin lines. This sets boundaries for $1 \lessapprox \sigma_v \lessapprox 3.2$ km s^{-1}. Figure 4.8 shows the curve of growth under the assumption that lines are formed through a combination of absorption and scattering ($\epsilon = 0.5$; see chapter 3 for details). We find that the best fit value for the Doppler parameter

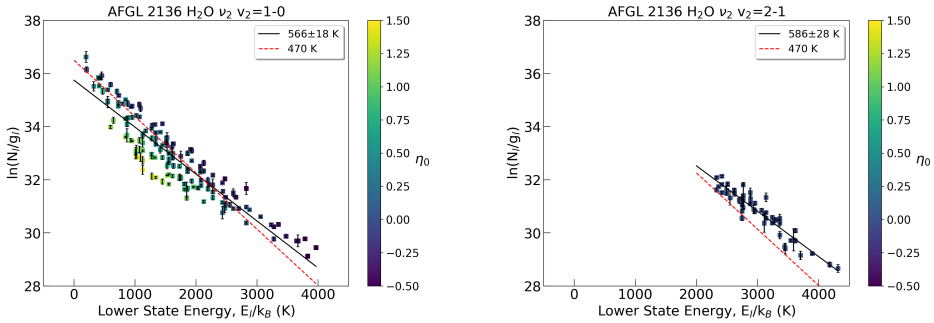

Figure 4.4: Rotation diagrams of the H_2O v=1-0 (*left*) and vibrationally excited v=2-1 (*right*) transitions of the ν_2 band in AFGL 2136. The colour bar is a function of $\log_{10}(\eta_0)$. The dashed red line denotes the temperature of 470 K derived from the curve of growth (see section 4.5.1). The solid black lines denote the fit to the rotation diagrams, and the temperatures of these fits are given in the legend.

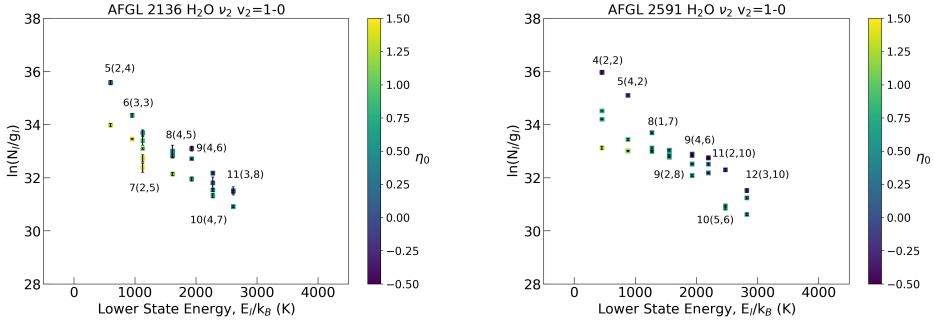

Figure 4.5: Rotation diagrams of AFGL 2136 and AFGL 2591 showing a selection of lines that have transitions out of the same lower level. These levels are indicated on the plots.

is for σ_v=3.0 km s^{-1}. The temperature and abundance with respect to CO are 470^{+24}_{-33} and $1.6^{+0.3}_{-0.1}$, respectively. This temperature is consistent with CO, CS and NH_3 in this source, whereas the temperatures of HCN and C_2H_2 are higher by 200 K (chapter 3). The cases of line formation in the approximation of pure scattering ($\epsilon = 0$) and pure absorption ($\epsilon = 1$) are also considered and shown in Figures 4.9 and 4.10 respectively. For all cases we find that σ_v of 3.0 km s^{-1} provides the best fit. The derived temperature is not very dependent on the choice of ϵ, however the abundance increases from $0.5^{+0.1}_{-0.1}$ for $\epsilon = 1$, to $1.3^{+0.1}_{-0.2}$ for $\epsilon = 0$, to $1.6^{+0.3}_{-0.1}$ for $\epsilon = 0.5$. The correction to the rotation diagram is good for all ϵ, with a closer to linear result compared to the slab model.

The temperature obtained from the slab analysis agrees with the temperature from the stellar atmosphere analysis, within the errors. The best fit value for σ_v in the stellar atmosphere model is 3.0 km s^{-1}, compared to 2.7 km s^{-1} for the slab model. We note that we cannot directly compare the column density derived from

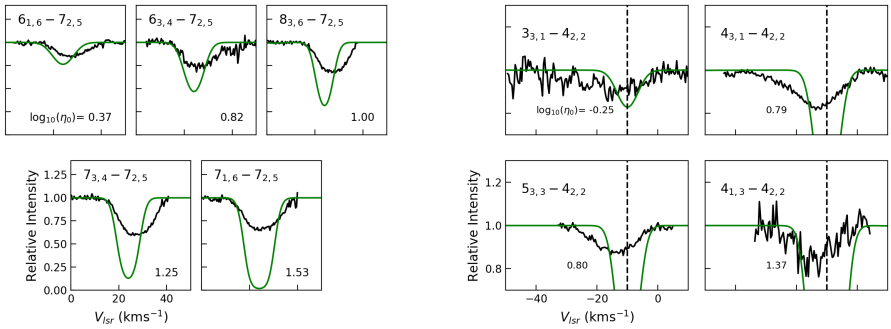

Figure 4.6: Absorption lines in AFGL 2136 of H_2O that trace the $7_{2,5}$ level (*left*) and the $4_{2,2}$ level in AFGL 2591 (*right*). The green solid line denotes a model of a background light source seen through a dust-free absorbing slab of gas, with f_c=1, generated at the physical conditions derived from the slab curves of growth. The opacities of each line, η_0, are indicated in the corresponding panels. The dashed vertical line in the plots for AFGL 2591 denotes -10 km s^{-1} for a reference.

the two methods. Goto et al. (2019) measured the ^{12}CO v=2-0 band and derived a temperature and column density of 530±80 K and 2.8±0.4 $\times 10^{19}$ cm^{-2}, respectively. With this column density we find a H_2O/CO ratio of 0.1. This is an order of magnitude lower than what we find for the H_2O abundance relative to CO from the stellar atmosphere model, however the v=2-0 band is at 2.3 μm therefore differing source sizes at difference wavelengths could have some effect. The derived physical conditions are summarised in Table 4.2 and all line parameters are given in Table 4.4 in the Appendix.

Four lines of $H_2^{18}O$ are detected in AFGL 2136 and curves of growth are shown in Figure 4.11. The temperature we derive is 252^{+7}_{-12} K and 260^{+11}_{-67}, for the stellar atmosphere and slab models respectively. This is lower than the temperature for $H_2^{16}O$ which may reflect the fact that these lines have lower energy levels, therefore probe colder gas. The abundance with respect to CO is $3.6^{+0.3}_{-0.3} \times 10^{-3}$, which results in a $^{16}O/^{18}O$ ratio of 444±83, consistent with the standard ISM value of 500 (Wilson & Rood 1994).

For the vibrationally excited v_2=2-1 band, absorption line profiles are consistent with each other and no evidence for trends in peak velocity or line width is present. The average σ_v and v_{lsr} for the v_2=2-1 band are 3.1±1.0 km s^{-1} and 25.7±1.3 km s^{-1}, respectively. This is in good agreement with the v_2=1-0 band. In the rotation diagram, all transitions can be fit with a straight line. All lines have very low values for η_0 therefore will lie on the linear part of the curve of growth. We therefore derive the temperature and abundance/column density for this band from the rotation diagram. These parameters are summarised in Table 4.2. Given the measured relative populations of the v=1-0 and v=2-1 vibrational states of H_2O, we derive a vibrational temperature of 452±57 K for H_2O, very close to the rotational temperature. The full line parameters for the v=2-1 transition are given in Table 4.4.

The ν_3=1-0 band at 2 μm was observed in absorption by Indriolo et al. (2020). All lines lie in a straight line in the rotation diagram indicative of optically thin

gas, therefore this band likely gives a reliable handle on the temperature, 502±12 K, however some lines do not reach the depth predicted by the absorbing slab model, so there are optical depth effects, also at 2 μm.

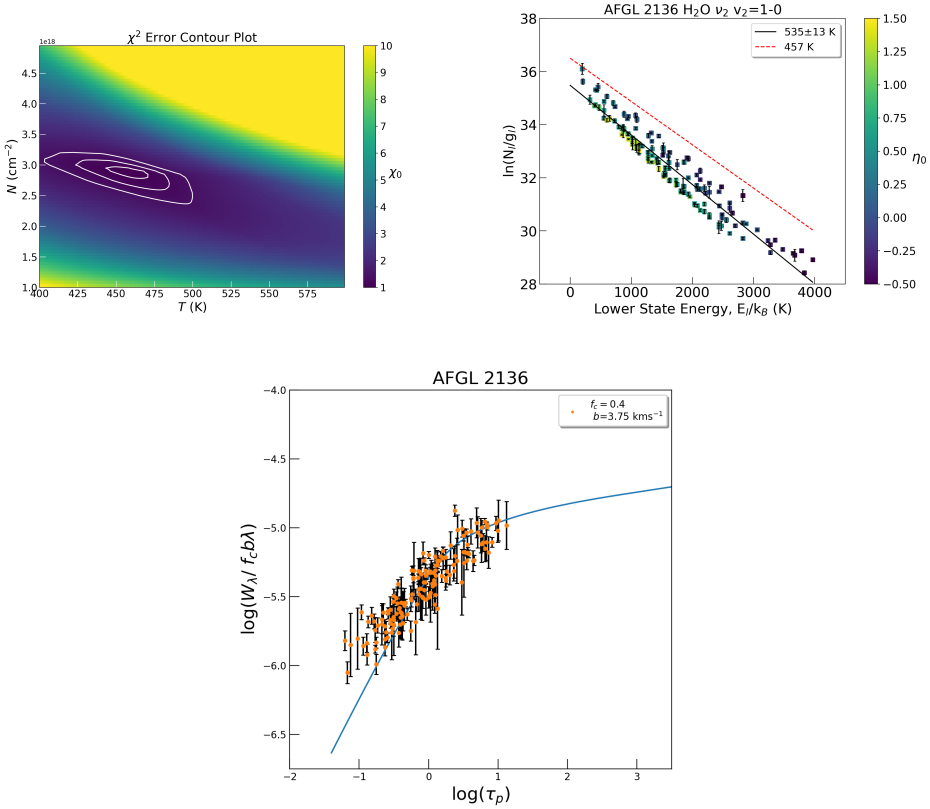

Figure 4.7: *bottom:* The curve of growth for the v=1-0 transition of AFGL 2136 for the slab model, taking a covering factor of 0.4 and b=3.75 km s^{-1}. The best fit empirical curve of growth is shown and the corresponding best fit temperature and column density are indicated. *top left*: The error on the parameters is given in the contour plot where the colour scale is the reduced χ^2 value. The contours represent the 1σ, 2σ and 3σ uncertainty levels. *top right:* The column densities for the optically thick lines were determined using the curve of growth. The best fit temperature of 457 K from the slab curve of growth is represented by the red dashed line. The black solid lines are fits to the corrected data set and the corresponding temperatures are indicated for each case.

4.4.2 AFGL 2591

The absorption line profiles in AFGL 2591 are complex. The systemic velocity of the envelope of this source is $v_{lsr} = -5.5$ km s^{-1} (van der Tak et al. 1999; Wang et al. 2012; Gieser et al. 2019). The presence of two velocity components is obvious in several examples, one at -10 km s^{-1} and one at -25 km s^{-1} (Figure 4.12) and we

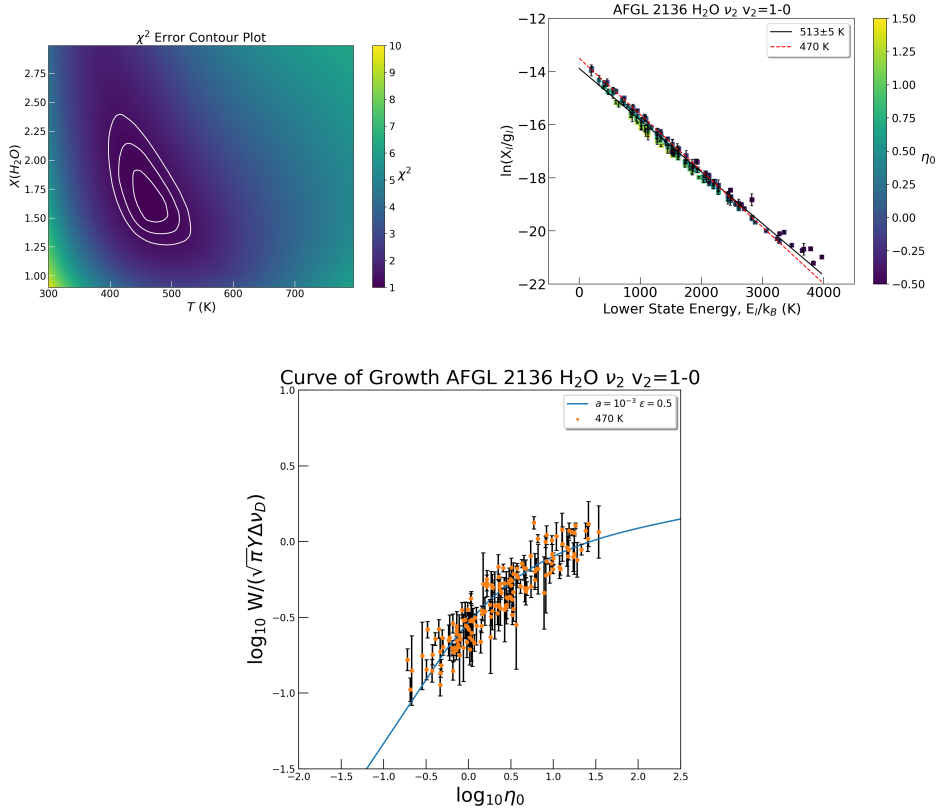

Figure 4.8: *bottom:* The curve of growth for the v=1-0 transition of AFGL 2136 for the stellar atmosphere model. The theoretical curve is for the case of a mixture of absorption and scattering. The best fit empirical curve of growth is shown and the corresponding best fit temperature and abundance are indicated. *top left*: The error on the parameters is given in the contour plot where the colour scale is the reduced χ^2 value. The contours represent the 1σ, 2σ and 3σ uncertainty levels. The H_2O abundance is quoted relative to CO. *top right:* The rotation diagram is a function of η_0 and the abundances for the optically thick lines were determined using the curve of growth. The best fit temperature of 470 K from the curve of growth is represented by the red dashed line. The black solid lines are fits to the corrected data set and the corresponding temperatures are indicated for each case. Note that the y-axis is the abundance in the lower level based on the stellar atmosphere theory.

refer to these as the major and minor components, respectively. There is no consistent trend in A or E_l for the presence and/or strength of the minor velocity component e.g. some strong lines show only one component whereas some show two, and some lines with equivalent energies show both one and two components (Figure 4.12). This may reflect different excitation conditions in the minor component compared to the major one. Due to the heavy blending of the two velocity components, in order to achieve reasonable fits the v_{lsr} of the minor component could not be left a free parameter in the fitting routine, and instead had to be fixed to a certain velocity.

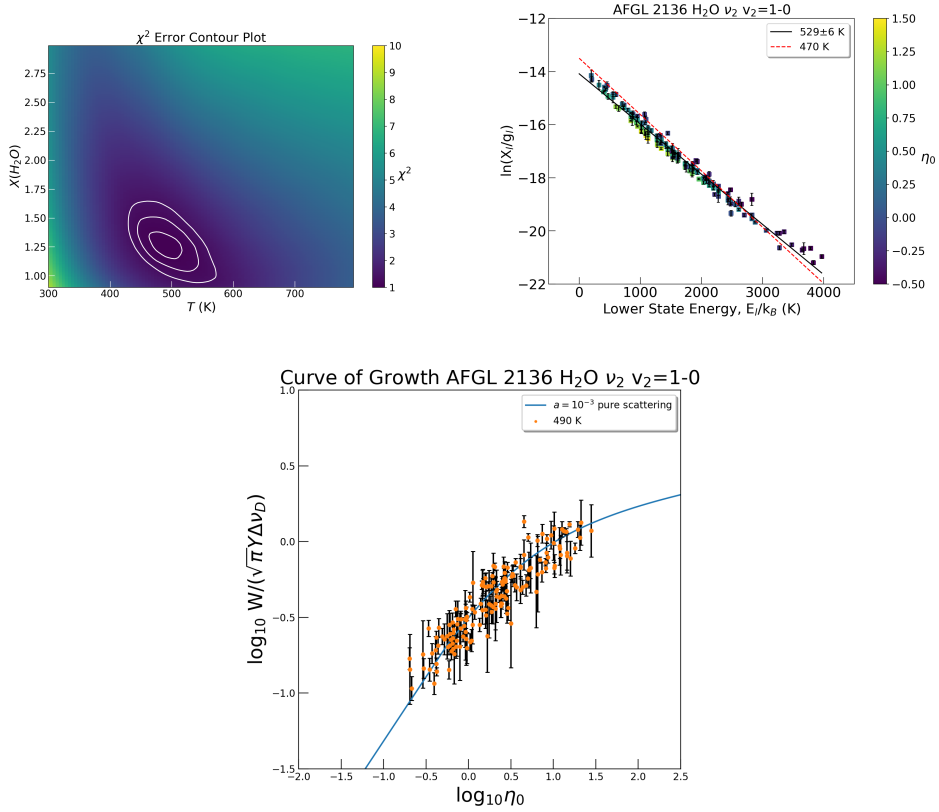

Figure 4.9: *bottom:* The curve of growth best fit for the case of pure scattering. *top left:* The error on the parameters is given in the contour plot where the colour scale is the reduced χ^2 value. The contours represent the 1σ, 2σ and 3σ uncertainty levels. The H_2O abundance is quoted relative to CO. *top right:* The rotation diagram is a function of η_0 and the abundances for the optically thick lines were determined using the curve of growth. The best fit temperature of 470 K from Table 4.2 is represented by the red dashed line. The black solid lines are fits to the corrected data set and the corresponding temperatures are indicated for each case.

In contrast to AFGL 2136, the v_2=1-0 band reveals variations in the peak velocity, with some lines appearing shifted with respect to each other. There is a general trend between the peak velocity and the opacity of the transition (Figures 4.12 & 4.13). This is the case for all lines, whether the minor component is present or not. As a result of this trend, the v_{lsr} of the minor component also changes, since it is the composite line profile that shifts. In order to minimise uncertainty of the placement of the minor component, we applied a constraint that the two velocity components should be separated by the same amount; 14 km s^{-1} for all transitions. However it is not possible to achieve this exactly, as we fix the velocity of the minor component and allow the velocity of the major component to vary. Thus the peak velocity of the major component pre-fitting was estimated by eye, looking at the composite line

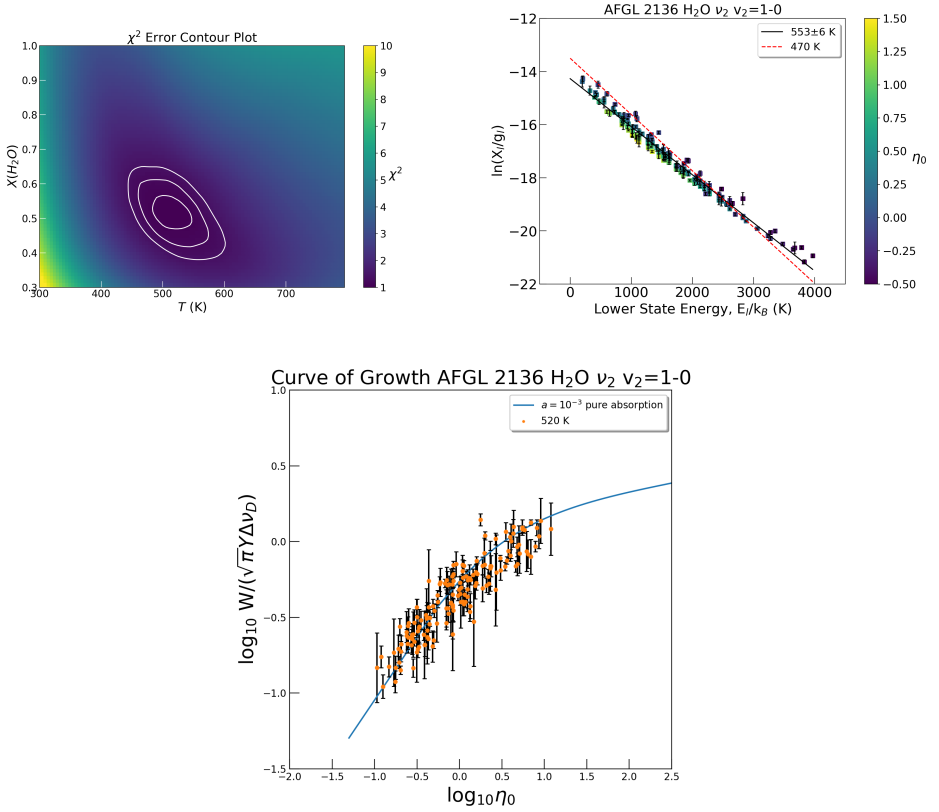

Figure 4.10: *bottom:* The curve of growth best fit for the case of pure absorption in AFGL 2136. *top left:* The error on the parameters is given in the contour plot where the colour scale is the reduced χ^2 value. The contours represent the 1σ, 2σ and 3σ uncertainty levels. The H_2O abundance is quoted relative to CO. *top right:* The rotation diagram is a function of η_0 and the abundances for the optically thick lines were determined using the curve of growth. The best fit temperature of 470 K from Table 4.2 is represented by the red dashed line. The black solid lines are fits to the corrected data set and the corresponding temperatures are indicated for each case.

profile. Then the peak velocity for the minor component to be used in the fitting was chosen based on this estimate. Naturally this leads to some uncertainties in the placement of the minor velocity component, and therefore, most importantly, the integrated line strength of the major velocity component. A separation of 14±1 km s^{-1} between the two components is more accurate, and this constraint gives a good fit to to the line profiles and curve of growths. Not accounting for the shift of the minor component introduces a large scatter in the curve of growth. Furthermore we note the lines show an overall variation in line width, illustrated in Figure 4.13. Referring to the results below, we note that this line width increases with increasing η_0.

This trend has been observed previously by Indriolo et al. (2015a), however these authors fit only 1 velocity component to every line. We have fitted two gaussian

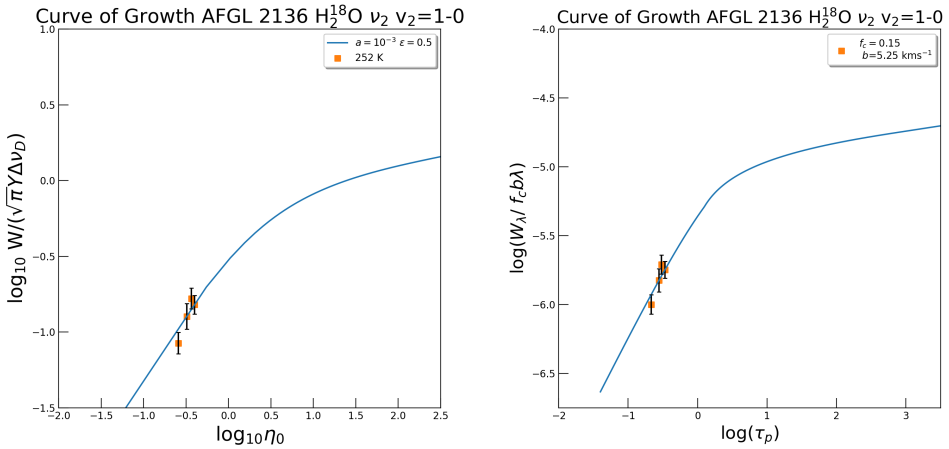

Figure 4.11: The curve of growth for $H_2^{18}O$ in AFGL 2136. The stellar atmosphere curve of growth assumes line formation by a combination of absorption and scattering.

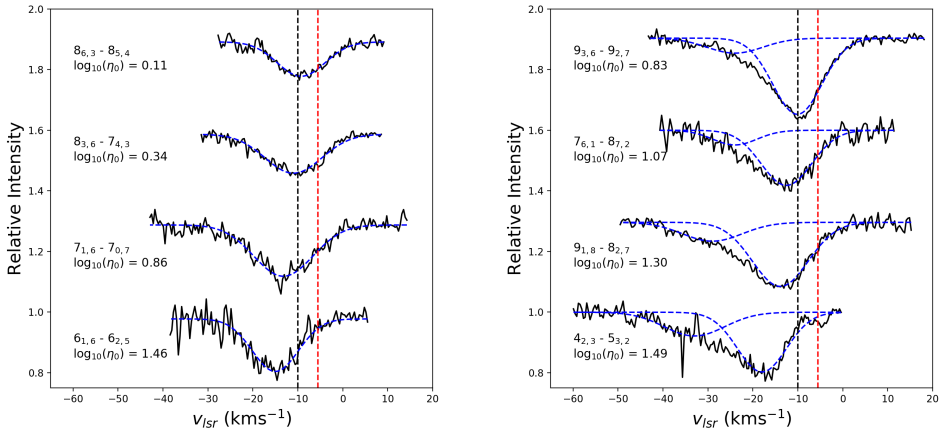

Figure 4.12: Line profiles of AFGL 2591 showing the trend in peak velocity with η_0. Transitions are shown that exhibit one and two velocity components in the left and right panels, respectively. The blue dashed lines denoted the gaussian fits to each velocity component. The black dashed line at -10 km s^{-1} is added for a reference and the red dashed line at -5.5 km s^{-1} indicates the velocity of the gaseous envelope as observed at sub-mm wavelengths.

components, but the two velocity components are not well resolved. Thus, combined with the trends in peak velocity and line width, we are limited in terms of the line fitting. It was not possible to accurately determine the physical conditions of the minor component since it is too weak and difficult to disentangle from the major component.

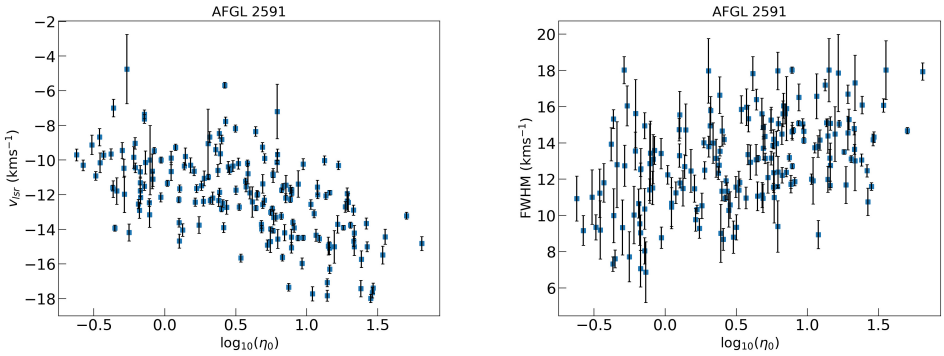

Figure 4.13: Plots illustrating the relationship between η_0 and the peak velocity and line width in AFGL 2591 on the left and right, respectively.

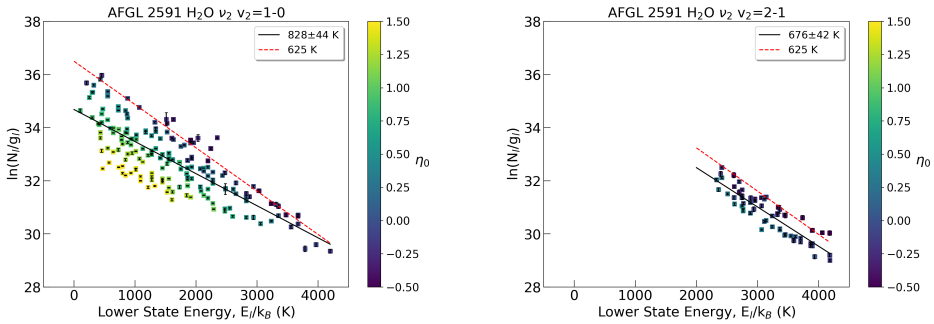

Figure 4.14: Rotation diagrams of the H_2O v=1-0 (*left*) and vibrationally excited v=2-1 (*right*) transitions of the ν_2 band in AFGL 2591. The colour bar is a function of $\log_{10}(\eta_0)$. The dashed red line denotes the temperature of 625 K derived from the curve of growth. The solid black lines denote the fit to the rotation diagrams, and the temperature of this fit is given in the legend.

The rotation diagrams for the v_2=1-0 and v_2=1-2 bands are shown in Figure 4.14. For the v_2=1-0 band, the scatter is far more accentuated compared to what is seen in AFGL 2136. Therefore the rotation diagrams do not reflect the true physical conditions and a curve of growth analysis is required. Figure 4.5 illustrates this point for levels which trace the same lower level across a range of energies.

As in AFGL 2136, Figure 4.6 shows that absorption lines do not go to zero flux, even when they have very large opacities. Four lines from the $4_{2,2}$ level are shown. These lines should have the same column density as they originate from the same lower level, however this is not the case as shown in Figure 4.5. Absorption lines saturate at 15% relative to the continuum, and therefore lines with larger and larger opacity exhibit a greater discrepancy with the absorbing slab model. Saturation occurs at a lower flux than in AFGL 2136, hence the more extreme scatter in the rotation diagram compared to AFGL 2136.

We show the results of the curve of growth analysis in the approximation of an absorbing slab for AFGL 2591 in Figure 4.16. As a result of the complexity of the line profiles, the scatter in the curve of growth for AFGL 2591 is dominated by systematic error. Therefore we determine the fit to the curve based only on lines that show a single velocity component and then apply the derived physical conditions to the data set as a whole. Again we fix the value for f_c from Figure 4.6. This sets a value of approximately 0.15 for AFGL 2591. We find a best fit temperature and column density of 541^{+1}_{-8} K and $1.5^{+0.1}_{-0.1} \times 10^{19}$ cm^{-2}, respectively. The value for b which gave the lowest chi-squared value was 5.25 km s^{-1}. This value for b corresponds to a value of 3.7 km s^{-1} for σ_v. For AFGL 2591, we fix σ_v between 1 and 4 km s^{-1}.

The curve of growth in Figure 4.17 for the stellar atmosphere model gives a temperature and abundance with respect to CO of 625^{+27}_{-22} and $7.4^{+0.5}_{-0.4}$ respectively, assuming $\epsilon = 0.5$. The best fit value for σ_v in this case is 2.75 km s^{-1}. For the other processes of lines formation we find different values of σ_v fit better, with 2.0 km s^{-1} and 1.5 km s^{-1} for $\epsilon = 0$ and $\epsilon = 1$, respectively. These curves of growth are shown in Figures 4.18 and 4.19. We also find that the abundances are different with $7.9^{+0.6}_{-0.5}$ and $4.2^{+0.3}_{-0.2}$ for ϵ of 0 and 1, respectively, while the temperature varies by only 25 K.

Comparing the slab analysis to the stellar atmosphere analysis, we find that for AFGL 2591, the temperatures are significantly different, but agree within the 3σ error bars, with 541^{+11}_{-21} K and 625^{+82}_{-70} K, respectively. Taking the column density of $9.3{\times}10^{16}$ cm^{-2} for ^{13}CO (Mitchell et al. 1990) and a ^{12}C/^{13}C ratio of 60, we find a H_2O/CO ratio of 2.7, using the water column density derived from the slab model. This is a factor of 2-4 lower than what we derive from the stellar atmosphere curve of growth, depending on the value of ϵ. The corrected rotation diagrams for the stellar atmosphere approach are better than those for the slab model, although the slab model still does a good correction. The physical conditions are summarised in Table 4.2. All line parameters are given in Table 4.7 in the Appendix.

In the v_2=2-1 band of AFGL 2591, the rotation diagram suggests that these lines are also optically thick with $\log_{10}(\eta_0)$ approaching 1. This is confirmed by the fact that there is an overall increase in the line width with η_0. We therefore carry out a curve of growth analysis using the stellar atmosphere model on this band as well to determine the physical conditions. The results are shown in Figure 4.15. There is no evidence for a velocity trend with opacity in this band and an average value of -10.2±0.4 km s^{-1} is derived for v_{lsr}. We derive a vibrational temperature of 504±61 K, for σ_v = 2 km s^{-1}. We did not consider $H_2^{18}O$ detected in our spectra of AFGL 2591. Two lines are present however were blended with other source lines, and most strong lines that should have been detected were not. All line parameters for the v=2-1 band are given in Table 4.8 in the Appendix.

H_2O line profiles agree well with those of the other molecules in this source. In a previous analysis, all species were fit with only one gaussian, assuming that absorption originated from one velocity component (chapter 3). A number of H_2O lines clearly reveal the presence of two velocity components, which is not obvious in the other molecules. If the other species were fit with two velocity components instead of one, the equivalent width of the lines would be lower and thus the abundances calculated would be reduced. We find that this is only a small effect, however, not more than a factor of 1.3. The HCN opacities are of the order of the optically thin H_2O lines. This

is reflected in the rotation diagram where the data lie along a straight line indicative of optically thin gas in LTE. Therefore the HCN lines could not have broadened after saturating at non-zero flux.

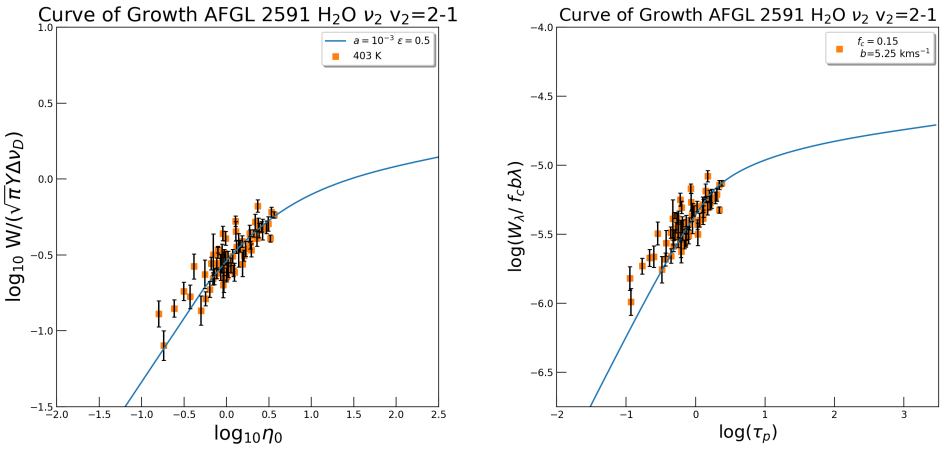

Figure 4.15: Curve of growth for AFGL 2591 v_2=2-1 band for the absorbing slab and stellar atmosphere models in the right and left panels, respectively. The best fit temperature and abundance are shown for both cases.

Table 4.2: H_2O Absorption Physical Conditions.

Source	Band	Number of Lines	Temperature (K)	Column Density (cm^{-2})	Temperature (K)	Abundance (w.r.t CO)
			Foreground Model		Atmosphere Model	
AFGL 2136	ν_2 $v_2 = 1 - 0$	154	457^{+13}_{-14}	$3.6^{+0.1}_{-0.1} \times 10^{18}$	470^{+24}_{-33}	$1.6^{+0.3}_{-0.1}$
	ν_2 $v_2 = 2 - 1$	55	585 ± 28	$3.9 \pm 0.1 \times 10^{16}$	585 ± 28	$9.2 \pm 0.4 \times 10^{-3}$
AFGL 2591	ν_2 $v_2 = 1 - 0$	177	541^{+1}_{-8}	$1.5^{+0.1}_{-0.1} \times 10^{19}$	625^{+27}_{-22}	$7.4^{+0.5}_{-0.4}$
	ν_2 $v_2 = 2 - 1$	63	418^{+28}_{-16}	$1.0^{+0.2}_{-0.2} \times 10^{17}$	403^{+27}_{-25}	$7.3^{+0.6}_{-0.4} \times 10^{-2}$

The column density and temperature derived from the slab model curve of growth are presented as well as the abundances and temperatures from the stellar atmosphere curves of growth with $\epsilon = 0.5$. Parameters of the ν_2 v_2=2-1 band in AFGL 2136 are taken from the rotation diagram. The upper and lower subscripts denote the 1σ error from the contour plots.

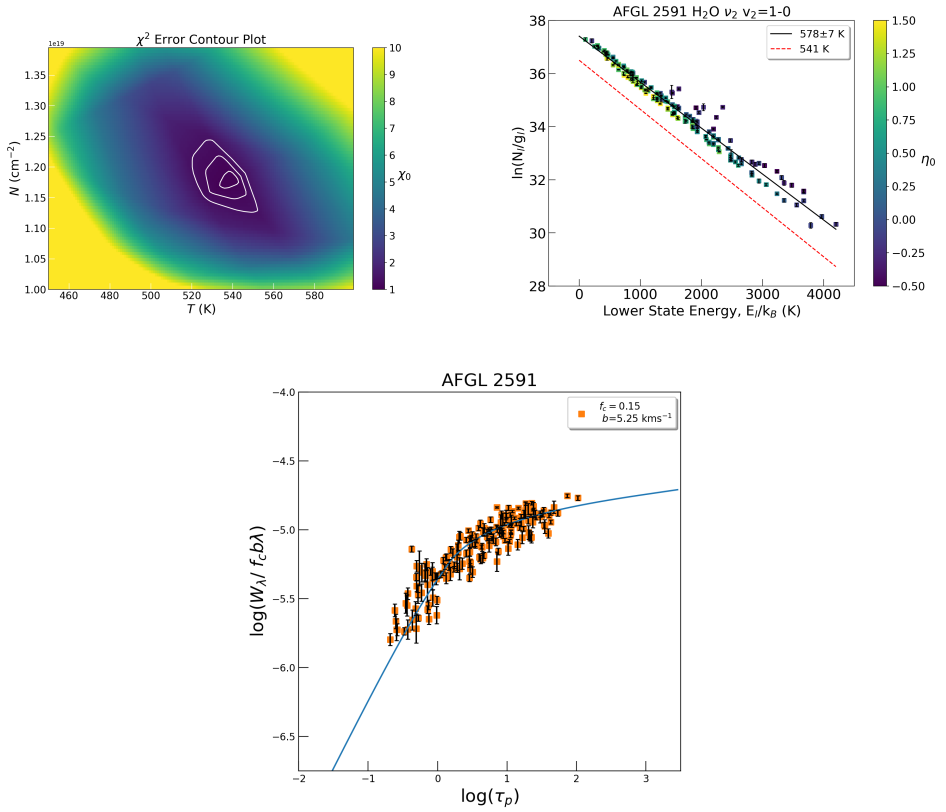

Figure 4.16: *bottom:* The curve of growth for the v=1-0 transition of AFGL 2591 for the slab model, taking a covering factor of 0.15 and b=5.25 km s^{-1}. The best fit empirical curve of growth is shown and the corresponding best fit temperature and column density are indicated. All lines are included here calculated at the conditions derived from the lines with one velocity component. *top left*: The error on the parameters is given in the contour plot where the colour scale is the reduced χ^2 value. The contours represent the 1σ, 2σ and 3σ uncertainty levels. *top right:* The best fit temperature of 541 K from the curve of growth is represented by the red dashed line. The black solid lines are fits to the corrected data set and the corresponding temperatures are indicated for each case.

4.5 Discussion

We have presented two scenarios to explain the absorption line data obtained from the spectral survey: foreground absorption and absorption in a disk atmosphere. Here, we will discuss the advantages and challenges of each model, and subsequently we will propose which model we regard as the most robust.

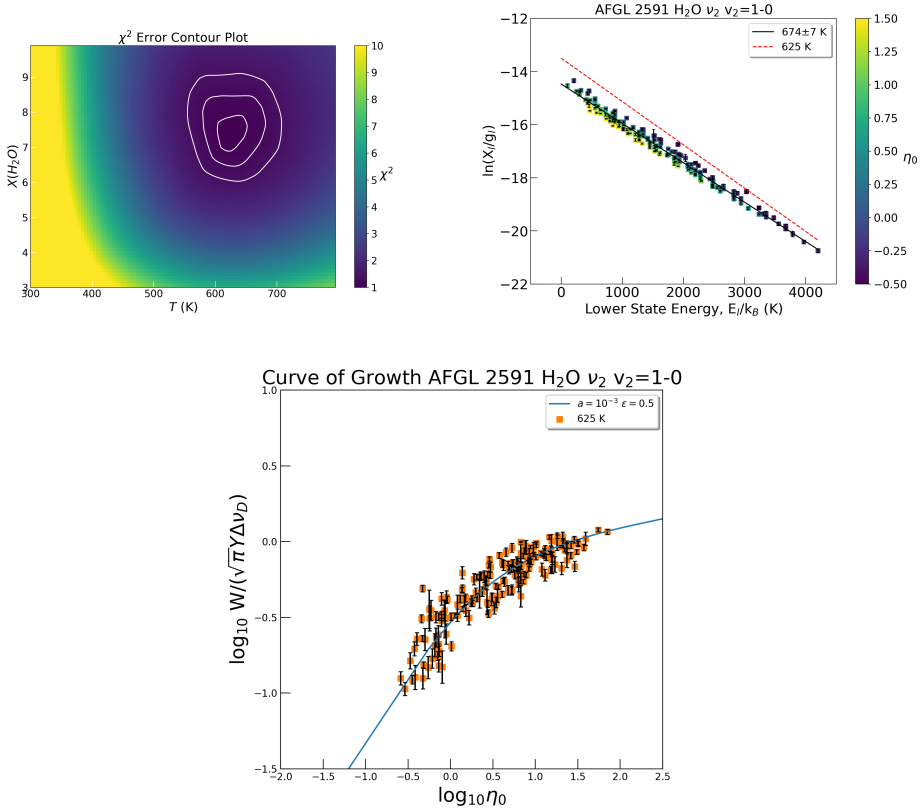

Figure 4.17: *bottom:* The curve of growth for the v=1-0 transition of AFGL 2591. The theoretical curve is for the case of $\epsilon = 0.5$. The empirical curve of growth is calculated based on the physical conditions given in Table 4.2. *top left:* The error on the parameters is given in the contour plot where the colour scale is the reduced χ^2 value. The contours represent the 1σ, 2σ and 3σ uncertainty levels. The H_2O abundance is quoted relative to CO. *top right:* The rotation diagram is a function of η_0 and the abundances for the optically thick lines were determined using the curve of growth. The best fit temperature of 625 K from the curve of growth is represented by the red dashed line. The black solid line is a fit to the corrected data set and the corresponding temperature is indicated. Note that the y-axis is the abundance in the lower level based on the stellar atmosphere theory.

4.5.1 Foreground Absorption

One explanation for the observation of absorption lines towards these massive YSOs is that these lines trace foreground absorption seen against the mid-IR continuum from the disk. This could be the sites of H_2O maser emission in these sources. H_2O masers require temperatures of around 400 K (consistent with that which we find from the curves of growth), densities of 10^8 - 10^9 cm^{-3}, and a high column density of H_2O to be produced (Elitzur et al. 1989).

H_2O masers are detected towards AFGL 2136, with the strongest maser emission coming from 27.1 km s^{-1} (Menten & van der Tak 2004), coinciding with one of

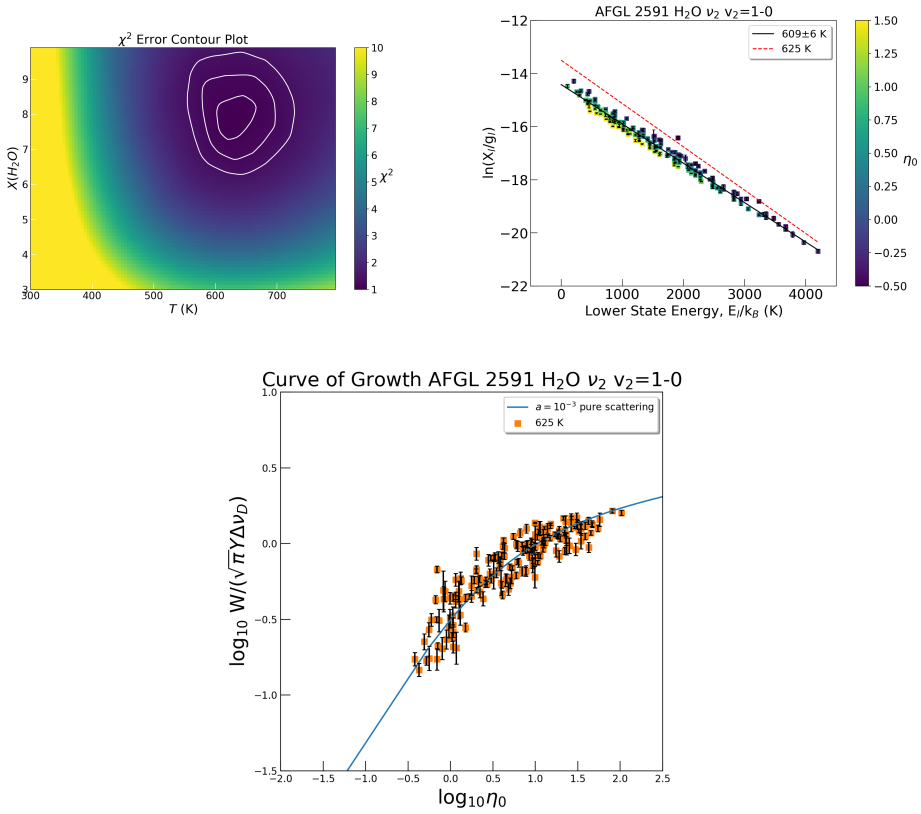

Figure 4.18: *bottom:* The curve of growth for the v=1-0 transition of AFGL 2591. The theoretical curve is for the case of $\epsilon = 0$. The empirical curve of growth is calculated based on the physical conditions given in Table 4.2. *top left:* The error on the parameters is given in the contour plot where the colour scale is the reduced χ^2 value. The contours represent the 1σ, 2σ and 3σ uncertainty levels. The H_2O abundance is quoted relative to CO. *top right:* The rotation diagram is a function of η_0 and the abundances for the optically thick lines were determined using the curve of growth. The best fit temperature of 625 K from the curve of growth is represented by the red dashed line. The black solid line is a fit to the corrected data set and the corresponding temperature is indicated. Note that the y-axis is the abundance in the lower level based on the stellar atmosphere theory.

the mid-IR H_2O velocity components seen in absorption. It should be noted that this value for the v_{lsr} has not changed in around 25 years. The maser emission arises in an area of $0.3\times0.5''$ (600×1000 AU) with centroid velocities ranging from 19-34 km s^{-1}. The authors find that the maser emission is coincident with the radio continuum from RS4 (in their source notation). Considering the uncertainty in the positions, AFGL 2136 IRS1 and RS4 may coincide. The authors propose that the red-shifted velocities of the H_2O maser emission suggests that it is infalling onto the protostar, and may be formed in shocked gas behind the accretion shock. The fact that we observe H_2O absorption, red-shifted with respect to the systemic velocity, would strongly support

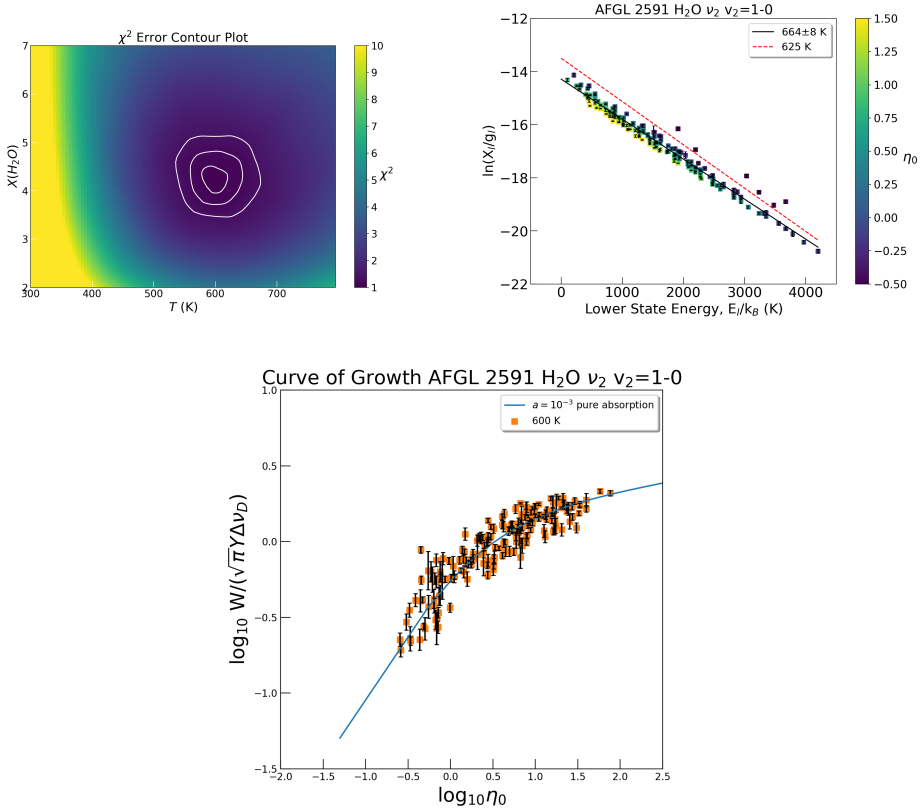

Figure 4.19: *bottom:* The curve of growth for the v=1-0 transition of AFGL 2591. The theoretical curve is for the case of $\epsilon = 1$. The empirical curve of growth is calculated based on the physical conditions given in Table 4.2. *top left:* The error on the parameters is given in the contour plot where the colour scale is the reduced χ^2 value. The contours represent the 1σ, 2σ and 3σ uncertainty levels. The H_2O abundance is quoted relative to CO. *top right:* The rotation diagram is a function of η_0 and the abundances for the optically thick lines were determined using the curve of growth. The best fit temperature of 625 K from the curve of growth is represented by the red dashed line. The black solid line is a fit to the corrected data set and the corresponding temperature is indicated. Note that the y-axis is the abundance in the lower level based on the stellar atmosphere theory.

this scenario, if the absorption came from the location of the masers.

Studies of H_2O maser emission towards AFGL 2591 conclude that it arises from the outflow cavity walls where the outflow interacts with the ambient cloud material (Trinidad et al. 2003; Torrelles et al. 2014). Sanna et al. (2012) find that the maser emission is distributed in a V-shape, opening with position angle consistent with the outflow. The velocity range of the different masers (-31 to -16 km s^{-1}; Torrelles et al. (2014)) coincides with the velocity range of the minor mid-IR H_2O absorption component. Trinidad et al. (2003) also measure 29 H_2O masers in an extended structure, and find values from -28 km s^{-1} to -9.6km s^{-1}, consistent with the range of velocities

of both the major and minor components. Thus the masers velocities also encompass the H_2O absorption line velocities in this source.

A major challenge with a foreground origin for the absorbing gas is the fact that the absorption lines do not go to zero flux, but saturate at 40% and 15% relative to the continuum for AFGL 2136 and AFGL 2591, respectively. If we are seeing the background source through the H_2O-rich walls of an outflow cone, then the absorbing gas must be mixed with IR emitting dust. However from models of interferometry data, the mid-IR continuum comes from ∼100 AU from the star (Monnier et al. 2009; de Wit et al. 2011; Frost et al. 2021). This is on scales sizes similar to the disk, therefore the disk is the natural source of the continuum emission.

Within the scenario of foreground absorption, a more reasonable explanation of why H_2O absorption lines do not reach zero flux is that the absorbing gas does not fully cover the infrared continuum source. This has been pursued before in several absorption line studies (Knez et al. 2009; Barentine & Lacy 2012; Indriolo et al. 2015a; Rangwala et al. 2018). We note that while the strongest maser emission in AFGL 2136 comes from two clusters that are $0.02\times0.01''$ and $0.03\times0.03''$ in size, (corresponding to ∼ 25 and 50 AU respectively, at a distance of 2 kpc) the velocity component seen in absorption at 33 km s^{-1} is not part of the strongest emission, and lies at the extremity of the maser cluster. The extent of the maser clusters is 600×1000 AU, compared to the size of the mid-IR continuum source of ∼125 AU (Monnier et al. 2009; de Wit et al. 2011; Frost et al. 2021). Thus if the H_2O absorption arises from shocked gas coinciding with the H_2O masers, in order to partially cover the source the absorbing gas must reside in blobs coinciding with the masers of corresponding velocity. This would be analogous to the scenario proposed by Knez et al. (2009), where blobs of foreground gas are seen against the circumstellar disk. These blobs would then also have to include the other molecules observed such as HCN, NH_3, CS and C_2H_2. In AFGl 2591, the masers cover a v-shape tracing the cavity walls covering only one side of the continuum, so the absorbing gas could only partially cover the source (Sanna et al. 2012).

4.5.2 Stellar Atmosphere Model

In our previous study on absorption lines of simple organic species in AFGL 2136 and AFGL 2591, we introduced an analysis based on stellar atmosphere theory under the assumption that the absorption lines originate in the disks of these protostars (chapter 3). In order to explain the presence of absorption lines, such a disk must be heated from the mid-plane such that the temperature decreases with increasing scale height. This heating is attributed to viscous accretion in the mid-plane. This same model would also apply to H_2O absorption.

The large spread in the rotation diagrams of Figures 4.4 and 4.14 is an indication that many of the H_2O absorption lines in AFGL 2136 and AFGL 2591 are optically thick. From the curves of growth we see that these lines have transitioned onto the logarithmic part of the curve of growth (Figures 4.8 & 4.17; see below). This is a consequence of the fact that these lines have saturated, resulting in the scatter in the rotation diagram.

A *direct prediction* of the stellar atmosphere model presented in chapter 3 is that

strong absorption lines will saturate at non-zero flux, therefore they may become optically thick whilst at the same time appearing as weak lines. This saturation point will be at the same flux for all lines. This is observed in both AFGL 2136 and AFGL 2591 and demonstrated in Figure 4.6, where absorption lines that trace the same lower level, but with different opacities, are compared to an absorbing slab model that fully covers the infrared source. For the low opacity lines, the absorption lines agree well with this model. However as the opacity increases, the absorption lines diverge more and more from this approximation, as the absorption lines become saturated. As discussed in section 4.5.1, fitting the data with a foreground slab necessitates the inclusion of a coverage factor less than one.

After saturation, the column density of the absorption lines are logarithmically related to the equivalent width. As a result of this, for optically thick lines, the column density will be underestimated. This is visible in Figure 4.5 where the column density of lines with higher opacity, η_0, is more underestimated than those with low opacity.

This scatter has been observed before (Indriolo et al. 2015a, 2020). Indriolo et al. (2020) noted that, in AFGL 2136, the underprediction in the column density was related to the Einstein A coefficient. Transitions with high Einstein A's and/or with large column densities will become optically thick higher up in the disk photosphere compared to optically thin lines. This translates in the rotation diagram into an apparent small column density in that level. We note that the opacity is an interplay of the Einstein A and the column density. Indeed, some lines with very similar η_0's are shifted downward in the rotation diagram by the same amount despite that they have very different Einstein A's.

In chapter 3, we located the absorbing gas to come from a clump at 50 AU, coincident with a peak in the sub-mm continuum of AFGL 2136 imaged with ALMA (Maud et al. 2019). We also adopted the same explanation for AFGL 2591. However as discussed in section 4.2, models of mid-IR interferometry observations require the continuum to originate from around 130 AU, in order to get a reasonable fit. Therefore, if the absorption lines arise in a circumstellar disk, they must probe gas beyond this radius. Such a scenario is outlined in Figure 4.20. On scales of 1000 AU, the dust is too cold to be observed at mid-IR wavelengths therefore mid-IR observations probe only a limited extent of the disk. The large grain disk in the inner 130 AU is also not seen at mid-IR wavelengths as it is optically thin.

In order to achieve a temperature structure in the disk that increases towards the mid-plane, heating of the disk has to be dominated by viscous processes in the mid-plane. Pomohaci et al. (2017) calculate the accretion rate for a sample of YSOs, estimating the accretion luminosity, L_{acc}, from Bracket γ emission, and find a low accretion rate of $1{\times}10^{-5}$ $M_\odot$/yr for AFGL 2136. AFGL 2591 has been modelled by Trinidad et al. (2003) where the authors find that the heating is dominated by stellar radiation from a radius of 20 AU, with models considered with accretion rates below $1{\times}10^{-5}$ $M_\odot/yr$. However the mass estimates for both of these YSOs of 40 $M_\odot$ (Sanna et al. 2012; Maud et al. 2019) would place these stars on the main sequence, as nuclear processes begin in the interior for masses greater than 10 $M_\odot$ during the accretion phase. Therefore their luminosity would come from hydrogen burning in the core, and accretion is not an important source of luminosity. As an aside, this does remove the need to assume a bloated star to account for the high luminosity of these

objects (de Wit et al. 2011; Frost et al. 2021). Tan & McKee (2003) developed an outflow-confined HII region model, in which high accretion rates result in a collimated morphology of the ionising radiation projected out from the star along the outflow direction, shielding the disk from protostellar feedback (Tanaka et al. 2016, 2017). The radiation from the star thus escapes through the polar direction instead of the equatorial. Because of this flashlight effect (Nakano 1989; Yorke & Bodenheimer 1999; Kuiper et al. 2016), radiation pressure does not influence the gas flow in the disk plane and massive stars can keep accreting. However, again, the star derives most of its luminosity from H-burning in the core. As a corollary, the flashlight effect prevents heating of the disk by stellar radiation. Applied to Orion Source *I* in the Orion Molecular Cloud, this model naturally explains the elongation of the radio emission from this source (Tan 2008). This model, if applied to AFGL 2136 and AFGL 2591, would explain the elongated radio emission (Trinidad et al. 2003; Menten & van der Tak 2004), and is outlined in Figure 4.20. Furthermore, it would result in the disk being shielded from stellar radiation and therefore an alternative heating mechanism for the disk is required. We note that, without external radiation heating the disk surfaces, no rim/wall would develop at the inner boundary and the mid-IR radiation would have to come from the disk surface. The scale size of this emitting surface would (still) have to be 50 AU in order to explain the visibility curves in the mid-IR (Preibisch et al. 2003; Monnier et al. 2009; de Wit et al. 2011; Frost et al. 2021).

Consider an internally heated disk. The total luminosity is given by:

$$L_{disk} = 2A < Q_p > \sigma_{sb} T_{eff}^4 \tag{4.9}$$

where A is the surface area, $< Q_p >$ the Planck averaged dust efficiency, σ_{sb} is Stefan-Boltzmann constant, and T_{eff} the effective temperature. $< Q_p >$ can be approximated as:

$$< Q_p >= 2 \times 10^{-3} \frac{a}{1\mu m} \tag{4.10}$$

for 250$<$ T $<$1000 K (cf., Chapter 5 in Tielens 2005). For a disk radius of 125 AU, a size of 50 AU and an effective temperature of 600 K, we get:

$$L_{disk} =< Q_p > 10^5 L_\odot = 10^2 \frac{a}{1\mu m} L_\odot \tag{4.11}$$

For a black body the disk would radiate 10^5 $L_\odot$, which is unrealistic. Hence the dust grains cannot be too large, the absorption/emission is not a black body, and the temperature gradient will steepen (eg., radiation escapes in frequency space rather than diffuses spatially). Taking this luminosity, we can derive the total heating of the disk in the mid-plane, or the viscous dissipation, via:

$$L_{disk} = GM_\star \dot{M}/R \tag{4.12}$$

or

$$\dot{M} = 5 \times 10^{-3} \frac{a}{1\mu m} M_\odot/yr \tag{4.13}$$

for a 40 $M_\odot$ star. The small grains in the inner disk have been removed, likely by a wind. The presence of a wind is proposed by Menten & van der Tak (2004) and Maud et al. (2018) for AFGL 2136 and Trinidad et al. (2003) for AFGL 2591. The dust inside of the rim is composed of much larger grains that have decoupled from the gas and settled in a thin layer in the mid-plane (Maud et al. 2019). Since there is still H_2O gas in the inner disk, the wind would not yet have removed all of the material. We do note that the removal of the small grains greatly reduces the dust-gas coupling to the radiation field and hence this gas has to be viscously heated as well. In the absence of small dust grains, cooling is also greatly reduced and this may lead to the high temperature required to excite the vibrationally excited H_2O line observed by ALMA (Maud et al. 2019). Detailed models will be required to assess these aspects.

Probing the Disk Wind of AFGL 2591

The presence of a velocity shift in the H_2O absorption lines with increasing opacity strongly supports the presence of a wind. Lines with higher opacity are more blue-shifted than those with lower opacities (Fig 4.12). These lines would therefore trace higher layers in a disk atmosphere that are being blown out from the disk by the wind, probing the acceleration zone. Since the orientation of AFGL 2591 is such that the disk is face on, the outflow/wind is directed towards the observer (van der Tak et al. 1999; Sanna et al. 2012), and therefore a larger blue-shift corresponds to the higher layers of the wind. Since the major and minor velocity components are separated by 14±1 km s^{-1} for every line, the velocity variation with opacity must be the same for the two components, and therefore they must both trace the same wind. These components would probe different layers of the disk however, since the peak velocities of the two components are different for the same absorption line. It is unclear however how these two components can have the same acceleration whilst arising in different layers of the disk wind. It is possible that there is a difference in the acceleration of the order of 2 km s^{-1} that cannot be detected due to the blending of the two velocity components. This could explain the scatter in the trend observed between the peak velocity and η_0 (Figure 4.13).

4.5.3 Advantages and Disadvantages

Both the foreground and disk scenarios can provide reasonable fits to the observed behaviour of the equivalent width of the H_2O lines (section 4.5.1 and 4.5.2). However, there are a number of other aspects of the observations that a model has to face. Summarising the observational characteristics of these two sources within the confines of the general structure outlined in Section 4.4, a successful model has to account for:

1) The presence of absorption rather than emission lines.

2) Non-zero saturated lines.

3) Narrow velocity components of ∼10 km s^{-1}, and peak velocities offset from sys-

temic.

4) HCN/C_2H_2 column density differences of a factor of 4 and 10 for AFGL 2136 and AFGL 2591 respectively, between 7 and 13 μm transitions from the same level (chapter 3).

5) Ortho-to-para ratios (OPRs) for C_2H_2 less than the equilibrium value of 3

6) The chemical abundance ratios.

7) The presence of 4-13 μm absorption lines for all molecules and 3 μm emission lines for HCN and C_2H_2.

8) The presence of H_2O absorption lines originating from vibrationally excited levels.

9) The velocity trend in the H_2O transitions with line opacity for AFGL 2591.

In the remainder of this subsection we will examine both scenarios - foreground absorption slab and disk absorption - against these aspects.

Foreground Absorption

As discussed in section 4.5.1, absorption by a foreground slab can readily explain the presence of narrow absorption lines that occur at a velocity offset from the systemic velocity. By associating this foreground slab with the maser emission region(s), the range of velocities observed are described by the known maser velocities.

An externally heated layer of a disk will have a surface layer that is warmer than the interior. Hence, it would show emission lines rather than absorption lines. The foreground layer could eat away this line emission, if the foreground layer and disk are at the same radial velocity. However, as the continuum source has to be only partially covered (section 4.5.1 and below), emission lines would remain and those would actually be more prominent at the longer wavelengths where, in this scenario, the coverage is very small. Hence, within this scenario, we would have to postulate that the gas in the disk surface has a very low abundance of H_2O as well as CO, C_2H_2, HCN, CS, and NH_3. As stellar EUV photons are confined to a very narrow cone, it is unlikely that photo-dissociation of these species by FUV photons plays a role in the disk surface. Moreover, ALMA has revealed the ubiquitous presence of warm H_2O in the inner 125 AU region of AFGL 2136. If this gas can be heated and remain H_2O-rich, then the dust rim or disk should contain H_2O as well.

As introduced in section 4.1, column density variations of HCN and C_2H_2 between bands at different wavelength which trace the same lower level are observed (chapter 3). In order to explain this behaviour in the context of foreground absorption, a partial covering explanation must be invoked that varies with wavelength, and can explain a difference in column density up to a factor of 4 and 10 for AFGL 2136 and AFGL 2591, respectively. This would require that the covering factor, f_c, would have to be 0.1 and 0.015 at 13 μm, for AFGL 2136 and AFGL 2591, respectively. This

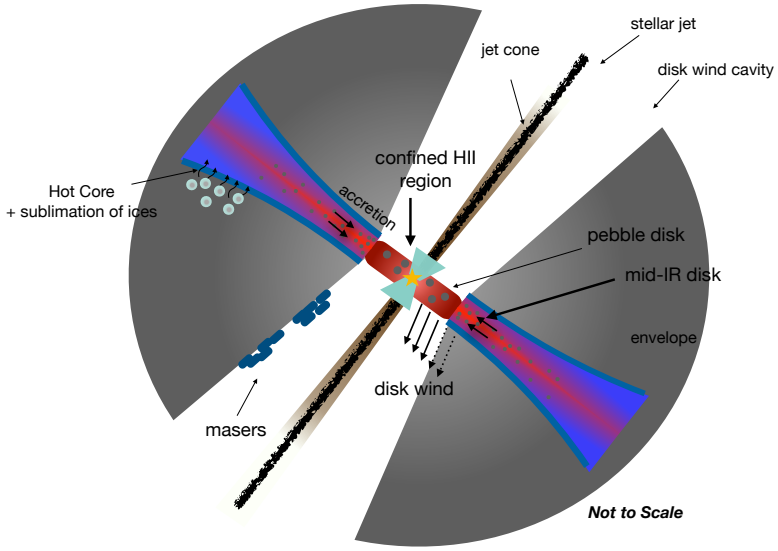

Figure 4.20: Cartoon illustration of the different physical components of the proposed disk and its surroundings (not to scale), and the mechanisms relevant to the discussion, based on observational evidence for AFGL 2136. A jet has carved a narrow channel (shown in brown) through the thick cocoon around the massive protostar. The radiation from the central star escapes through this channel, creating a flashlight effect. Near the star, the gas in the channel walls is ionised by the stellar radiation, producing a confined HII region, indicated by the transparent region. A disk wind, represented by the solid lines, has removed gas and small dust grains within 125 AU but leaving a thin pebble disk. The thin inner pebble disk is the source of the continuum and the vibrationally excited H_2O lines in the sub-mm while the continuum and absorption lines in the mid-IR originate from the dust disk beyond 125 AU. The disk is heated internally through viscous processes, leading to accretion. We see evidence for the wind from the mid-IR absorption lines in AFGL 2591, represented by the dotted lines. Outside of 125 AU, the disk wind is not strong enough to excavate gas and (small) grains. On a scale of 1000 AU, the disk is not warm enough to observe at mid-IR wavelengths, therefore the mid-IR disk is only observed out to a limited portion of the whole disk. At around 1000 AU, the gas is warmer than ∼100 K and ices evaporate, leading to the release of complex organic molecules (COMs) from grain surfaces as well as the gas-phase production of COMs. This is the Hot Core region. We note that there is a lack of COMs detected in a disk-like structure in AFGL 2136, but rather CH_3OH is observed in a plume structure, suggesting that this object is late on it's evolution, consistent with detection of unresolved H30α emission in a very compact region (Maud et al. 2018). AFGL 2591 on the other hand does show CH_3OH on scales of 1000 AU in a disk-like structure (Jiménez-Serra et al. 2012). The location of maser emission is located, tracing the cavity walls. The temperature and density of the disk increase towards both the mid-plane and the central star, with the colour scale representing the temperature where red is hot and blue cold. The grey-scale colour represents the surrounding envelope in which the disk is embedded. For AFGL 2591 the observer looks into the cone of the blue-shifted outflow, whereas for AFGL 2136 the observer looks more into the plane of the disk (inclination of 40°).

is, however, difficult to reconcile with a dust rim origin for the mid-IR continuum, as the whole wall would be at a very similar temperature and would not vary with wavelength. Hence, this implies that the mid-IR continuum comes from a spatially

extended disk surface, where radial distance differences will result in spatial variations in the dust temperature.

In Chapter 5 we show that HCN and C_2H_2 in AFGL 2136 are in absorption at 3 μm. Curves of growth for a foreground absorbing slab show that lines are on the linear part of the curve of growth and optically thin at all wavelengths. Thus in order to explain the observed equivalent widths, the lines at 13 μm require a partial covering factor of 0.3 and 0.25 for HCN and C_2H_2 respectively. This compares to covering factors of > 0.9 and < 0.95 for HCN and C_2H_2 respectively at both 3 μm and 7 μm, which have approximately equivalent covering factors. Thus the area of the 13 μm continuum must be three times smaller than the area of both the 3 μm and 7 μm continuum. This constraint on the covering factor of HCN and C_2H_2 means that, in the case that these species are produced in a foreground cloud, these molecules must cover the source more than H_2O, which has a covering factor of 0.4 at 6 μm. The ubiquity and high column density of H_2O in star forming regions makes this scenario highly unlikely as H_2O is very easily formed above temperatures of $\sim$250 K (Walsh et al. 2015; Agúndez et al. 2018). An OPR for C_2H_2 of 1.6 is derived, taking into consideration the partial covering factors in the curve of growth analysis.

Furthermore, the 4 to 13 μm spectral region of both sources exclusively shows lines in absorption, however the 3 μm spectrum of AFGL 2591 shows HCN and C_2H_2 lines in emission (chapter 3). AFGL 2591 is not unique in this regard with emission lines of HCN detected towards MonR2 IRS 3 at 3 μm (chapter 5). This massive YSO is another well known target that exhibits absorption lines at mid-IR wavelengths (Boonman et al. 2003a; Dungee et al. 2018). While a varying partial coverage fraction with wavelength is perhaps conceivable, that this slab would then emit in the 3 μm lines seems very unlikely.

The observations reveal absorption lines associated with v=2-1 transitions. The derived vibrational excitation temperatures of both sources are very similar to the rotational excitation temperature. This would imply densities in excess of the critical density for vibrational transitions ($\sim 10^{10}$ cm^{-3}). This is a much higher density than allowed in masers; eg., maser action requires densities below the critical density of rotational transitions and models typically yield densities of 10^9 cm^{-3} (Hollenbach et al. 2013; Neufeld & Melnick 1991). Of course, masers also require specific sight lines of high velocity coherence and so in principle the conditions in the maser spots might be different than the general region probed in absorption.

Shock heating, such as that which excites masers, cannot sustain a high enough temperature for long enough to form many of the simple organic species that are also observed in absorption (chapter 3). These include HCN, C_2H_2, NH_3 and CS, with CH_4 also being observed towards another high mass source, NGC 7538 IRS1 (Knez et al. 2009). These molecules are characteristic of disk chemistry (Walsh et al. 2015; Agúndez et al. 2018; Banzatti et al. 2017) (see Section 4.5.4). Also, by the time H_2O would form in the post-shock gas, it would have reached an equilibrium velocity and could not explain the peak velocity trend observed in AFGL 2591.

The observed OPRs of C_2H_2 are 1.8 ± 0.2 and 2.1 ± 0.3 for AFGL 2136 and AFGL 2591, respectively (chapter 3). If C_2H_2 is formed in hot gas, it should have the equilibrium OPR of 3, as opposed to cold formation on grain surfaces where the OPR is less than 3. A lower than 3 OPR, such as has been observed for C_2H_2 in Orion IRc2

(Rangwala et al. 2018), has previously been explained as gas that has been released from grain surfaces by shocks, and not had enough time to convert p-C_2H_2 to o-C_2H_2 (Timmermann 1998; Neufeld et al. 2019). This can only occur for low velocity C-type shocks with velocities ≤ 15 km s^{-1} however, since for higher velocities, large amounts of H^+ and H_3^+ rapidly convert p-C_2H_2 to o-C_2H_2, quickly achieving an OPR of 3. A shock velocity of ≤ 15 km s^{-1} is inconsistent with the J shock velocities proposed by Menten & van der Tak (2004) to explain the maser emission, therefore shocks are not a viable explanation of the low OPRs of C_2H_2.

Circumstellar Disk

Absorption lines are a natural outcome of radiative transfer in a disk atmosphere with a temperature decreasing with height. With disk densities close to or above the critical density of the levels involved, radiative transfer in the lines is dominated by absorption rather than scattering and this will lead in a natural way to saturated lines that do not go to zero. The observed velocity gradient with increasing η_0 of the H_2O lines in AFGL 2591 also fits naturally in the environment where an inner disk has been removed by a disk wind. The presence of absorption lines from vibrationally excited levels with a similar excitation temperature as the rotational population is also expected in a disk the level populations are in LTE at high densities (chapter 3).

Turning now to the challenges to the model, the difference in absorption column density between 7 and 13 μm lines of HCN and C_2H_2 originating from the same level can conceivably be explained by locating these species in a region of the disk that has the "right" conditions (i.e., temperature) to drive the chemistry to high abundances of these species (chapter 3). Indeed, the enhanced abundances of HCN and C_2H_2 are common for the inner regions of disks (Walsh et al. 2015; Agúndez et al. 2018). Therefore the abundance of HCN and C_2H_2 would be lower in the outer parts of the disk, leading to a high abundance region concentrated in the inner parts of the disk. At the longer wavelengths of 13 μm, the molecular absorption is diluted by dust emission from larger radii, where molecule formation is less efficient due to the lower temperatures, leading to the apparent column density discrepancy.

Such a thermally and chemically stratified disk may also be able to explain the presence (and characteristics) of the HCN and C_2H_2 emission lines observed in the 3 μm region of AFGL 2591. The emitting gas is cool ($\sim$200 K) and the lines are narrow. The absence of absorption lines at 3 μm implies the absence of HCN and C_2H_2 in the innermost regions of the disk where these molecules are destroyed, therefore we attributed emission lines to be produced by scattering of continuum photons higher up in the disk photosphere, thus explaining the lower temperature and narrower line width. At the longer wavelengths of 7 μm, cooler dust emission traces larger disk radii where an efficient gas phase chemistry takes place at temperatures of $\sim$600 K, which we see in absorption.

In chapter 3 we found that the low OPR of C_2H_2 could reasonably be explained by a disk atmosphere. Due to the fact that ortho lines will have three times larger column density than the para lines, these lines will become optically thick higher up in the disk photosphere compared to the para lines, thus probing a smaller column density and resulting in a slightly lower OPR than three.

The line profiles of the absorption lines present a challenge to this model however. The absorption lines of AFGL 2136 are offset from the H_2O emission line detected with ALMA, where the 232 GHz $\nu_2 = 1$ line is centred around the systemic velocity of 22 km s^{-1}. They are also around a factor of two narrower. Therefore, if the absorption lines originate in the mid-IR disk, they must only trace the red-shifted part of this disk. For AFGL 2591, the absorption lines are blue-shifted with respect to the systemic velocity. In this case they would have to probe only the blue side of the disk. This requires a specific geometry; for example a flaring disk where the completely opaque outer parts partially obscure the inner region at mid-IR wavelengths. The outer parts need to be transparent at sub-mm wavelengths, however.

In the stellar atmosphere analysis, we adopted a Doppler width based on the observed width of the optically thin lines. In this model, however, the relevant line broadening processes are thermal and microturbulent broadening. Therefore if macroscopic motions dominated the line profile, simply taking the observed line width might overestimate the Doppler width. We note that macroscopic motions such as rotation merely smear out the line profile but do not affect the equivalent width analysis (Mihalas 1978). At the temperatures we derive, the thermal contribution to the line width is around 1 km s^{-1}. Fits to the curve of growth are not possible with an intrinsic line width of < 2 km s^{-1} for any of the curves of growth, except for $\epsilon = 0$ for AFGL 2591. Therefore, microscopic turbulent processes would have to dominate the intrinsic line width, in such a way as to be greater than the sound speed (around 2 km s^{-1}). We note that dissipation of this supersonic turbulence may be a source of internal energy for the gas. As turbulence might be dissipated on a sound crossing timescale (300 yr at 100 AU), this may require a continuous replenishment of turbulence from, e.g., gravitational or magnetic energies.

The Implications for Chemistry in Disks

A CO abundance of 10^{-4} implies a dust continuum absorption of 7.7×10^{-24} and 4.3×10^{-23} cm^{-2}/g-of-gas, for AFGL 2136 and AFGL 2591, respectively. This is calculated as X_{CO}/α from equation 4.8. This is about a factor 2-10 less than in the models of Ormel et al. (2011). Overall, it seems that coagulation has proceeded to a greater extent in these disks than in the models developed by them for dense cores in molecular clouds.

The high derived abundance ratio of H_2O relative to CO implies that most of the elemental oxygen has been converted into H_2O. The dust in the region responsible for the continuum has to be warmer than 450 to 600 K and is therefore well above the ice sublimation temperature. As a result all the available oxygen will be in the gas phase. At the derived gas temperature, atomic oxygen is quickly converted into water through reactions with H_2 (Walsh et al. 2015; Agúndez et al. 2018). In our analysis, we have given abundances relative to CO, considering it likely that in the warm gas much of the available carbon has been converted into CO, resulting in an abundance of $\sim10^{-4}$ with respect to H-nuclei.

For AFGL 2591, we derive a very high H_2O/CO ratio of $7.4^{+0.5}_{-0.4}$, while typically this value is at most 2. The H_2O abundance with respect to H is also very high, ranging from 7.9×10^{-4} to 4.2×10^{-4}, as we calculate abundances under the condition

that CO to H is 1×10^{-4}. Therefore, the dust opacity implied (quoted above) is likely overestimated by around a factor of 2 or 3. This would also result in a lower CO abundance however, therefore the H_2O/CO ratio would stay the same. Whether this high abundance is due to the chemistry or an observational effect is unclear. H_2O and CO are observed at 6 and 4 μm, respectively. Since different wavelengths probe different spatial scales in the disk, spatial variations of the column densities of these molecules could lead to a difference in the abundance ratios. This would have to explain at least a factor of 2 difference, taking the H_2O abundance derived assuming $\epsilon = 1$ and taking the highest typical H_2O/CO ratio of 2. The ^{12}CO abundance of AFGL 2591 is estimated from the equivalent widths of ^{13}CO and assuming a $^{12}C/^{13}C$ ratio of 60. If this isotopologue ratio was larger than 60, this would also reduce the H_2O/CO ratio. If the ^{12}CO abundance was increased, then all the abundances quoted in Table 4.3 for AFGL 2591 would be reduced by the same factor. Alternatively CO could be depleted in this source. In AFGL 2136, the H_2O/CO abundance is within the range that would be expected for a high temperature gas-phase chemistry where a lot of water is produced. Therefore the relative abundances of the other species in AFGL 2136 are robust.

Table 4.3: Chemical Abundance Ratios.

	HCN/CO ($\times10^{-2}$)	C_2H_2/CO ($\times10^{-2}$)	NH_3/CO ($\times10^{-2}$)	HCN/C_2H_2	CS/CO ($\times10^{-3}$)	H_2O/CO
AFGL 2591	10.0	$> 0.9^a$	2.0	$< 11.2^a$	7.5	7.4^e
AFGL 2136	2.0	1.0	0.2	1.8	1.3	1.6^e
Hot Core[b]	0.03	0.02	0.02	1.5	0.1	1.7
TTauri Disk[c]	1-2	0.8-1	< 6	1-1.2	–	0.2-0.3
Herbig Disk[d]	15.0	5.0	–	3.0	3.8	1.0

[a] Upper limits are place on C_2H_2 because, while this species was detected at 13 μm in AFGL 2591, the undiluted band at 7 μm was not detected.
[b] Orion-KL observed at mm-wavelengths (Feng et al. 2015)
[c] Observations of TTauri disks by Mandell et al. (2012)
[d] Disk chemical models by Agúndez et al. (2018) assuming a H_2O/CO ratio of 1.
[e] Taking the H_2O abundance from Table 4.2.

Hot core abundance ratios of several species relevant to this discussion are summarised in Table 4.3. The abundances we derive for AFGL 2591 and AFGL 2136 are 1-2 orders of magnitude higher than what is observed in hot cores. Abundance ratios for TTauri disks calculated by Mandell et al. (2012) are consistent with other estimates of these ratios derived from disks in low mass YSOs observed with Spitzer (Salyk et al. 2011; Pontoppidan et al. 2014). These are in agreement with the abundance ratios that we derive in AFGL 2591 and AFGL 2136 (Table 4.3), as are the

abundance ratios for chemical models of Herbig disks. We caution however that the heating of Herbig and TTauri disks is by stellar radiation, therefore involves UV processing which may limit the applicability of this chemistry for the massive YSOs.

Summary

Most of the characteristics of the observed absorption lines in the mid-IR can be readily fit into the disk scenario. The most challenging aspect is the presence of narrow absorption lines shifted from the systemic velocity. This would require a specific geometry for the disk and models will have to show whether these are tenable. In contrast, absorption in foreground gas faces many challenges that are difficult to accommodate. With these considerations, we conclude that the disk origin for the absorption lines more robustly explains all of the available observational results from the spectral survey, taking into account not only absorption of H_2O, but also the other simple organics across all wavelengths. Detailed physical and chemical models for disks around massive protostars are required to fully test the disk scenario.

4.6 Conclusions

We have analysed the spectral features of H_2O in the 5-8 μm SOFIA/EXES spectral survey of the massive protostars AFGL 2136 and AFGL 2591 at a resolving power of R=50,000 (6 km s^{-1}). Our conclusions are as follows:

- Hundreds of rotational transitions of H_2O are detected in the ground and first vibrational states, as well as several lines of $H_2^{18}O$. All transitions are observed in absorption.

- Two main origins for the H_2O lines are investigated: foreground absorption against the mid-IR continuum source and an origin in the photosphere of an internally heated circumstellar disk. Using curve of growth analyses, H_2O temperatures of 457^{+13}_{-14} K and 470^{+24}_{-33} K are derived for the foreground and disk models respectively for AFGL 2136, and 541^{+1}_{-8} K and 625^{+27}_{-22} K respectively for AFGL 2591.

- We find that some lines are optically thick, even though they saturate at 40% and 15% of the continuum for AFGL 2136 and AFGL 2591, respectively, resulting in a large scatter in the rotation diagram.

- We find that, for a foreground origin for the absorption lines, the line profiles agree with H_2O maser emission in each source. However, to explain the saturation of the lines at non-zero flux, a partial covering factor must be invoked in this case. Such a covering factor must vary with wavelength by up to a factor of 10 in order to account for column density variations observed in HCN and C_2H_2 at 7 and 13 μm. Furthermore H_2O must cover the source less than HCN and C_2H_2 (chapter 5). The observed chemical abundances of HCN, C_2H_2, NH_3 and CS provide a further challenge to this interpretation. Finally, ALMA has

revealed the presence of large grains and vibrationally excited water gas in Keplerian rotation in the inner 130 AU of AFGL 2136, therefore H_2O emission lines would be expected which are not observed.

- A disk photosphere origin of the absorption lines explains in a natural way the presence of absorption lines that saturate at non zero flux. A disk origin can also account for the column density variations of HCN and C_2H_2, and low OPRs of C_2H_2, and chemical abundance ratios are characteristic of disk chemistry. However, the presence of absorption lines requires a decreasing temperature gradient with height in the disk, implying that heating of the disk is dominated by viscous dissipation in the mid-plane rather than by external illumination from the central protostar. The absence of external illumination on the disk is consistent with the flashlight effect created by the outflow cavity and the observed thermal radio morphology. Absorption lines in AFGL 2591 show velocity trends with opacity hinting at the presence of a disk wind. Finally, the peak velocities of the absorption lines are offset from the systemic velocity of the sources, and the line widths are narrower than would be expected from a disk origin, requiring a specific geometry.

- We conclude that a disk origin for the absorption lines best explains all of the available observational results from the spectral survey from water and simple organics across all wavelengths.

Acknowledgements

Based [in part] on observations made with the NASA/DLR Stratospheric Observatory for Infrared Astronomy (SOFIA). SOFIA is jointly operated by the Universities Space Research Association, Inc. (USRA), under NASA contract NNA17BF53C, and the Deutsches SOFIA Institut (DSI) under DLR contract 50 OK 0901 to the University of Stuttgart. The authors thank the anonymous referee for their very helpful and constructive input. A.G.G.M.T thanks the Spinoza premie of the NWO.

4.A Appendix

Table 4.4: Line Parameters for the v=1-0 transition of AFGL 2136. E_l is the energy of the lower level of the transition, g_l and g_u are the statistical weights of the lower and upper levels respectively, A_{ul} is the Einstein A coefficient of the transition, v_{lsr} is the peak velocity of the line, FWHM is the full width at half maximum of the line, W is the equivalent width in units of Hz and τ_p is the peak optical depth of the transition. η_0 is the opacity in the lower level of the transition calculated for $\epsilon = 0.5$. Line data were taken from the HITRAN database (Gordon et al. 2017).

Transition	λ (μm)	E_l (K)	g_l	g_u	A_{ul} (s^{-1})	v_{lsr} (km s^{-1})	FWHM (km s^{-1})	W (10^8 Hz)	$\log_{10}(\eta_0)$	$\log_{10}(\tau_p)$
$12_{2,11} - 11_{1,10}$	5.3719	2194	69	75	10.9	24.1 ± 1.8	11.2 ± 1.2	4.83 ± 0.80	0.57	0.12
$12_{1,11} - 11_{2,10}$	5.3737	2194	23	25	10.9	26.1 ± 0.7	7.9 ± 0.7	2.29 ± 0.66	0.09	-0.36
$11_{3,8} - 10_{4,7}$	5.3772	2275	63	69	3.3	26.0 ± 2.1	7.5 ± 0.9	1.64 ± 0.84	-0.06	-0.51
$9_{3,7} - 8_{2,6}$	5.3806	1414	17	19	5.0	27.2 ± 0.6	12.0 ± 0.5	4.80 ± 0.24	0.36	-0.07
$8_{3,6} - 7_{2,5}$	5.4119	1125	45	51	4.3	25.2 ± 0.6	9.6 ± 0.3	5.36 ± 0.35	1.00	0.58
$7_{6,1} - 7_{5,2}$	5.4183	1525	45	45	1.3	25.7 ± 1.8	7.9 ± 0.8	1.83 ± 0.74	0.04	-0.39
$9_{3,6} - 9_{5,4}$	5.4238	2125	57	57	1.9	26.4 ± 1.9	10.4 ± 1.1	1.82 ± 0.43	-0.23	-0.68
$11_{2,10} - 10_{1,9}$	5.4248	1860	21	23	10.2	26.7 ± 1.6	13.7 ± 0.6	5.53 ± 1.06	0.35	-0.09
$7_{3,5} - 6_{2,4}$	5.4431	867	13	15	3.9	25.6 ± 1.4	8.8 ± 0.7	3.97 ± 0.80	0.66	0.26
$10_{1,9} - 9_{2,8}$	5.4862	1554	19	21	9.5	26.7 ± 0.8	10.0 ± 0.5	4.63 ± 0.42	0.58	0.15
$10_{3,7} - 9_{4,6}$	5.4904	1929	19	21	2.6	24.9 ± 0.9	10.6 ± 0.5	1.51 ± 0.31	-0.33	-0.78
$11_{4,7} - 10_{5,6}$	5.5031	2473	63	69	1.7	25.4 ± 1.1	8.0 ± 0.6	1.14 ± 0.17	-0.49	-0.95
$9_{2,7} - 8_{3,6}$	5.5179	1447	51	57	4.6	24.3 ± 1.4	10.5 ± 0.7	5.24 ± 0.84	0.80	0.37
$11_{1,10} - 11_{0,11}$	5.5290	1909	69	69	0.8	25.2 ± 0.9	8.1 ± 0.6	1.60 ± 0.20	-0.30	-0.74
$12_{4,9} - 12_{3,10}$	5.5298	2824	75	75	2.2	24.0 ± 0.6	7.2 ± 1.0	1.12 ± 0.59	-0.67	-1.14
$10_{5,6} - 10_{4,7}$	5.5496	2275	63	63	2.7	25.2 ± 0.3	10.8 ± 0.8	1.94 ± 0.18	-0.14	-0.59
$8_{5,4} - 8_{4,5}$	5.5651	1615	51	51	2.5	25.5 ± 1.1	8.4 ± 0.6	2.65 ± 0.46	0.34	-0.09
$7_{5,3} - 7_{4,4}$	5.5670	1335	15	15	2.2	26.0 ± 0.2	9.2 ± 0.6	1.82 ± 0.15	0.02	-0.41
$5_{5,0} - 5_{4,1}$	5.5685	878	33	33	1.1	24.1 ± 1.2	8.9 ± 0.6	3.39 ± 0.57	0.49	0.08
$7_{5,2} - 7_{4,3}$	5.5775	1340	45	45	2.2	25.0 ± 0.6	9.9 ± 0.4	3.35 ± 0.24	0.50	0.07
$8_{2,7} - 7_{1,6}$	5.5836	1013	45	51	7.9	24.4 ± 2.0	12.3 ± 0.8	10.38 ± 0.71	1.40	0.99
$10_{2,9} - 10_{1,10}$	5.5870	1603	63	63	1.0	25.3 ± 2.3	8.5 ± 1.1	1.94 ± 0.82	0.03	-0.40
$8_{5,3} - 8_{4,4}$	5.5917	1628	17	17	2.6	26.2 ± 0.2	9.4 ± 0.5	1.63 ± 0.11	-0.12	-0.55

Table 4.4: continued.

Transition	λ (μm)	E_l (K)	g_l	g_u	A_{ul} (s^{-1})	v_{lsr} (km s^{-1})	FWHM (km s^{-1})	W (10^8 Hz)	$\log_{10}(\eta_0)$	$\log_{10}(\tau_p)$
$9_{3,6} - 8_{4,5}$	5.6118	1615	51	57	2.0	26.0 ± 1.4	10.2 ± 0.8	2.94 ± 1.51	0.31	-0.12
$10_{4,7} - 10_{3,8}$	5.6230	2081	63	63	2.8	25.5 ± 0.8	7.6 ± 0.4	1.65 ± 0.21	0.07	-0.38
$9_{2,8} - 9_{1,9}$	5.6485	1324	19	19	1.2	26.5 ± 0.2	10.3 ± 0.6	1.71 ± 0.13	-0.13	-0.56
$9_{1,9} - 8_{0,8}$	5.6551	1070	17	19	13.2	24.0 ± 1.8	12.3 ± 0.8	7.02 ± 2.01	1.16	0.75
$9_{4,6} - 9_{3,7}$	5.6590	1750	19	19	3.0	25.0 ± 0.8	8.8 ± 0.5	1.37 ± 0.62	-0.10	-0.54
$10_{2,8} - 10_{1,9}$	5.6645	1860	21	21	2.1	26.1 ± 0.2	8.3 ± 0.6	1.17 ± 0.11	-0.32	-0.76
$8_{4,5} - 8_{3,6}$	5.6864	1447	51	51	3.1	24.9 ± 0.7	11.3 ± 0.4	5.45 ± 0.34	0.63	0.20
$7_{4,4} - 7_{3,5}$	5.7051	1175	15	15	3.1	24.9 ± 1.1	8.7 ± 0.7	2.84 ± 0.38	0.35	-0.07
$11_{3,8} - 11_{2,9}$	5.7131	2432	69	69	3.2	28.7 ± 0.2	10.7 ± 0.5	1.95 ± 0.11	-0.14	-0.60
$6_{4,3} - 6_{3,4}$	5.7162	933	39	39	2.9	24.5 ± 4.0	10.2 ± 0.6	4.68 ± 0.71	0.96	0.55
$5_{4,2} - 5_{5,3}$	5.7217	725	11	11	2.4	24.6 ± 1.1	10.1 ± 0.4	4.61 ± 0.79	0.53	0.12
$10_{4,7} - 9_{5,4}$	5.7233	2125	57	63	1.2	26.0 ± 0.2	8.2 ± 0.4	1.03 ± 0.07	-0.33	-0.78
$8_{1,7} - 8_{0,8}$	5.7264	1070	17	17	1.4	24.1 ± 1.0	9.6 ± 0.7	2.53 ± 0.27	0.16	-0.25
$4_{4,0} - 4_{3,1}$	5.7281	552	9	9	1.6	24.5 ± 0.9	9.5 ± 0.6	2.67 ± 1.30	0.43	0.03
$8_{3,6} - 8_{2,7}$	5.7320	1274	51	51	2.7	25.2 ± 2.0	10.8 ± 0.9	6.04 ± 1.39	0.73	0.31
$9_{2,7} - 9_{1,8}$	5.7494	1552	57	57	2.6	24.6 ± 1.6	9.9 ± 0.8	3.11 ± 0.70	0.51	0.08
$6_{4,2} - 6_{3,3}$	5.7550	951	13	13	3.2	24.7 ± 1.5	10.1 ± 0.8	4.13 ± 0.70	0.51	0.10
$7_{2,6} - 7_{1,7}$	5.7735	843	15	15	1.7	25.6 ± 0.7	11.5 ± 0.4	4.99 ± 0.30	0.41	-0.01
$7_{3,5} - 7_{2,6}$	5.7792	1021	15	15	3.1	24.9 ± 1.7	11.4 ± 1.0	5.00 ± 0.73	0.50	0.09
$10_{3,7} - 10_{2,8}$	5.7995	2069	21	21	4.1	27.5 ± 0.3	8.7 ± 0.8	1.46 ± 0.17	-0.19	-0.64
$7_{1,6} - 7_{0,7}$	5.8022	843	45	45	1.8	25.0 ± 1.2	12.4 ± 0.7	7.38 ± 0.66	0.91	0.50
$11_{4,7} - 11_{3,8}$	5.8050	2609	69	69	5.3	24.7 ± 0.7	9.2 ± 0.5	2.23 ± 0.19	-0.06	-0.52
$8_{4,4} - 8_{3,5}$	5.8088	1511	17	17	4.5	26.0 ± 0.9	11.3 ± 0.5	3.65 ± 0.77	0.28	-0.15
$9_{4,5} - 9_{3,6}$	5.8280	1846	57	57	5.2	25.6 ± 0.8	8.2 ± 0.9	2.08 ± 1.40	0.56	0.12
$10_{4,6} - 10_{3,7}$	5.8289	2213	21	21	5.6	27.6 ± 0.3	8.4 ± 0.9	1.03 ± 0.14	-0.18	-0.64
$6_{2,5} - 6_{1,6}$	5.8342	643	39	39	2.1	24.0 ± 1.8	10.9 ± 0.7	7.07 ± 1.85	1.11	0.71

Table 4.4: continued.

Transition	λ (μm)	E_l (K)	g_l	g_u	A_{ul} (s^{-1})	v_{lsr} (km s^{-1})	FWHM (km s^{-1})	W (10^8 Hz)	$\log_{10}(\eta_0)$	$\log_{10}(\tau_p)$
$8_{2,6} - 8_{1,7}$	5.8380	1270	17	17	3.3	25.1 ± 1.0	9.9 ± 0.6	3.87 ± 0.38	0.37	-0.05
$6_{2,4} - 5_{3,3}$	5.8575	725	11	13	1.8	24.2 ± 0.8	9.4 ± 0.6	3.75 ± 0.33	0.50	0.10
$8_{4,5} - 7_{5,2}$	5.8656	1525	45	51	0.9	25.9 ± 1.1	9.8 ± 0.7	2.21 ± 0.96	0.03	-0.40
$9_{3,6} - 9_{2,7}$	5.8729	1729	57	57	5.2	25.0 ± 1.3	10.3 ± 0.6	4.82 ± 0.66	0.67	0.24
$8_{3,6} - 7_{4,3}$	5.8860	1340	45	51	1.0	24.9 ± 1.2	8.8 ± 0.5	2.52 ± 0.72	0.28	-0.14
$5_{2,4} - 5_{1,5}$	5.8909	470	11	11	2.5	25.6 ± 1.8	13.1 ± 0.7	7.47 ± 1.87	0.82	0.42
$7_{2,5} - 7_{1,6}$	5.9228	1013	45	45	4.4	24.5 ± 2.0	10.4 ± 0.8	5.75 ± 1.73	1.17	0.76
$8_{3,5} - 8_{2,6}$	5.9246	1414	17	17	6.1	24.5 ± 1.8	9.0 ± 0.9	3.33 ± 0.99	0.53	0.10
$7_{4,3} - 6_{5,2}$	5.9399	1278	39	45	0.6	25.1 ± 1.4	8.8 ± 0.7	2.13 ± 0.42	0.05	-0.37
$7_{3,5} - 6_{4,2}$	5.9447	1090	13	15	0.9	25.8 ± 3.0	12.5 ± 1.5	2.17 ± 0.59	-0.04	-0.46
$7_{3,4} - 7_{2,5}$	5.9507	1125	45	45	6.5	24.5 ± 1.5	9.7 ± 0.6	5.90 ± 1.79	1.25	0.83
$6_{3,3} - 6_{2,4}$	5.9530	867	13	13	6.0	24.5 ± 2.0	10.1 ± 0.8	4.28 ± 2.45	0.91	0.50
$6_{3,3} - 5_{4,2}$	5.9792	878	11	13	0.8	25.7 ± 1.1	10.0 ± 0.6	1.87 ± 0.49	0.01	-0.41
$6_{3,4} - 5_{4,1}$	6.0191	878	33	39	0.7	24.0 ± 0.5	7.1 ± 0.2	2.96 ± 0.22	0.46	0.05
$7_{2,6} - 6_{3,3}$	6.0350	951	13	15	0.6	25.2 ± 0.3	10.0 ± 0.8	1.59 ± 0.17	-0.09	-0.50
$6_{4,3} - 5_{5,0}$	6.0375	1067	33	39	0.3	25.2 ± 2.6	14.0 ± 1.4	1.94 ± 0.43	-0.14	-0.55
$5_{3,2} - 4_{4,1}$	6.0887	702	27	33	0.4	25.7 ± 1.2	12.0 ± 0.6	3.56 ± 0.76	0.27	-0.14
$5_{2,4} - 4_{3,1}$	6.0964	552	9	11	0.7	24.4 ± 0.7	9.3 ± 0.4	2.63 ± 0.22	0.25	-0.15
$4_{2,2} - 3_{3,1}$	6.1062	410	7	9	0.5	24.1 ± 0.6	8.9 ± 0.4	2.42 ± 0.16	0.16	-0.24
$4_{2,3} - 3_{3,0}$	6.1630	410	21	27	0.4	24.7 ± 0.8	10.1 ± 0.5	4.50 ± 0.35	0.57	0.18
$4_{4,1} - 5_{3,2}$	6.1698	732	33	27	0.2	24.0 ± 0.3	8.9 ± 0.5	1.37 ± 0.12	-0.12	-0.52
$3_{3,0} - 4_{2,3}$	6.2218	432	27	21	0.3	24.6 ± 1.2	10.6 ± 0.7	3.35 ± 0.38	0.28	-0.11
$3_{1,3} - 2_{2,0}$	6.2371	195	5	7	0.4	24.0 ± 3.4	12.5 ± 1.4	3.64 ± 0.55	0.18	-0.21
$5_{4,1} - 6_{3,4}$	6.2388	933	39	33	0.3	27.2 ± 0.2	9.8 ± 0.5	2.09 ± 0.13	0.08	-0.33
$2_{2,0} - 3_{1,3}$	6.2453	204	7	6	0.4	24.0 ± 1.1	7.7 ± 0.6	1.45 ± 0.34	-0.02	-0.41
$3_{2,1} - 4_{1,4}$	6.2716	323	27	21	0.3	24.0 ± 1.8	9.6 ± 0.8	2.83 ± 1.13	0.45	0.06

Table 4.4: continued.

Transition	λ (μm)	E_l (K)	g_l	g_u	A_{ul} (s^{-1})	v_{lsr} (km s^{-1})	FWHM (km s^{-1})	W (10^8 Hz)	$\log_{10}(\eta_0)$	$\log_{10}(\tau_p)$
$3_{3,1} - 4_{2,2}$	6.2827	454	9	7	0.4	25.3 ± 2.5	9.0 ± 1.4	1.59 ± 0.50	-0.11	-0.50
$4_{3,1} - 5_{2,4}$	6.2905	598	11	9	0.5	25.9 ± 1.4	8.8 ± 0.7	1.84 ± 0.36	-0.03	-0.43
$5_{3,2} - 6_{2,5}$	6.3388	795	39	33	0.5	25.3 ± 1.2	9.9 ± 0.7	3.25 ± 0.42	0.37	-0.04
$7_{4,3} - 8_{3,6}$	6.3856	1447	51	45	0.5	24.0 ± 1.5	12.2 ± 1.1	2.28 ± 0.27	-0.08	-0.50
$6_{2,4} - 6_{3,3}$	6.4531	951	13	13	11.3	24.2 ± 1.0	14.1 ± 0.3	7.35 ± 0.39	1.21	0.80
$13_{4,9} - 13_{5,8}$	6.4737	3783	81	81	15.0	25.3 ± 0.3	8.9 ± 0.9	1.66 ± 0.21	-0.48	-0.98
$9_{3,6} - 9_{4,5}$	6.4749	1957	57	57	12.7	24.4 ± 0.9	13.4 ± 0.6	6.48 ± 0.43	0.98	0.54
$3_{2,2} - 4_{1,3}$	6.5007	396	9	7	2.3	24.3 ± 0.9	12.8 ± 0.9	8.38 ± 0.77	0.77	0.37
$11_{4,7} - 11_{5,6}$	6.5067	2876	69	69	12.6	25.2 ± 1.2	14.1 ± 0.5	3.54 ± 0.24	0.22	-0.26
$9_{2,7} - 9_{3,6}$	6.5126	1846	57	57	12.2	24.0 ± 1.7	11.1 ± 0.8	4.26 ± 0.74	1.07	0.63
$7_{3,4} - 7_{4,3}$	6.5290	1340	45	45	9.5	24.3 ± 0.9	11.2 ± 0.7	5.55 ± 0.45	1.33	0.91
$13_{5,8} - 13_{6,7}$	6.5392	3966	81	81	12.5	25.7 ± 0.4	8.0 ± 1.0	1.04 ± 0.17	-0.72	-1.22
$10_{4,6} - 10_{5,5}$	6.5401	2482	21	21	11.1	25.9 ± 0.7	9.1 ± 1.7	1.21 ± 0.29	0.02	-0.44
$7_{1,6} - 7_{2,5}$	6.5474	1125	45	45	9.5	24.5 ± 3.4	14.1 ± 1.3	7.20 ± 2.86	1.53	1.12
$7_{4,4} - 8_{3,5}$	6.5818	1511	17	15	0.9	24.7 ± 0.5	10.1 ± 1.3	0.70 ± 0.12	-0.33	-0.76
$13_{3,10} - 13_{4,9}$	6.5832	3646	81	81	13.2	25.6 ± 0.2	9.1 ± 0.7	1.41 ± 0.14	-0.39	-0.89
$6_{3,4} - 6_{4,3}$	6.6007	1088	39	39	7.5	24.6 ± 3.0	14.1 ± 0.5	8.05 ± 2.75	1.42	1.00
$11_{2,9} - 11_{3,8}$	6.6594	2609	69	69	10.7	26.1 ± 0.9	10.5 ± 0.6	3.23 ± 0.28	0.42	-0.04
$9_{3,7} - 9_{4,6}$	6.6642	1929	19	19	9.4	24.8 ± 1.4	8.0 ± 0.9	2.24 ± 0.40	0.44	-0.01
$12_{4,9} - 12_{5,8}$	6.6867	3274	75	75	10.9	25.6 ± 1.1	7.4 ± 0.6	1.20 ± 0.21	-0.14	-0.63
$10_{3,8} - 10_{4,7}$	6.7052	2275	63	63	9.6	24.6 ± 2.3	12.7 ± 1.1	4.04 ± 0.76	0.65	0.20
$6_{3,4} - 7_{2,5}$	6.7146	1125	45	39	2.0	25.0 ± 2.4	9.8 ± 1.0	3.95 ± 1.49	0.82	0.40
$8_{2,7} - 8_{3,6}$	6.7157	1447	51	51	7.7	24.2 ± 2.4	12.0 ± 1.2	4.74 ± 1.03	1.23	0.81
$9_{1,8} - 9_{2,7}$	6.7288	1729	57	57	7.9	24.8 ± 2.3	13.6 ± 1.3	6.48 ± 1.37	1.04	0.60
$7_{0,7} - 7_{1,6}$	6.7731	1013	45	45	4.7	24.7 ± 1.6	12.9 ± 1.0	6.99 ± 0.83	1.38	0.97
$9_{2,8} - 9_{3,7}$	6.7826	1750	19	19	7.5	24.6 ± 1.4	8.8 ± 0.8	2.12 ± 0.40	0.53	0.09

Table 4.4: continued.

Transition	λ (μm)	E_l (K)	g_l	g_u	A_{ul} (s^{-1})	v_{lsr} (km s^{-1})	FWHM (km s^{-1})	W (10^8 Hz)	$\log_{10}(\eta_0)$	$\log_{10}(\tau_p)$
$7_{1,7} - 7_{2,6}$	6.7959	1021	15	15	4.6	24.0 ± 0.9	8.1 ± 1.1	2.71 ± 1.49	0.89	0.48
$12_{3,10} - 12_{4,9}$	6.8144	3058	75	75	9.6	25.8 ± 0.2	10.7 ± 0.7	2.48 ± 0.19	0.03	-0.45
$10_{1,9} - 10_{2,8}$	6.8251	2069	21	21	7.6	26.5 ± 0.2	11.8 ± 0.6	2.93 ± 0.19	0.29	-0.16
$13_{2,11} - 13_{3,10}$	6.8382	3475	81	81	9.8	26.1 ± 0.4	9.8 ± 1.0	1.36 ± 0.17	-0.31	-0.80
$4_{1,3} - 5_{2,4}$	6.8528	598	11	9	6.0	24.2 ± 1.8	11.3 ± 1.1	5.14 ± 0.77	1.18	0.78
$6_{0,6} - 7_{1,7}$	6.8714	843	15	13	8.1	24.9 ± 0.6	13.8 ± 0.5	6.63 ± 0.32	1.25	0.84
$8_{1,8} - 8_{2,7}$	6.8867	1274	51	51	4.4	25.2 ± 1.7	14.1 ± 1.0	6.85 ± 0.80	1.18	0.76
$11_{1,10} - 11_{2,9}$	6.9199	2432	69	69	7.3	25.3 ± 0.3	13.1 ± 0.7	3.06 ± 0.22	0.47	0.01
$11_{2,10} - 11_{3,9}$	6.9380	2439	23	23	7.2	25.8 ± 1.1	8.9 ± 0.7	1.56 ± 0.20	-0.01	-0.47
$7_{1,7} - 8_{0,8}$	6.9588	1070	17	15	7.8	25.8 ± 3.5	13.6 ± 1.7	6.83 ± 1.72	1.10	0.69
$7_{2,6} - 8_{1,7}$	6.9655	1270	17	15	5.7	25.1 ± 0.3	10.8 ± 1.1	3.19 ± 0.37	0.78	0.36
$9_{0,9} - 9_{1,8}$	6.9774	1552	57	57	4.2	24.0 ± 0.5	9.9 ± 0.4	4.08 ± 0.22	0.98	0.55
$9_{1,9} - 9_{2,8}$	6.9833	1554	19	19	4.2	27.1 ± 0.3	13.3 ± 0.9	3.20 ± 0.25	0.50	0.07
$8_{3,6} - 9_{2,7}$	7.0015	1729	57	51	3.4	25.7 ± 1.5	9.6 ± 0.8	2.65 ± 0.54	0.68	0.24
$7_{1,6} - 8_{2,7}$	7.0218	1274	51	45	5.9	24.5 ± 2.4	10.8 ± 1.2	4.27 ± 1.13	1.28	0.86
$12_{2,11} - 12_{3,10}$	7.0231	2824	75	75	7.1	24.4 ± 0.8	8.6 ± 0.6	1.56 ± 0.16	0.15	-0.32
$8_{0,8} - 9_{1,9}$	7.0559	1324	19	17	7.4	24.0 ± 0.4	10.5 ± 0.3	4.15 ± 0.19	0.92	0.50
$8_{2,7} - 9_{1,8}$	7.0617	1552	57	51	5.8	24.0 ± 1.0	11.6 ± 0.7	3.66 ± 0.32	1.08	0.65
$10_{0,10} - 10_{1,9}$	7.0818	1860	21	21	4.1	24.3 ± 1.4	10.7 ± 0.9	1.78 ± 0.23	0.26	-0.18
$10_{1,10} - 10_{2,9}$	7.0846	1861	63	63	4.1	24.6 ± 1.9	11.7 ± 1.2	2.80 ± 0.46	0.74	0.30
$10_{4,7} - 11_{3,8}$	7.0855	2609	69	63	2.2	25.1 ± 2.2	7.9 ± 1.2	1.29 ± 0.45	-0.22	-0.68
$8_{1,7} - 9_{2,8}$	7.0924	1554	19	17	5.9	24.1 ± 1.1	10.5 ± 0.7	2.82 ± 0.30	0.61	0.18
$13_{1,12} - 13_{2,11}$	7.1065	3233	81	81	7.0	25.8 ± 0.4	9.4 ± 1.1	1.59 ± 0.23	-0.18	-0.67
$9_{3,7} - 10_{2,8}$	7.1252	2069	21	19	4.0	24.5 ± 1.2	10.1 ± 0.8	1.65 ± 0.21	0.02	-0.43
$9_{2,8} - 10_{1,9}$	7.1552	1860	21	19	5.8	25.9 ± 0.7	9.8 ± 0.4	2.52 ± 0.18	0.38	-0.06
$11_{0,11} - 11_{1,10}$	7.1889	2194	69	69	4.0	24.7 ± 1.3	10.1 ± 0.5	2.98 ± 0.61	0.48	0.03

Table 4.4: continued.

Transition	λ (μm)	E_l (K)	g_l	g_u	A_{ul} (s^{-1})	v_{lsr} (km s^{-1})	FWHM (km s^{-1})	W (10^8 Hz)	$\log_{10}(\eta_0)$	$\log_{10}(\tau_p)$
$14_{2,13} - 14_{3,12}$	7.2028	3671	87	87	6.9	25.9 ± 2.8	7.9 ± 1.3	0.96 ± 0.49	-0.54	-1.04
$10_{3,8} - 11_{2,9}$	7.2356	2432	69	63	4.3	25.4 ± 3.9	8.7 ± 2.2	1.26 ± 0.69	0.26	-0.20
$9_{2,7} - 10_{3,8}$	7.2872	2081	63	57	4.5	25.1 ± 1.4	11.9 ± 0.9	3.21 ± 0.39	0.57	0.12
$12_{1,12} - 12_{2,11}$	7.3002	2554	75	75	3.9	24.0 ± 2.9	9.4 ± 0.8	1.84 ± 0.39	0.20	-0.27
$11_{2,9} - 12_{3,10}$	7.3945	2824	75	69	4.6	26.8 ± 0.3	10.7 ± 0.9	1.87 ± 0.20	-0.01	-0.48
$3_{0,3} - 4_{3,2}$	7.4108	550	27	21	0.2	26.3 ± 0.4	8.9 ± 1.2	1.13 ± 0.19	0.14	-0.26
$7_{3,4} - 8_{4,5}$	7.4618	1615	51	45	5.2	24.1 ± 1.6	11.5 ± 1.1	4.26 ± 0.63	0.99	0.56
$6_{4,2} - 7_{5,3}$	7.4654	1524	15	13	9.2	24.0 ± 2.3	10.1 ± 1.2	3.27 ± 0.89	0.78	0.35
$6_{4,3} - 7_{5,2}$	7.4708	1525	45	39	9.2	27.7 ± 0.2	15.0 ± 0.5	6.57 ± 0.26	1.26	0.83
$8_{3,5} - 9_{4,6}$	7.5193	1929	19	17	4.4	26.2 ± 0.2	12.4 ± 0.6	2.57 ± 0.16	0.21	-0.23
$13_{1,12} - 14_{2,13}$	7.5407	3350	87	81	5.1	26.3 ± 0.4	10.4 ± 1.2	1.35 ± 0.19	-0.35	-0.83
$9_{3,6} - 10_{4,7}$	7.5567	2275	63	57	3.9	24.4 ± 1.4	11.5 ± 0.9	2.39 ± 0.30	0.38	-0.08
$10_{3,7} - 11_{4,8}$	7.5802	2652	23	21	3.7	24.5 ± 0.8	7.1 ± 0.0	0.71 ± 0.12	-0.43	-0.89
$7_{4,3} - 8_{5,4}$	7.5932	1806	51	45	7.5	24.4 ± 0.9	11.2 ± 0.7	3.88 ± 0.34	1.00	0.56
$7_{4,4} - 8_{5,3}$	7.6127	1807	17	15	7.4	24.7 ± 1.0	7.8 ± 0.6	1.64 ± 0.24	0.52	0.08
$7_{5,2} - 8_{6,3}$	7.6187	2031	51	45	10.1	24.4 ± 1.6	13.9 ± 1.5	5.53 ± 0.79	0.92	0.48
$7_{5,3} - 8_{6,2}$	7.6196	2031	17	15	10.1	24.0 ± 0.4	7.1 ± 0.2	1.91 ± 0.15	0.44	-0.01
$7_{3,5} - 8_{4,4}$	7.6442	1628	17	15	4.3	25.0 ± 1.8	9.9 ± 1.0	1.91 ± 0.41	0.45	0.02
$8_{4,4} - 9_{5,5}$	7.7118	2122	19	17	6.2	26.0 ± 2.0	13.5 ± 0.9	2.60 ± 0.51	0.22	-0.23
$8_{4,5} - 9_{5,4}$	7.7676	2125	57	51	6.0	25.1 ± 1.0	10.7 ± 0.6	2.38 ± 0.25	0.69	0.24
$9_{4,5} - 10_{5,6}$	7.8122	2473	63	57	5.1	25.2 ± 2.6	10.1 ± 1.1	1.84 ± 0.73	0.35	-0.11
$15_{0,15} - 16_{1,16}$	7.8331	3829	99	93	5.1	25.1 ± 0.4	8.0 ± 1.1	0.51 ± 0.09	-0.69	-1.19
$9_{5,5} - 10_{6,4}$	7.9113	2698	21	19	7.1	24.0 ± 0.4	9.6 ± 1.0	0.88 ± 0.11	-0.17	-0.64
$11_{4,7} - 12_{5,8}$	7.9334	3274	75	69	3.7	25.0 ± 1.2	8.3 ± 0.8	0.84 ± 0.13	-0.42	-0.91
$6_{1,6} - 7_{2,5}$	7.9343	1125	45	39	0.4	24.7 ± 1.6	9.9 ± 0.7	1.71 ± 0.44	0.37	-0.04
$9_{4,6} - 10_{5,5}$	7.9452	2482	21	19	4.7	27.3 ± 0.2	10.2 ± 0.6	0.90 ± 0.07	-0.14	-0.60

Table 4.5: Line Parameters for the v=2-1 transition of AFGL 2136. E_l is the energy of the lower level of the transition, g_l and g_u are the statistical weights of the lower and upper levels respectively, A_{ul} is the Einstein A coefficient of the transition, v_{lsr} is the peak velocity of the line, FWHM is the full width at half maximum of the line, W is the equivalent width in units of Hz and τ_p is the peak optical depth of the transition. η_0 is the opacity in the lower level of the transition calculated for $\epsilon = 0.5$. Line data were taken from the HITRAN database (Gordon et al. 2017).

Transition	λ (μm)	E_l (K)	g_l	g_u	A_{ul} (s^{-1})	v_{lsr} (km s^{-1})	FWHM (km s^{-1})	W (10^8 Hz)	$\log_{10}(\eta_0)$	$\log_{10}(\tau_p)$
$4_{4,1} - 3_{3,0}$	5.4373	2745	21	27	9.8	27.5 ± 1.2	7.1 ± 3.2	1.11 ± 0.55	-0.20	-0.54
$5_{3,2} - 4_{2,3}$	5.5105	2745	27	33	6.2	24.0 ± 0.5	7.1 ± 0.5	0.73 ± 0.10	-0.31	-0.66
$6_{3,4} - 5_{2,3}$	5.5218	2955	33	39	6.9	26.6 ± 0.4	9.5 ± 1.1	1.04 ± 0.15	-0.37	-0.71
$11_{0,11} - 10_{1,10}$	5.6670	3892	63	69	27.6	27.2 ± 0.2	9.9 ± 0.6	1.18 ± 0.09	-0.32	-0.65
$3_{3,0} - 2_{2,1}$	5.6872	2507	15	21	10.9	24.9 ± 1.0	9.5 ± 1.3	1.86 ± 0.30	-0.01	-0.36
$10_{1,10} - 9_{0,9}$	5.7202	3615	57	63	26.5	26.3 ± 0.4	10.4 ± 1.1	1.64 ± 0.22	-0.13	-0.45
$6_{2,5} - 5_{1,4}$	5.7627	2879	33	39	10.9	25.5 ± 1.4	11.9 ± 3.2	2.61 ± 1.01	-0.06	-0.40
$9_{0,9} - 8_{1,8}$	5.7769	3364	51	57	25.2	27.0 ± 1.0	11.0 ± 2.8	2.83 ± 0.75	0.04	-0.29
$7_{1,6} - 6_{2,5}$	5.8206	3110	39	45	11.8	26.4 ± 0.4	11.9 ± 1.1	1.54 ± 0.18	-0.14	-0.48
$8_{1,8} - 7_{0,7}$	5.8322	3138	45	51	23.9	27.4 ± 0.2	10.7 ± 0.7	3.64 ± 0.28	0.18	-0.16
$7_{1,6} - 7_{0,7}$	5.8869	3138	45	45	3.7	26.0 ± 0.8	7.1 ± 2.2	0.90 ± 0.34	-0.68	-1.02
$7_{1,7} - 6_{0,6}$	5.8902	2938	13	15	22.4	25.2 ± 1.3	7.3 ± 2.3	1.15 ± 0.42	-0.19	-0.5
$6_{1,6} - 5_{0,5}$	5.9485	2764	33	39	20.7	25.7 ± 0.7	11.4 ± 0.7	4.25 ± 0.32	0.36	0.01
$6_{0,6} - 5_{1,5}$	5.9622	2767	11	13	20.6	25.1 ± 4.6	10.2 ± 9.2	1.58 ± 1.82	-0.12	-0.47
$4_{2,3} - 4_{1,4}$	6.0224	2621	27	27	5.9	25.0 ± 1.3	7.8 ± 2.2	1.09 ± 0.36	-0.21	-0.56
$7_{2,5} - 7_{1,6}$	6.0322	3323	45	45	9.4	26.7 ± 0.3	9.2 ± 0.7	1.04 ± 0.10	-0.38	-0.72
$4_{1,4} - 3_{0,3}$	6.0613	2492	21	27	16.7	24.7 ± 0.8	10.1 ± 0.9	2.88 ± 0.33	0.36	0.01
$5_{1,4} - 5_{0,5}$	6.0802	2764	33	33	6.4	26.5 ± 0.2	11.7 ± 0.6	1.99 ± 0.12	-0.20	-0.54
$2_{2,1} - 2_{1,2}$	6.1010	2413	15	15	5.9	26.0 ± 0.3	10.0 ± 0.7	1.16 ± 0.11	-0.26	-0.62
$3_{2,1} - 3_{1,2}$	6.1716	2550	21	21	12.5	25.8 ± 2.5	8.7 ± 3.8	1.56 ± 0.95	0.11	-0.24
$2_{1,2} - 1_{0,1}$	6.1753	2329	9	15	13.9	26.1 ± 0.8	10.4 ± 0.2	2.65 ± 0.25	0.19	-0.16
$3_{0,3} - 2_{1,2}$	6.2028	2413	15	21	11.9	25.0 ± 0.5	8.0 ± 0.7	1.78 ± 0.19	0.21	-0.15
$1_{1,0} - 1_{0,1}$	6.3157	2329	9	9	21.3	25.4 ± 0.5	7.1 ± 0.9	1.55 ± 0.29	0.19	-0.17

Table 4.5: continued.

Transition	λ (μm)	E_l (K)	g_l	g_u	A_{ul} (s^{-1})	v_{lsr} (km s^{-1})	FWHM (km s^{-1})	W (10^8 Hz)	$\log_{10}(\eta_0)$	$\log_{10}(\tau_p)$
$1_{0,1} - 1_{1,0}$	6.5149	2360	9	9	24.9	26.7 ± 0.2	10.5 ± 0.6	2.19 ± 0.17	0.27	-0.08
$3_{1,2} - 3_{2,1}$	6.5994	2618	21	21	19.1	24.0 ± 1.0	12.8 ± 1.5	3.49 ± 0.46	0.33	-0.02
$5_{1,4} - 5_{2,3}$	6.6160	2955	33	33	23.3	25.1 ± 1.5	11.1 ± 1.7	3.00 ± 0.63	0.32	-0.02
$2_{1,2} - 3_{0,3}$	6.6400	2492	21	15	13.5	24.5 ± 2.0	9.8 ± 3.3	1.76 ± 0.67	0.13	-0.22
$7_{2,5} - 7_{3,4}$	6.6462	3544	45	45	24.4	25.9 ± 0.3	8.4 ± 0.7	1.49 ± 0.16	-0.01	-0.35
$6_{2,4} - 6_{3,3}$	6.6574	3284	13	13	21.6	26.6 ± 0.3	11.0 ± 1.3	0.88 ± 0.12	-0.38	-0.72
$4_{0,4} - 4_{1,3}$	6.6674	2698	9	9	15.1	25.0 ± 1.0	7.4 ± 1.9	0.86 ± 0.26	-0.21	-0.56
$1_{0,1} - 2_{1,2}$	6.6739	2413	15	9	22.9	26.2 ± 0.2	10.4 ± 0.7	2.32 ± 0.19	0.22	-0.14
$9_{3,6} - 9_{4,5}$	6.6888	4315	57	57	23.9	24.4 ± 2.7	8.7 ± 1.9	0.69 ± 0.24	-0.56	-0.88
$9_{2,7} - 9_{3,6}$	6.6895	4180	57	57	25.5	24.5 ± 1.2	8.4 ± 1.6	0.84 ± 0.20	-0.43	-0.75
$7_{1,6} - 7_{2,5}$	6.7261	3443	45	45	20.3	24.2 ± 0.9	7.2 ± 1.8	1.02 ± 0.29	-0.01	-0.34
$3_{2,1} - 3_{3,0}$	6.7334	2745	21	21	9.2	27.7 ± 0.6	13.1 ± 2.0	1.33 ± 0.25	-0.06	-0.40
$5_{0,5} - 5_{1,4}$	6.7653	2879	33	33	12.5	26.5 ± 0.2	11.3 ± 0.7	2.33 ± 0.18	0.14	-0.21
$4_{1,4} - 4_{2,3}$	6.7857	2745	27	27	11.2	24.8 ± 0.4	9.9 ± 1.1	1.28 ± 0.18	0.13	-0.22
$5_{3,2} - 5_{4,1}$	6.7987	3240	33	33	12.1	25.6 ± 0.4	10.3 ± 1.2	1.39 ± 0.20	-0.13	-0.47
$3_{0,3} - 4_{1,4}$	6.8136	2621	27	21	17.1	25.3 ± 0.3	13.2 ± 0.9	2.98 ± 0.25	0.31	-0.04
$6_{2,5} - 6_{3,4}$	6.8285	3269	39	39	15.4	26.7 ± 0.5	11.6 ± 1.3	1.86 ± 0.26	0.01	-0.33
$4_{1,4} - 5_{0,5}$	6.8449	2764	33	27	16.0	25.5 ± 0.5	8.7 ± 1.2	2.17 ± 0.34	0.27	-0.08
$1_{1,0} - 2_{2,1}$	6.8512	2507	15	9	26.0	26.4 ± 0.3	12.1 ± 0.8	2.75 ± 0.23	0.24	-0.11
$3_{1,2} - 4_{2,3}$	7.0096	2745	27	21	13.2	24.3 ± 1.1	9.6 ± 1.6	1.79 ± 0.34	0.13	-0.21
$6_{1,6} - 7_{0,7}$	7.0362	3138	45	39	15.7	24.7 ± 0.6	10.1 ± 1.2	2.15 ± 0.28	0.13	-0.21
$2_{2,1} - 3_{3,0}$	7.0996	2745	21	15	26.7	24.3 ± 0.5	7.1 ± 0.9	1.39 ± 0.29	0.33	-0.02
$5_{1,4} - 6_{2,5}$	7.1217	3110	39	33	11.1	26.0 ± 2.0	7.6 ± 5.4	1.08 ± 0.85	-0.04	-0.38
$7_{1,7} - 8_{0,8}$	7.1324	3363	17	15	15.1	24.3 ± 1.6	7.6 ± 2.0	0.84 ± 0.33	-0.48	-0.82
$7_{0,7} - 8_{1,8}$	7.1381	3364	51	45	15.1	26.0 ± 1.5	9.4 ± 2.7	1.33 ± 0.43	-0.01	-0.34
$3_{2,1} - 4_{3,2}$	7.2050	2885	27	21	18.3	25.3 ± 1.2	13.3 ± 4.0	2.89 ± 0.89	0.21	-0.13

Table 4.5: continued.

Transition	λ (μm)	E_l (K)	g_l	g_u	A_{ul} (s^{-1})	v_{lsr} (km s^{-1})	FWHM (km s^{-1})	W (10^8 Hz)	$\log_{10}(\eta_0)$	$\log_{10}(\tau_p)$
$7_{1,6} - 8_{2,7}$	7.2245	3590	51	45	11.1	25.7 ± 4.8	9.2 ± 6.2	0.82 ± 0.78	-0.30	-0.63
$8_{1,8} - 9_{0,9}$	7.2308	3615	57	51	14.5	26.4 ± 1.4	10.4 ± 1.4	1.75 ± 0.32	-0.17	-0.50
$3_{3,0} - 4_{4,1}$	7.2937	3064	27	21	28.4	26.8 ± 0.9	13.8 ± 1.5	3.05 ± 0.37	0.29	-0.06
$4_{3,2} - 5_{4,1}$	7.4294	3240	33	27	20.9	26.1 ± 0.3	11.4 ± 0.9	1.83 ± 0.18	0.13	-0.21
$5_{3,2} - 6_{4,3}$	7.5509	3451	39	33	16.2	24.5 ± 2.3	7.9 ± 3.0	0.69 ± 0.32	-0.05	-0.39
$6_{3,4} - 7_{4,3}$	7.7350	3701	45	39	12.3	25.8 ± 1.1	7.1 ± 2.3	0.51 ± 0.19	-0.29	-0.61

Table 4.6: Line Parameters for the v=1-0 of $H_2^{18}O$ transition of AFGL 2136. E_l is the energy of the lower level of the transition, g_l and g_u are the statistical weights of the lower and upper levels respectively, A_{ul} is the Einstein A coefficient of the transition, v_{lsr} is the peak velocity of the line, FWHM is the full width at half maximum of the line, W is the equivalent width in units of Hz and τ_p is the peak optical depth of the transition. η_0 is the opacity in the lower level of the transition calculated for $\epsilon = 0.5$. Line data were taken from the HITRAN database (Gordon et al. 2017).

Transition	λ (μm)	E_l (K)	g_l	g_u	A_{ul} (s^{-1})	v_{lsr} (km s^{-1})	FWHM (km s^{-1})	W (10^8 Hz)	$\log_{10}(\eta_0)$	$\log_{10}(\tau_p)$
$2_{1,2} - 1_{0,1}$	6.0743	34	9	15.0	7.0	26.2±0.6	14.3±1.8	1.44±0.16	-0.43	-0.52
$4_{1,4} - 3_{0,3}$	5.9604	196	21	27.0	8.6	25.2±0.4	12.7±1.5	1.35±0.14	-0.39	-0.47
$5_{0,5} - 4_{1,4}$	5.9200	322	27	33.0	9.5	27.6±0.5	8.9±1.4	1.14±0.19	-0.49	-0.56
$2_{2,1} - 1_{1,0}$	5.9095	60	9	15.0	5.9	26.3±0.4	10.5±1.4	0.76±0.16	-0.58	-0.67

Table 4.7: Line Parameters for the v=1-0 transition of AFGL 2591. E_l is the energy of the lower level of the transition, g_l and g_u are the statistical weights of the lower and upper levels respectively, A_{ul} is the Einstein A coefficient of the transition, v_{lsr} is the peak velocity of the line, FWHM is the full width at half maximum of the line, W is the equivalent width in units of Hz and τ_p is the peak optical depth of the transition. η_0 is the opacity in the lower level of the transition calculated for $\epsilon = 0.5$. Line data were taken from the HITRAN database (Gordon et al. 2017).

Transition	λ (μm)	E_l (K)	g_l	g_u	A_{ul} (s^{-1})	v_{lsr} (km s^{-1})	FWHM (km s^{-1})	W (10^8 Hz)	$\log_{10}(\eta_0)$	$\log_{10}(\tau_p)$
$12_{2,11} - 11_{1,10}$	5.3719	2194	69	75	10.9	-9.7 ± 0.3	13.6 ± 0.9	3.69 ± 0.29	0.83	0.80
$12_{1,11} - 11_{2,10}$	5.3737	2194	23	25	10.9	-8.7 ± 0.3	15.9 ± 1.0	3.95 ± 0.26	0.35	0.33
$11_{3,8} - 10_{4,7}$	5.3772	2275	63	69	3.3	-10.3 ± 0.4	13.6 ± 1.2	2.08 ± 0.23	0.22	0.18
$9_{3,7} - 8_{2,6}$	5.3806	1414	17	19	5.0	-8.8 ± 0.3	15.7 ± 0.8	4.04 ± 0.21	0.44	0.50
$8_{6,3} - 8_{5,4}$	5.4172	1806	51	51	1.6	-9.3 ± 0.2	12.5 ± 0.6	2.79 ± 0.16	0.11	0.13
$4_{4,0} - 3_{3,1}$	5.4218	410	7	9	5.4	-11.7 ± 0.1	13.4 ± 0.4	3.57 ± 0.11	0.86	1.03
$9_{6,3} - 9_{5,4}$	5.4238	2125	57	57	1.9	-10.0 ± 0.2	10.4 ± 0.6	1.40 ± 0.10	0.01	-0.01
$11_{2,10} - 10_{1,9}$	5.4248	1860	21	23	10.2	-8.2 ± 0.2	12.8 ± 0.6	3.38 ± 0.15	0.54	0.54
$11_{1,10} - 10_{2,9}$	5.4285	1861	63	69	10.2	-10.2 ± 0.3	15.6 ± 0.4	6.31 ± 0.26	1.01	1.02
$7_{3,5} - 6_{2,4}$	5.4431	867	13	15	3.9	-10.2 ± 0.2	14.5 ± 0.6	3.61 ± 0.14	0.62	0.74
$11_{6,5} - 11_{5,6}$	5.4521	2876	69	69	2.4	-7.0 ± 0.5	11.4 ± 1.5	0.83 ± 0.13	-0.32	-0.43
$5_{3,2} - 4_{2,3}$	5.4641	432	27	33	3.1	-12.1 ± 0.2	16.1 ± 0.2	5.51 ± 0.14	1.17	1.34
$12_{2,11} - 12_{1,12}$	5.4689	2241	75	75	0.7	-9.7 ± 0.2	13.0 ± 1.1	1.54 ± 0.15	-0.39	-0.43
$10_{1,9} - 9_{2,8}$	5.4862	1554	19	21	9.5	-12.0 ± 0.2	14.2 ± 0.2	4.26 ± 0.12	0.69	0.73
$10_{3,7} - 9_{4,6}$	5.4904	1929	19	21	2.6	-12.2 ± 0.4	13.7 ± 1.1	1.24 ± 0.10	-0.13	-0.13
$12_{1,12} - 11_{0,11}$	5.5022	1909	69	75	15.0	-11.9 ± 0.1	16.1 ± 0.4	5.42 ± 0.15	1.20	1.20
$11_{4,7} - 10_{5,6}$	5.5031	2473	63	69	1.7	-10.4 ± 0.3	16.6 ± 1.9	1.49 ± 0.21	-0.17	-0.23
$9_{2,7} - 8_{3,6}$	5.5179	1447	51	57	4.6	-12.2 ± 0.3	13.5 ± 0.2	3.83 ± 0.15	0.89	0.94
$5_{3,3} - 4_{2,2}$	5.5229	454	9 1	1	3.9	-14.1 ± 0.1	15.2 ± 0.5	3.59 ± 0.13	0.80	0.96
$11_{2,10} - 11_{1,11}$	5.5270	1909	23	23	0.8	-9.7 ± 0.3	12.2 ± 1.2	0.80 ± 0.08	-0.58	-0.58
$11_{1,10} - 11_{0,11}$	5.5290	1909	69	69	0.8	-11.5 ± 0.2	15.9 ± 0.7	2.16 ± 0.12	-0.11	-0.10
$12_{4,9} - 12_{3,10}$	5.5298	2824	75	75	2.2	-9.4 ± 0.5	10.8 ± 1.5	0.97 ± 0.16	-0.26	-0.36
$9_{2,8} - 8_{1,7}$	5.5319	1270	17	19	8.8	-13.3 ± 0.2	15.0 ± 0.7	4.22 ± 0.19	0.82	0.89

Table 4.7: continued.

Transition	λ (μm)	E_l (K)	g_l	g_u	A_{ul} (s^{-1})	v_{lsr} (km s^{-1})	FWHM (km s^{-1})	W (10^8 Hz)	$\log_{10}(\eta_0)$	$\log_{10}(\tau_p)$
$13_{3,10} - 13_{2,11}$	5.5373	3233	81	81	2.1	-10.3 ± 0.3	10.7 ± 0.8	0.68 ± 0.07	-0.54	-0.68
$9_{1,8} - 8_{2,7}$	5.5479	1274	51	57	8.7	-13.9 ± 0.1	14.6 ± 0.1	5.95 ± 0.10	1.30	1.37
$10_{5,6} - 10_{4,7}$	5.5496	2275	63	63	2.7	-11.6 ± 0.2	13.0 ± 0.3	2.26 ± 0.09	0.14	0.11
$4_{3,1} - 3_{2,2}$	5.5567	296	7	9	4.3	-15.6 ± 0.2	16.6 ± 0.7	3.86 ± 0.17	0.87	1.04
$9_{5,5} - 9_{4,6}$	5.5599	1929	19	19	2.7	-12.5 ± 0.3	12.0 ± 0.8	1.12 ± 0.08	-0.15	-0.15
$11_{3,9} - 11_{2,10}$	5.5613	2194	23	23	1.7	-10.9 ± 0.2	10.9 ± 0.7	0.79 ± 0.05	-0.45	-0.48
$7_{5,2} - 7_{4,3}$	5.5775	1340	45	45	2.2	-12.7 ± 0.2	13.0 ± 0.2	3.17 ± 0.10	0.56	0.63
$10_{1,9} - 10_{0,10}$	5.5909	1603	21	21	1.0	-13.9 ± 0.2	9.4 ± 0.5	0.97 ± 0.05	-0.32	-0.28
$8_{5,3} - 8_{4,4}$	5.5917	1628	17	17	2.6	-12.1 ± 0.3	14.5 ± 0.8	2.00 ± 0.12	0.01	0.04
$9_{3,6} - 8_{4,5}$	5.6118	1615	51	57	2.0	-12.8 ± 0.2	12.6 ± 0.5	2.45 ± 0.12	0.44	0.47
$8_{2,6} - 7_{3,5}$	5.6208	1175	15	17	3.5	-7.8 ± 0.3	13.1 ± 0.3	3.75 ± 0.18	0.47	0.55
$7_{2,6} - 6_{1,5}$	5.6318	781	13	15	6.9	-14.5 ± 0.2	16.1 ± 0.1	5.16 ± 0.11	0.98	1.10
$9_{2,8} - 9_{1,9}$	5.6485	1324	19	19	1.2	-12.4 ± 0.2	12.7 ± 0.6	1.94 ± 0.09	-0.07	-0.01
$9_{4,6} - 9_{3,7}$	5.6590	1750	19	19	3.0	-11.3 ± 0.2	13.4 ± 0.5	2.05 ± 0.08	0.05	0.08
$10_{2,8} - 10_{1,9}$	5.6645	1860	21	21	2.1	-11.8 ± 0.3	10.6 ± 1.0	0.95 ± 0.09	-0.14	-0.13
$13_{4,9} - 13_{3,10}$	5.6840	3475	81	81	3.7	-10.2 ± 0.6	10.7 ± 1.6	0.84 ± 0.15	-0.42	-0.58
$8_{4,5} - 8_{3,6}$	5.6864	1447	51	51	3.1	-13.7 ± 0.2	16.5 ± 0.9	4.20 ± 0.26	0.72	0.77
$7_{4,4} - 7_{3,5}$	5.7051	1175	15	15	3.1	-12.2 ± 0.4	15.0 ± 1.1	2.86 ± 0.21	0.38	0.46
$10_{5,6} - 9_{6,3}$	5.7081	2347	57	63	1.0	-11.7 ± 0.5	16.3 ± 0.5	3.05 ± 0.16	-0.33	-0.37
$8_{1,8} - 7_{0,7}$	5.7096	843	45	51	12.5	-13.2 ± 0.2	15.7 ± 0.2	7.26 ± 0.22	1.74	1.86
$11_{3,8} - 11_{2,9}$	5.7131	2432	69	69	3.2	-10.3 ± 0.2	13.8 ± 0.7	2.66 ± 0.15	0.18	0.12
$6_{4,3} - 6_{3,4}$	5.7162	933	39	39	2.9	-15.1 ± 0.3	15.6 ± 0.4	5.28 ± 0.21	0.93	1.04
$5_{2,4} - 4_{1,3}$	5.7187	396	9 1	1	5.2	-16.0 ± 0.3	16.0 ± 0.3	4.74 ± 0.19	1.01	1.17
$5_{4,2} - 5_{3,3}$	5.7217	725	11	11	2.4	-13.9 ± 0.3	15.2 ± 0.3	4.30 ± 0.17	0.45	0.58
$4_{4,1} - 4_{3,2}$	5.7238	550	27	27	1.6	-14.0 ± 0.1	14.3 ± 0.4	4.21 ± 0.13	0.78	0.93
$4_{4,0} - 4_{3,1}$	5.7281	552	9	9	1.6	-12.4 ± 0.3	15.0 ± 0.3	3.52 ± 0.15	0.31	0.46

Table 4.7: continued.

Transition	λ (μm)	E_l (K)	g_l	g_u	A_{ul} (s^{-1})	v_{lsr} (km s^{-1})	FWHM (km s^{-1})	W (10^8 Hz)	$\log_{10}(\eta_0)$	$\log_{10}(\tau_p)$
$8_{3,6} - 8_{2,7}$	5.7320	1274	51	51	2.7	-13.0 ± 0.2	16.2 ± 0.7	4.16 ± 0.22	0.78	0.86
$7_{2,5} - 6_{3,4}$	5.7352	933	39	45	2.6	-13.9 ± 0.2	13.1 ± 0.2	4.39 ± 0.16	0.95	1.06
$5_{4,1} - 5_{3,2}$	5.7371	732	33	33	2.5	-13.6 ± 0.2	15.7 ± 0.2	5.57 ± 0.11	0.94	1.07
$9_{2,7} - 9_{1,8}$	5.7494	1552	57	57	2.6	-10.8 ± 0.6	16.3 ± 0.7	4.15 ± 0.33	0.62	0.67
$7_{2,6} - 7_{1,7}$	5.7735	843	15	15	1.7	-12.3 ± 0.2	16.7 ± 0.8	3.61 ± 0.17	0.36	0.48
$7_{3,5} - 7_{2,6}$	5.7792	1021	15	15	3.1	-10.6 ± 0.2	11.9 ± 0.7	2.63 ± 0.16	0.49	0.59
$9_{5,4} - 8_{6,3}$	5.7822	2031	51	57	0.7	-10.5 ± 0.5	18.8 ± 0.8	2.14 ± 0.62	-0.25	-0.26
$7_{1,6} - 7_{0,7}$	5.8022	843	45	45	1.8	-13.2 ± 0.2	15.5 ± 0.6	4.87 ± 0.22	0.86	0.98
$11_{4,7} - 11_{3,8}$	5.8050	2609	69	69	5.3	-11.5 ± 0.3	11.9 ± 0.7	2.72 ± 0.20	0.30	0.22
$6_{3,4} - 6_{2,5}$	5.8180	795	39	39	3.4	-11.6 ± 0.4	14.9 ± 0.6	5.21 ± 0.32	1.11	1.24
$6_{1,6} - 5_{0.5}$	5.8227	468	33	39	10.8	-14.8 ± 0.4	18.8 ± 0.5	6.61 ± 0.27	1.85	2.01
$9_{4,5} - 9_{3,6}$	5.8280	1846	57	57	5.2	-9.9 ± 0.3	14.3 ± 0.3	3.95 ± 0.15	0.74	0.75
$6_{2,5} - 6_{1,6}$	5.8342	643	39	39	2.1	-14.5 ± 0.2	15.2 ± 0.2	5.86 ± 0.11	1.01	1.15
$8_{2,6} - 8_{1,7}$	5.8380	1270	17	17	3.3	-8.5 ± 0.3	17.5 ± 1.0	3.19 ± 0.18	0.42	0.49
$10_{3,8} - 9_{4,5}$	5.8394	1957	57	63	0.7	-9.0 ± 0.3	14.6 ± 1.0	1.89 ± 0.16	-0.17	-0.17
$8_{4,4} - 7_{5,3}$	5.8410	1524	15	17	0.9	-11.6 ± 0.1	9.2 ± 0.4	1.37 ± 0.06	-0.33	-0.28
$5_{3,3} - 5_{2,4}$	5.8473	598	11	11	3.5	-14.0 ± 0.2	12.4 ± 0.7	2.85 ± 0.16	0.72	0.86
$9_{3,7} - 8_{4,4}$	5.8491	1628	17	19	0.9	-9.6 ± 0.3	15.0 ± 0.9	1.83 ± 0.11	-0.34	-0.31
$6_{2,4} - 5_{3,3}$	5.8575	725	11	13	1.8	-11.9 ± 0.2	14.6 ± 0.3	3.45 ± 0.14	0.42	0.56
$8_{4,5} - 7_{5,2}$	5.8656	1525	45	51	0.9	-13.6 ± 0.3	14.4 ± 0.6	2.86 ± 0.16	0.14	0.18
$4_{3,2} - 4_{2,3}$	5.8670	432	27	27	3.2	-15.1 ± 0.4	12.9 ± 0.2	4.41 ± 0.40	1.20	1.36
$9_{3,6} - 9_{2,7}$	5.8729	1729	57	57	5.2	-10.1 ± 0.1	12.8 ± 0.1	5.83 ± 0.07	0.83	0.85
$3_{3,1} - 3_{2,2}$	5.8784	296	7	7	2.4	-15.7 ± 0.2	16.8 ± 0.8	4.73 ± 0.21	0.57	0.75
$8_{3,6} - 7_{4,3}$	5.8860	1340	45	51	1.0	-11.0 ± 0.2	14.9 ± 0.6	3.44 ± 0.16	0.34	0.41
$5_{2,4} - 5_{1,5}$	5.8909	470	11	11	2.5	-12.8 ± 0.1	17.3 ± 0.6	4.27 ± 0.14	0.68	0.84
$4_{3,1} - 4_{2,2}$	5.9167	454	9	9	3.9	-12.8 ± 0.1	14.9 ± 0.1	4.45 ± 0.10	0.79	0.95

Table 4.7: continued.

Transition	λ (μm)	E_l (K)	g_l	g_u	A_{ul} (s^{-1})	v_{lsr} (km s^{-1})	FWHM (km s^{-1})	W (10^8 Hz)	$\log_{10}(\eta_0)$	$\log_{10}(\tau_p)$
$7_{2,5} - 7_{1,6}$	5.9228	1013	45	45	4.4	-10.0 ± 0.3	18.1 ± 0.3	6.21 ± 0.18	1.16	1.26
$8_{3,5} - 8_{2,6}$	5.9246	1414	17	17	6.1	-11.2 ± 0.2	12.3 ± 0.6	2.60 ± 0.13	0.61	0.66
$5_{3,2} - 5_{2,3}$	5.9383	642	33	33	5.0	-13.7 ± 0.2	14.2 ± 0.2	5.04 ± 0.12	1.35	1.49
$7_{3,4} - 7_{2,5}$	5.9507	1125	45	45	6.5	-10.3 ± 0.2	16.0 ± 0.2	6.12 ± 0.16	1.26	1.35
$6_{3,3} - 6_{2,4}$	5.9530	867	13	13	6.0	-11.5 ± 0.2	17.0 ± 0.7	4.94 ± 0.20	0.87	0.99
$6_{3,3} - 5_{4,2}$	5.9792	878	11	13	0.8	-9.5 ± 0.2	14.7 ± 0.8	2.36 ± 0.12	-0.04	0.08
$6_{2,4} - 6_{1,5}$	5.9942	781	13	13	5.8	-12.3 ± 0.2	13.0 ± 0.5	3.77 ± 0.14	0.92	1.05
$6_{3,4} - 5_{4,1}$	6.0191	878	33	39	0.7	-12.3 ± 0.4	13.9 ± 0.4	3.14 ± 0.18	0.42	0.53
$6_{4,3} - 5_{5,0}$	6.0375	1067	33	39	0.3	-11.3 ± 0.3	13.7 ± 0.4	1.81 ± 0.10	-0.14	-0.04
$5_{2,3} - 5_{1,4}$	6.0441	574	33	33	7.2	-15.5 ± 0.5	17.0 ± 0.4	5.02 ± 0.26	1.57	1.72
$5_{2,4} - 4_{3,1}$	6.0964	552	9	11	0.7	-12.3 ± 0.2	15.7 ± 0.6	2.66 ± 0.10	0.14	0.29
$4_{1,4} - 3_{2,1}$	6.2133	305	21	27	0.4	-12.7 ± 0.4	12.6 ± 0.5	3.61 ± 0.25	0.47	0.65
$3_{3,0} - 4_{2,3}$	6.2218	432	27	21	0.3	-14.7 ± 0.4	16.5 ± 1.3	3.40 ± 0.32	0.14	0.30
$2_{2,0} - 3_{1,3}$	6.2453	204	7	5	0.4	-14.2 ± 0.5	9.5 ± 1.4	0.93 ± 0.14	-0.21	-0.03
$3_{2,1} - 4_{1,4}$	6.2716	323	27	21	0.3	-13.7 ± 0.5	10.8 ± 0.5	3.08 ± 0.27	0.28	0.45
$3_{3,1} - 4_{2,2}$	6.2827	454	9	7	0.4	-12.0 ± 1.0	13.9 ± 1.1	1.69 ± 0.33	-0.25	-0.09
$2_{2,1} - 3_{1,2}$	6.3737	249	21	15	1.1	-11.4 ± 0.5	15.8 ± 0.6	4.71 ± 0.31	0.73	0.91
$1_{1,1} - 2_{0,2}$	6.3903	100	5	3	5.3	-13.3 ± 0.4	12.3 ± 1.4	2.76 ± 0.32	0.80	1.00
$4_{1,3} - 4_{2,2}$	6.4115	454	9	9	11.5	-14.2 ± 0.4	14.1 ± 1.6	3.88 ± 0.45	1.37	1.53
$7_{2,5} - 7_{3,4}$	6.4506	1212	45	45	12.5	-14.4 ± 0.4	18.8 ± 1.6	5.39 ± 0.55	1.59	1.67
$6_{2,4} - 6_{3,3}$	6.4531	951	13	13	11.3	-15.0 ± 0.5	18.8 ± 1.7	5.16 ± 0.48	1.19	1.30
$12_{4,8} - 12_{5,7}$	6.4820	3310	25	25	13.9	13.1 ± 0.7	14.0 ± 2.2	1.85 ± 0.29	-0.07	-0.22
$9_{2,7} - 9_{3,6}$	6.5126	1846	57	57	12.2	-13.7 ± 0.5	18.7 ± 2.1	5.04 ± 0.68	1.25	1.27
$13_{5,8} - 13_{6,7}$	6.5392	3966	81	81	12.5	-10.6 ± 1.0	12.8 ± 0.9	1.21 ± 0.19	-0.05	-0.27
$10_{4,6} - 10_{5,5}$	6.5401	2482	21	21	11.1	-9.1 ± 8.0	18.8 ± 1.8	2.25 ± 0.50	0.34	0.29
$7_{4,4} - 8_{3,5}$	6.5818	1511	17	15	0.9	-4.7 ± 3.9	17.0 ± 1.1	1.75 ± 0.27	-0.23	-0.18

Table 4.7: continued.

Transition	λ (μm)	E_l (K)	g_l	g_u	A_{ul} (s^{-1})	v_{lsr} (km s^{-1})	FWHM (km s^{-1})	W (10^8 Hz)	$\log_{10}(\eta_0)$	$\log_{10}(\tau_p)$
$5_{3,3} - 5_{4,2}$	6.5950	878	11	11	6.1	-14.4 ± 0.4	18.8 ± 0.2	3.73 ± 0.04	0.93	1.04
$6_{3,4} - 6_{4,3}$	6.6007	1088	39	39	7.5	-15.7 ± 0.5	17.0 ± 0.5	4.46 ± 0.25	1.42	1.51
$10_{4,7} - 10_{5,6}$	6.6409	2473	63	63	10.0	-10.9 ± 0.4	13.5 ± 1.1	2.68 ± 0.27	0.80	0.74
$9_{3,7} - 9_{4,6}$	6.6642	1929	19	19	9.4	-11.9 ± 0.3	14.1 ± 0.9	2.61 ± 0.18	0.64	0.64
$10_{3,8} - 10_{4,7}$	6.7052	2275	63	63	9.6	-11.9 ± 0.2	15.6 ± 0.5	3.47 ± 0.13	0.93	0.90
$6_{1,6} - 6_{2,5}$	6.7121	795	39	39	4.9	-15.0 ± 0.3	12.1 ± 0.8	3.39 ± 0.26	1.46	1.59
$6_{3,4} - 7_{2,5}$	6.7146	1125	45	39	2.0	-14.6 ± 0.5	16.0 ± 0.4	3.45 ± 0.17	0.83	0.92
$8_{2,7} - 8_{3,6}$	6.7157	1447	51	51	7.7	-11.9 ± 0.3	15.6 ± 0.9	4.92 ± 0.35	1.32	1.38
$8_{2,7} - 8_{3,6}$	6.7157	1447	51	51	7.7	-12.4 ± 0.5	17.6 ± 0.5	5.19 ± 0.35	1.32	1.38
$11_{3,9} - 11_{4,8}$	6.7557	2652	23	23	9.6	-10.6 ± 0.3	12.7 ± 0.7	1.89 ± 0.11	0.24	0.17
$14_{4,11} - 14_{5,10}$	6.7668	4199	87	87	11.3	-9.8 ± 0.6	11.4 ± 1.6	0.98 ± 0.17	-0.18	-0.43
$7_{0,7} - 7_{1,6}$	6.7731	1013	45	45	4.7	-14.7 ± 0.3	14.7 ± 0.3	4.53 ± 0.15	1.37	1.47
$9_{2,8} - 9_{3,7}$	6.7826	1750	19	19	7.5	-12.0 ± 0.3	12.4 ± 0.8	3.06 ± 0.20	0.69	0.71
$7_{1,7} - 7_{2,6}$	6.7959	1021	15	15	4.6	-14.2 ± 0.5	16.5 ± 0.6	4.48 ± 0.35	0.88	0.98
$12_{3,10} - 12_{4,9}$	6.8144	3058	75	75	9.6	-10.4 ± 0.3	11.7 ± 0.9	2.01 ± 0.19	0.48	0.36
$10_{1,9} - 10_{2,8}$	6.8251	2069	21	21	7.6	-10.3 ± 0.3	10.4 ± 0.9	1.77 ± 0.15	0.52	0.50
$6_{2,5} - 7_{1,6}$	6.8631	1013	45	39	5.3	-15.0 ± 0.5	18.2 ± 1.5	4.38 ± 0.44	1.37	1.47
$6_{0,6} - 7_{1,7}$	6.8714	843	15	13	8.1	-16.3 ± 0.2	13.9 ± 1.2	3.20 ± 0.28	1.20	1.32
$8_{0,8} - 8_{1,7}$	6.8749	1270	17	17	4.4	-14.9 ± 0.3	13.3 ± 0.9	2.88 ± 0.18	0.76	0.83
$8_{1,8} - 8_{2,7}$	6.8867	1274	51	51	4.4	-15.0 ± 0.9	15.5 ± 1.5	3.30 ± 0.39	1.23	1.31
$5_{1,4} - 6_{2,5}$	6.9063	795	39	33	5.8	-17.6 ± 0.3	15.2 ± 0.3	4.61 ± 0.19	1.50	1.62
$7_{1,7} - 8_{0,8}$	6.9588	1070	17	15	7.8	-14.3 ± 0.3	17.5 ± 1.2	3.86 ± 0.27	1.10	1.20
$7_{2,6} - 8_{1,7}$	6.9655	1270	17	15	5.7	-7.2 ± 1.6	18.8 ± 1.0	3.83 ± 0.49	0.83	0.90
$9_{0,9} - 9_{1,8}$	6.9774	1552	57	57	4.2	-13.1 ± 0.2	14.8 ± 0.3	3.78 ± 0.11	1.09	1.13
$9_{1,9} - 9_{2,8}$	6.9833	1554	19	19	4.2	-11.5 ± 0.3	16.9 ± 1.0	3.32 ± 0.20	0.61	0.65
$3_{2,2} - 4_{3,1}$	6.9933	552	9	7	8.6	-17.1 ± 0.2	13.2 ± 0.7	2.99 ± 0.16	1.18	1.33

Table 4.7: continued.

Transition	λ (μm)	E_l (K)	g_l	g_u	A_{ul} (s^{-1})	v_{lsr} (km s^{-1})	FWHM (km s^{-1})	W (10^8 Hz)	$\log_{10}(\eta_0)$	$\log_{10}(\tau_p)$
$8_{3,6} - 9_{2,7}$	7.0015	1729	57	51	3.4	-10.1 ± 0.5	10.9 ± 1.4	2.04 ± 0.33	0.83	0.85
$12_{1,11} - 12_{2,10}$	7.0134	2820	25	25	7.1	-9.9 ± 0.4	11.8 ± 1.1	1.46 ± 0.13	0.08	-0.01
$7_{1,6} - 8_{2,7}$	7.0218	1274	51	45	5.9	-12.4 ± 0.5	16.3 ± 0.6	4.54 ± 0.29	1.33	1.40
$12_{2,11} - 12_{3,10}$	7.0231	2824	75	75	7.1	-10.2 ± 0.3	12.7 ± 1.0	2.00 ± 0.20	0.56	0.46
$4_{2,2} - 5_{3,3}$	7.0475	725	11	9	6.8	-17.7 ± 0.4	13.1 ± 1.3	2.90 ± 0.28	1.08	1.21
$8_{1,8} - 9_{0,9}$	7.0547	1324	57	51	7.4	-13.7 ± 0.3	13.6 ± 0.3	4.51 ± 0.23	1.46	1.52
$8_{2,7} - 9_{1,8}$	7.0617	1552	57	51	5.8	-14.9 ± 0.2	14.3 ± 0.5	3.40 ± 0.14	1.19	1.24
$10_{0,10} - 10_{1,9}$	7.0818	1860	21	21	4.1	-12.5 ± 0.2	10.3 ± 0.6	1.50 ± 0.09	0.45	0.46
$10_{1,10} - 10_{2,9}$	7.0846	1861	63	63	4.1	-11.7 ± 0.2	12.9 ± 0.2	3.19 ± 0.12	0.92	0.93
$8_{1,7} - 9_{2,8}$	7.0924	1554	19	17	5.9	-12.6 ± 0.2	14.8 ± 0.6	3.29 ± 0.14	0.73	0.77
$13_{1,12} - 13_{2,11}$	7.1065	3233	81	81	7.0	-11.1 ± 0.4	13.7 ± 0.5	1.92 ± 0.12	0.32	0.18
$5_{2,3} - 6_{3,4}$	7.1175	933	39	33	5.5	-17.4 ± 0.5	14.2 ± 0.3	3.63 ± 0.18	1.42	1.53
$9_{3,7} - 10_{2,8}$	7.1252	2069	21	19	4.0	-12.4 ± 0.2	11.2 ± 0.6	1.83 ± 0.10	0.25	0.24
$4_{2,3} - 5_{3,2}$	7.1469	732	33	27	5.6	-18.0 ± 0.2	12.8 ± 0.2	3.77 ± 0.13	1.49	1.62
$9_{0,9} - 10_{1,10}$	7.1544	1603	63	57	7.1	-12.7 ± 0.3	12.9 ± 1.0	2.99 ± 0.28	1.31	1.35
$4_{3,1} - 5_{4,2}$	7.1643	878	11	9	10.4	-17.8 ± 0.3	15.4 ± 0.9	3.91 ± 0.24	1.18	1.30
$11_{0,11} - 11_{1,10}$	7.1889	2194	69	69	4.0	-12.3 ± 0.3	15.4 ± 0.7	3.13 ± 0.17	0.74	0.71
$11_{1,11} - 11_{2,10}$	7.1903	2194	23	23	4.0	-11.6 ± 0.2	11.7 ± 0.2	1.74 ± 0.08	0.26	0.24
$14_{1,13} - 14_{2,12}$	7.2001	3670	29	29	6.9	-8.7 ± 0.5	12.5 ± 1.3	0.85 ± 0.09	-0.42	-0.61
$7_{2,5} - 8_{3,6}$	7.2125	1447	51	45	4.5	-14.5 ± 0.2	15.2 ± 0.6	3.36 ± 0.15	1.13	1.18
$11_{4,8} - 12_{3,9}$	7.2383	3030	25	23	2.7	-9.1 ± 0.6	12.3 ± 1.5	0.70 ± 0.09	-0.48	-0.59
$7_{1,6} - 7_{4,3}$	7.2543	1340	45	45	0.2	-12.9 ± 0.5	11.0 ± 1.2	1.04 ± 0.14	-0.14	-0.08
$4_{1,4} - 5_{2,3}$	7.2723	642	33	27	1.2	-17.3 ± 0.2	14.3 ± 0.2	3.16 ± 0.09	0.91	1.05
$5_{3,2} - 6_{4,3}$	7.2792	1088	39	33	8.0	-17.4 ± 0.3	15.3 ± 0.3	4.12 ± 0.14	1.51	1.60
$9_{2,7} - 10_{3,8}$	7.2872	2081	63	57	4.5	-10.8 ± 0.2	12.8 ± 0.2	2.75 ± 0.10	0.80	0.78
$12_{1,12} - 12_{2,11}$	7.3002	2554	75	75	3.9	-11.7 ± 0.2	10.8 ± 0.7	1.70 ± 0.13	0.54	0.47

Table 4.7: continued.

Transition	λ (μm)	E_l (K)	g_l	g_u	A_{ul} (s^{-1})	v_{lsr} (km s^{-1})	FWHM (km s^{-1})	W (10^8 Hz)	$\log_{10}(\eta_0)$	$\log_{10}(\tau_p)$
$5_{2,4} - 6_{3,3}$	7.3389	951	13	11	3.6	-14.7 ± 0.6	16.2 ± 0.6	3.06 ± 0.25	0.78	0.89
$11_{2,9} - 12_{3,10}$	7.3945	2824	75	69	4.6	-9.4 ± 0.3	14.3 ± 1.0	2.44 ± 0.22	0.40	0.30
$12_{2,11} - 13_{1,12}$	7.4401	2939	81	75	5.4	-9.6 ± 0.6	10.6 ± 1.6	1.70 ± 0.32	0.43	0.32
$12_{1,11} - 13_{2,12}$	7.4423	2939	27	25	5.4	-11.1 ± 0.4	14.2 ± 1.4	1.82 ± 0.17	-0.05	-0.15
$7_{3,4} - 8_{4,5}$	7.4618	1615	51	45	5.2	-12.0 ± 0.2	10.5 ± 0.8	2.53 ± 0.22	1.11	1.15
$6_{4,2} - 7_{5,3}$	7.4654	1524	15	13	9.2	-11.5 ± 0.6	16.8 ± 1.8	3.78 ± 0.40	0.89	0.94
$6_{4,3} - 7_{5,2}$	7.4708	1525	45	39	9.2	-12.9 ± 0.3	15.8 ± 0.3	3.84 ± 0.15	1.37	1.41
$12_{1,12} - 13_{0,13}$	7.4744	2599	81	75	6.1	-9.3 ± 0.3	12.3 ± 0.8	2.01 ± 0.16	0.72	0.65
$8_{3,5} - 9_{4,6}$	7.5193	1929	19	17	4.4	-10.6 ± 0.3	13.5 ± 0.3	2.14 ± 0.13	0.41	0.41
$14_{1,14} - 14_{2,13}$	7.5326	3350	87	87	3.9	-10.7 ± 0.5	12.0 ± 1.4	1.57 ± 0.23	0.08	-0.07
$13_{2,12} - 14_{1,13}$	7.5396	3350	29	27	5.1	-11.8 ± 0.8	13.9 ± 2.4	0.94 ± 0.16	-0.30	-0.45
$13_{2,11} - 14_{3,12}$	7.5437	3671	87	81	4.5	-7.4 ± 0.3	9.7 ± 0.7	1.24 ± 0.11	-0.11	-0.29
$13_{2,11} - 14_{3,12}$	7.5437	3671	87	81	4.5	-7.6 ± 0.3	11.7 ± 1.1	1.72 ± 0.16	-0.11	-0.29
$9_{3,6} - 10_{4,7}$	7.5567	2275	63	57	3.9	-12.4 ± 0.9	18.7 ± 0.9	3.47 ± 0.22	0.65	0.62
$5_{1,5} - 6_{2,4}$	7.5754	867	13	11	0.7	-14.0 ± 0.4	12.7 ± 1.0	1.63 ± 0.12	0.16	0.28
$10_{3,7} - 11_{4,8}$	7.5802	2652	23	21	3.7	-10.0 ± 4.9	14.5 ± 1.8	1.26 ± 0.36	-0.07	-0.14
$6_{2,5} - 7_{3,4}$	7.5819	1212	45	39	2.2	-11.4 ± 0.8	17.4 ± 0.7	3.78 ± 0.28	0.98	1.06
$7_{6,1} - 8_{7,2}$	7.6060	2289	51	45	12.8	-12.6 ± 0.3	13.2 ± 0.3	3.37 ± 0.12	1.07	1.03
$14_{2,13} - 15_{1,14}$	7.6420	3786	93	87	4.9	-10.1 ± 0.7	8.8 ± 1.7	0.60 ± 0.15	-0.10	-0.30
$8_{4,4} - 9_{5,5}$	7.7118	2122	19	17	6.2	-5.7 ± 0.2	12.3 ± 0.2	2.97 ± 0.10	0.46	0.44
$8_{4,5} - 9_{5,4}$	7.7676	2125	57	51	6.0	-11.7 ± 0.1	13.9 ± 0.1	3.16 ± 0.06	0.93	0.91
$9_{8,2} - 10_{9,1}$	7.8054	3556	21	19	13.4	-10.7 ± 0.4	9.0 ± 1.0	0.84 ± 0.10	-0.14	-0.31
$9_{4,5} - 10_{5,6}$	7.8122	2473	63	57	5.1	-8.3 ± 0.3	14.2 ± 0.8	1.88 ± 0.14	0.68	0.62
$9_{4,6} - 10_{5,5}$	7.9452	2482	21	19	4.7	-9.8 ± 0.5	15.7 ± 1.4	1.31 ± 0.12	0.18	0.12

Table 4.8: Line Parameters for the v=2-1 transition of AFGL 2591. E_l is the energy of the lower level of the transition, g_l and g_u are the statistical weights of the lower and upper levels respectively, A_{ul} is the Einstein A coefficient of the transition, v_{lsr} is the peak velocity of the line, FWHM is the full width at half maximum of the line, W is the equivalent width in units of Hz and τ_p is the peak optical depth of the transition. η_0 is the opacity in the lower level of the transition calculated for $\epsilon = 0.5$. Line data were taken from the HITRAN database (Gordon et al. 2017).

Transition	λ (μm)	E_l (K)	g_l	g_u	A_{ul} (s^{-1})	v_{lsr} (km s^{-1})	FWHM (km s^{-1})	W (10^8 Hz)	$\log_{10}(\eta_0)$	$\log_{10}(\tau_p)$
$10_{3,8} - 9_{2,7}$	5.4015	4055	57	63.0	10.1	-8.6 ± 0.3	8.5 ± 0.9	0.81 ± 0.11	-0.62	-0.77
$4_{4,1} - 3_{3,0}$	5.4373	2745	21	27.0	9.8	-9.5 ± 0.3	11.4 ± 0.8	1.36 ± 0.12	0.01	-0.18
$5_{3,2} - 4_{2,3}$	5.5105	2745	27	33.0	6.2	-10.6 ± 0.3	10.6 ± 0.7	1.35 ± 0.11	-0.11	-0.30
$6_{3,4} - 5_{2,3}$	5.5218	2955	33	39.0	6.9	-11.1 ± 0.3	8.2 ± 0.8	1.29 ± 0.16	-0.14	-0.32
$11_{0,11} - 10_{1,10}$	5.6670	3892	63	69.0	27.6	-11.1 ± 0.3	10.1 ± 0.9	1.62 ± 0.18	0.02	-0.14
$10_{1,10} - 9_{0,9}$	5.7202	3615	57	63.0	26.5	-11.9 ± 0.3	13.3 ± 0.9	2.08 ± 0.19	0.18	0.02
$8_{1,7} - 7_{2,6}$	5.7330	3336	15	17.0	14.1	-10.1 ± 0.6	11.6 ± 1.7	0.90 ± 0.16	-0.43	-0.60
$6_{2,5} - 5_{1,4}$	5.7627	2879	33	39.0	10.9	-10.0 ± 0.3	11.5 ± 0.8	1.92 ± 0.16	0.16	-0.02
$9_{1,9} - 8_{0,8}$	5.7754	3363	17	19.0	25.2	-9.5 ± 0.4	14.1 ± 2.7	1.67 ± 0.53	-0.16	-0.32
$9_{0,9} - 8_{1,8}$	5.7769	3364	51	57.0	25.2	-11.0 ± 0.3	14.1 ± 0.2	2.32 ± 0.13	0.32	0.15
$5_{2,4} - 4_{1,3}$	5.8037	2698	9	11.0	9.7	-7.5 ± 0.5	9.8 ± 1.8	0.71 ± 0.16	-0.30	-0.49
$7_{1,6} - 6_{2,5}$	5.8206	3110	39	45.0	11.8	-7.5 ± 0.2	12.2 ± 0.8	2.75 ± 0.22	0.11	-0.07
$8_{0,8} - 7_{1,7}$	5.8353	3138	15	17.0	23.9	-7.0 ± 0.5	13.2 ± 1.2	2.28 ± 0.25	-0.04	-0.22
$3_{3,1} - 3_{2,2}$	5.9287	2610	7	7.0	4.3	-11.6 ± 0.4	8.1 ± 1.5	0.41 ± 0.09	-0.74	-0.93
$3_{3,0} - 3_{2,1}$	5.9478	2618	21	21.0	4.5	-9.2 ± 0.3	9.6 ± 0.8	0.83 ± 0.09	-0.24	-0.44
$6_{1,6} - 5_{0,5}$	5.9485	2764	33	39.0	20.7	-9.7 ± 0.2	13.6 ± 0.5	2.94 ± 0.14	0.56	0.38
$6_{0,6} - 5_{1,5}$	5.9622	2767	11	13.0	20.6	-10.1 ± 0.3	10.1 ± 0.7	1.25 ± 0.11	0.08	-0.10
$5_{3,2} - 5_{2,3}$	5.9925	2955	33	33.0	8.7	-7.3 ± 0.3	11.3 ± 0.9	1.51 ± 0.15	-0.01	-0.19
$5_{1,5} - 4_{0,4}$	6.0059	2615	9	11.0	18.8	-8.5 ± 0.4	11.1 ± 1.2	1.22 ± 0.17	0.09	-0.10
$7_{3,4} - 7_{2,5}$	6.0232	3443	45	45.0	11.8	-10.6 ± 0.3	12.3 ± 0.8	1.63 ± 0.13	-0.10	-0.27
$7_{2,5} - 7_{1,6}$	6.0322	3323	45	45.0	9.4	-10.8 ± 0.3	14.1 ± 1.0	1.38 ± 0.12	-0.11	-0.28
$2_{2,1} - 2_{1,2}$	6.1010	2413	15	15.0	5.9	-9.7 ± 0.2	13.8 ± 0.6	1.68 ± 0.09	-0.10	-0.30
$3_{0,3} - 2_{1,2}$	6.2028	2413	15	21.0	11.9	-9.8 ± 0.4	14.1 ± 0.1	3.18 ± 0.30	0.37	0.17

Table 4.8: continued.

Transition	λ (μm)	E_l (K)	g_l	g_u	A_{ul} (s^{-1})	v_{lsr} (km s^{-1})	FWHM (km s^{-1})	W (10^8 Hz)	$\log_{10}(\eta_0)$	$\log_{10}(\tau_p)$
$2_{1,1} - 2_{0,2}$	6.2878	2396	5	5.0	17.7	-9.7 ± 0.6	8.6 ± 1.5	1.40 ± 0.31	-0.05	-0.25
$1_{1,0} - 1_{0,1}$	6.3157	2329	9	9.0	21.3	-14.5 ± 0.4	10.4 ± 1.0	2.43 ± 0.29	0.34	0.14
$1_{0,1} - 1_{1,0}$	6.5149	2360	9	9.0	24.9	-9.9 ± 0.4	12.7 ± 1.7	2.08 ± 0.33	0.43	0.23
$7_{2,5} - 7_{3,4}$	6.6462	3544	45	45.0	24.4	-10.7 ± 0.3	12.3 ± 0.9	1.84 ± 0.16	0.28	0.11
$4_{0,4} - 4_{1,3}$	6.6674	2698	9	9.0	15.1	-8.3 ± 0.4	12.5 ± 1.1	1.75 ± 0.18	-0.01	-0.20
$9_{2,7} - 9_{3,6}$	6.6895	4180	57	57.0	25.5	-9.6 ± 0.5	15.0 ± 1.7	1.20 ± 0.16	-0.06	-0.21
$7_{1,6} - 7_{2,5}$	6.7261	3443	45	45.0	20.3	-11.9 ± 0.4	12.5 ± 1.0	1.63 ± 0.16	0.28	0.11
$3_{2,1} - 3_{3,0}$	6.7334	2745	21	21.0	9.2	-13.3 ± 1.0	14.1 ± 2.9	1.45 ± 0.37	0.14	-0.05
$7_{3,4} - 7_{4,3}$	6.7536	3701	45	45.0	18.0	-11.9 ± 0.4	12.4 ± 1.0	1.32 ± 0.14	0.07	-0.09
$5_{0,5} - 5_{1,4}$	6.7653	2879	33	33.0	12.5	-12.2 ± 0.5	13.1 ± 1.2	1.71 ± 0.20	0.36	0.17
$4_{2,3} - 4_{3,2}$	6.7693	2885	27	27.0	12.6	-12.1 ± 0.4	13.2 ± 1.0	1.44 ± 0.14	0.29	0.11
$5_{3,2} - 5_{4,1}$	6.7987	3240	33	33.0	12.1	-11.2 ± 0.4	11.8 ± 0.9	1.50 ± 0.15	0.12	-0.05
$4_{3,2} - 4_{4,1}$	6.8108	3064	27	27.0	7.7	-9.5 ± 0.7	13.5 ± 1.9	1.16 ± 0.21	-0.03	-0.21
$3_{0,3} - 4_{1,4}$	6.8136	2621	27	21.0	17.1	-11.9 ± 0.4	13.5 ± 1.2	2.12 ± 0.23	0.49	0.30
$8_{1,7} - 8_{2,6}$	6.8165	3735	17	17.0	18.4	-9.8 ± 0.5	10.9 ± 1.7	1.11 ± 0.21	-0.38	-0.54
$4_{1,4} - 5_{0,5}$	6.8449	2764	33	27.0	16.0	-10.1 ± 0.5	11.6 ± 0.5	2.00 ± 0.20	0.47	0.29
$1_{1,0} - 2_{2,1}$	6.8512	2507	15	9.0	26.0	-10.5 ± 0.3	13.0 ± 0.8	2.01 ± 0.16	0.41	0.22
$5_{1,5} - 6_{0,6}$	6.9411	2938	13	11.0	16.0	-11.9 ± 0.6	9.0 ± 1.5	0.90 ± 0.19	-0.03	-0.21
$7_{0,7} - 7_{1,6}$	6.9985	3323	45	45.0	10.0	-8.0 ± 0.4	13.8 ± 1.7	1.82 ± 0.27	0.11	-0.06
$6_{1,6} - 7_{0,7}$	7.0362	3138	45	39.0	15.7	-10.4 ± 0.4	15.1 ± 1.3	2.00 ± 0.20	0.38	0.20
$2_{2,0} - 3_{3,1}$	7.0934	2744	7	5.0	26.9	-10.6 ± 0.3	9.7 ± 0.9	1.07 ± 0.12	0.06	-0.13
$2_{2,1} - 3_{3,0}$	7.0996	2745	21	15.0	26.7	-11.3 ± 0.3	15.8 ± 0.9	2.39 ± 0.18	0.53	0.34
$5_{1,4} - 6_{2,5}$	7.1217	3110	39	33.0	11.1	-9.8 ± 0.2	9.8 ± 0.6	1.23 ± 0.10	0.21	0.03
$7_{0,7} - 8_{1,8}$	7.1381	3364	51	45.0	15.1	-11.3 ± 0.4	13.1 ± 1.4	1.72 ± 0.22	0.27	0.10
$8_{1,8} - 8_{2,7}$	7.1424	3590	51	51.0	9.2	-10.2 ± 0.6	9.5 ± 1.4	0.78 ± 0.15	-0.04	-0.20
$7_{1,6} - 8_{2,7}$	7.2245	3590	51	45.0	11.1	-11.8 ± 0.2	10.0 ± 0.6	0.87 ± 0.07	0.01	-0.16

Table 4.8: continued.

Transition	λ (μm)	E_l (K)	g_l	g_u	A_{ul} (s^{-1})	v_{lsr} (km s^{-1})	FWHM (km s^{-1})	W (10^8 Hz)	$\log_{10}(\eta_0)$	$\log_{10}(\tau_p)$
$8_{2,7} - 9_{1,8}$	7.2272	3868	57	51.0	10.9	-12.1 ± 0.3	10.3 ± 0.7	0.85 ± 0.08	-0.16	-0.31
$3_{2,2} - 4_{3,1}$	7.2371	2886	9	7.0	17.5	-11.4 ± 0.8	13.5 ± 2.1	1.01 ± 0.20	-0.07	-0.25
$9_{0,9} - 9_{1,8}$	7.2431	3868	57	57.0	8.9	-11.6 ± 0.3	10.2 ± 1.0	0.72 ± 0.09	-0.19	-0.35
$3_{3,0} - 4_{4,1}$	7.2937	3064	27	21.0	28.4	-11.6 ± 0.2	11.0 ± 0.5	1.54 ± 0.08	0.52	0.34
$4_{2,2} - 5_{3,3}$	7.3018	3060	11	9.0	13.7	-13.4 ± 0.2	8.2 ± 0.6	1.05 ± 0.10	-0.18	-0.36
$9_{2,8} - 10_{1,9}$	7.3255	4177	21	19.0	11.0	-14.5 ± 0.5	7.7 ± 1.2	0.49 ± 0.10	-0.80	-0.94
$9_{1,9} - 10_{0,10}$	7.3323	3892	21	19.0	13.8	-10.7 ± 0.4	9.7 ± 1.1	0.69 ± 0.10	-0.50	-0.66
$9_{0,9} - 10_{1,10}$	7.3337	3892	63	57.0	13.8	-9.5 ± 0.3	10.2 ± 0.3	1.22 ± 0.07	-0.03	-0.18
$4_{3,2} - 5_{4,1}$	7.4294	3240	33	27.0	20.9	-10.1 ± 0.4	10.9 ± 1.0	1.70 ± 0.19	0.39	0.21
$5_{3,2} - 6_{4,3}$	7.5509	3451	39	33.0	16.2	-11.5 ± 0.4	11.4 ± 1.0	1.25 ± 0.14	0.23	0.06
$5_{3,3} - 6_{4,2}$	7.5739	3452	13	11.0	16.0	-7.0 ± 0.1	10.0 ± 1.7	0.85 ± 0.18	-0.25	-0.42
$5_{5,0} - 6_{6,1}$	7.5956	3934	39	33.0	29.8	-9.2 ± 0.5	10.3 ± 1.6	0.99 ± 0.18	0.19	0.03
$6_{3,4} - 7_{4,3}$	7.7350	3701	45	39.0	12.3	-7.0 ± 0.4	10.7 ± 1.0	0.88 ± 0.10	0.03	-0.14
$6_{5,2} - 7_{6,1}$	7.7405	4181	45	39.0	24.2	-12.8 ± 0.3	13.0 ± 0.9	0.88 ± 0.08	0.01	-0.14